NASA-CR-182157

IN-26-CR
167344

ANISOTROPIC CONSTITUTIVE MODELING FOR NICKEL-BASE SINGLE CRYSTAL SUPERALLOYS

A dissertation submitted to the

Department of Aerospace Engineering and Engineering Mechanics
College of Engineering
Division of Graduate Education and Research
University of Cincinnati

in partial fulfillment of the
requirement for the degree of

Doctor of Philosophy

1988

by

Michael Y. Sheh

NAG3-511
NASA-CR-182157

B.S.M.E. National Cheng-Kung University, Taiwan, R.O.C., 1980
M.S.As.E. University of Cincinnati, 1986

(NASA-CR-182157) ANISOTROPIC CONSTITUTIVE MODELING FOR NICKEL-BASE SINGLE CRYSTAL SUPERALLOYS Ph.D. Thesis (Cincinnati Univ.) 190 p CSCL 11F
N88-29961
Unclas
G3/26 0167344

ANISOTROPIC CONSTITUTIVE MODELING FOR NICKEL-BASE SINGLE CRYSTAL SUPERALLOYS

A dissertation summitted to the

Department of Aerospace Engineering and Engineering Mechanics
College of Engineering
Division of Graduate Education and Research
University of Cincinnati

in partial fulfillment of the
requirement for the degree of

Doctor of Philosophy

1988

by

Michael Y. Sheh

B.S.M.E. National Cheng-Kung University, Taiwan, R.O.C., 1980
M.S.As.E. University of Cincinnati, 1986

ABSTRACT

The purpose of this research is to develop a anisotropic constitutive model based on crystallographic slip theory for nickel-base single crystal superalloys. The constitutive equations developed in this research utilizes drag stress and back stress state variables to model the local inelastic flow. Specially-designed experiments have been conducted to evaluate the existence of back stress in single crystal superalloy Rene N4 at 982°C. The results suggest that i) the back stress is orientation dependent; and ii) the back stress state variable is required for the current model to predict material anelastic recovery behavior.

Preliminary study on crystal lattice rotation during creep is made and a lattice rotation kinematics is established for future development. A procedure has been developed for the derivation of material constants from experimental data.

The model has been evaluated for its predictive capability on single crystal material behavior including orientation dependent stress-strain response, tension/compression asymmetry, strain rate sensitivity, anelastic recovery behavior, cyclic hardening and softening, stress relaxation, creep and associated crystal lattice rotation. Limitations and future development needs are discussed.

ACKONLEDGMENTS

I would like to express my sincere gratiyude to Professor Donald C. Stouffer for his suggestion of this research topic and for his guidance and assistance in the completion of this research.

I am also thankful to Professors David L. Butler, N. Jayaraman, and Richard W. Young and Dr. Richard McKnight for being members of my dissertation committeee and reviewing this work.

I am also appreciative to Mr. David A. Alden for his cooperation in conducting the high temperature experiments during this research.

I also want to acknowledge NASA for their finacial support in this research efforrt.

I want to thank Ms. Carol Walker for reviewing the grammatical content of this dissertation.

I also wish to thank my loving wife, Christina, for encouraging me to pursue this work and my son, Howie, for inspiring me to finish it.

I want to thank my parent for their endless love and support during my pursuit of this research.

Finally, I thank God for blessing me with the opportunity to do this research.

TABLE OF CONTENTS

PAGE

ABSTRACT i

ACKNOWLEDGEMENTS ii

TABLE OF CONTENTS iii

LIST OF TABLES viii

LIST OF FIGURES ix

CHAPTER I INTRODUCTION TO CONSTITUTIVE MODELING FOR NICKEL-BASE SINGLE CRYSTAL SUPERALLOYS 1

1.1 Nickel-Base Single Crystal Superalloys Overview .. 1

1.1.1 Structural Properties 1

1.1.2 Mechanical Properties 3

1.2 Consitutive Modelling History 10

1.2.1 Crystallographic Approach 10

1.2.2 Dame and Stouffer's Model 12

1.3 Scope of the Present Study 13

CHAPTER II BACK STRESS AND DRAG STRESS 17

2.1 State Variable Constitutive Modeling 17

2.2 Phenomenological Modeling Using Internal Stress .. 21

2.3 Experimental Evaluation of Internal Stress 24

2.4 Physical Background for State Variables 25

2.5 Back Stress in Single Crystals 28

CHAPTER III DEFORMATION MECHANISM OF NICKEL-BASE SINGLE CRYSTAL SUPERALLOYS 34

3.1 High Strain Rate Deformation Mechanism 36

3.2 Low Starin Rate Deformation Mechanism 38

3.3 Crystal Lattice Rotation During Creep 42

3.4 Summary Of Physical Background For Single Crystal Constitutive Model 45

LIST OF TABLES

PAGE

Table 1-1 Compositions And Heat Treatment Of Modern Single Crystal Superalloys. 2

Table 3-1 List Of Slip Plane And Slip Direction For Each Slip System And The Associated Slip Number. 35

Table 4-1 Corresponding Slip System Number For Resolved Shear Stresses, τ_1, τ_2, and τ_3 In Equation (3.19). 61

Table 5-1 Discriptions Of Mechanical Tests For Rene N4 At 982°C.. 80

Table 5-2 Experimental Data For Determining Elastic Material Constants Of Rene N4 At 982°C. 90

Table 5-3 Distribution Of Resolved Shear Stress In Each Slip System For A Loading Of 1000MPa In The [100], [110], [111], And [321] Directions. 93

Table 5-4 Material constants for Rene N4 VF317 at 760°C 116

Table 5-5 Material constants for Rene N4 at 982°C. 117

Table 7-1 Data Base Requirement for Determining Material Constants In The Current Model. 161

PRECEDING PAGE BLANK NOT FILMED

IV-V-VI

PAGES iv-v-vi INTENTIONALLY BLANK

LIST OF FIGURES

PAGE

Figure 1-1 Microstructure Of Nickel-base Single Crystal Superalloy. 4

Figure 1-2 Yield Strength Of PWA1480 At 593°C As A Function of Orientation Along The [001]-[011] Boundary Of The Standard Stereographic Triangle. 5

Figure 1-3 Yield Strength Of PWA1480 As A Function Of Temperature At Two Strain Rates For [100] oriented specimens. 5

Figure 1-4 Yield Strength Of PWA1480 As A Function Of Temperature for the [001], [011] and [111] orientations in tension and compression. 7

Figure 1-5 Effect Of Temperature On The Ultimate Tensile Strength Of SC 7-14-6. 7

Figure 1-6 Strain Rate Sensitivity Of PWA1480 At 871°C In The [111] Orientation. 8

Figure 1-7 Cyclic Hardening Of PWA1480 In The [321] Orientation At 760°C. 8

Figure 1-8 Cyclic Response Of PWA1480 At 760°C. 14

Figure 2-1 The interdisciplinary approach to constitutive Modeling. 18

Figure 2-2 Phenomenological model utilizing back stress concept to explain discrepency in creep-stress dependence between theory and experiment: (a) the model without back stress; (b) the model with back stress. 23

Figure 2-3 Double Tensile Test In The [100] Orientation With A 120 Second Hold Period. 30

Figure 2-4 Double Tensile Test In The [111] Orientation With A 120 Second Hold Period. 31

Figure 2-5 Inelastic Strain-Time Histories For The [100] And [111] Orientations During The 120 Seconds Hold Period In The Double Tensile Test. 32

Figure 3-1 Orientations Of Crystals That Exhibited Octahedral Slip (symbol ■) or cube slip (symbol □) or mixed Octahedral And Cube Slip (symbol ◪). 39

Figure 3-2 Schmid Factor Contour For <112>{111} Slip Systems. 41

Figure 3-3 Directions Of Crystal Lattice Rotation In Standard Stereographic Triangle For Single Crystals Under <112>{111} slip. 44

~~PRECEDING PAGE BLANK NOT FILMED~~

PAGE

Figure 3-4 MAR-M247 Creep Data Shown As A Function Of Orientation For Single Crystals Tested At 774°C And 724MPa: (a) Primary Creep Strain; (b) Secondary Creep Rate; and (c) the Schmid factor along the [100]-[110] boundary. . 46

Figure 4-1 Displacement Field Assumed In Dame And Stouffer's Model. 52

Figure 4-2 The proposed kinematics in the current model: (a) A Pure Rotation In The κ Plane (Plane Normal $\underset{\sim}{n}^{\kappa}$) Plus (b) A Pure Shear On The α Slip Plane (Plane Normal $\underset{\sim}{n}^{\alpha}$) In The β Direction. 54

Figure 4-3 Lall, Chin, And Pope's Model (1979) For Tension/Compression Asymmetry. 61

Figure 4-4 Creep Curves Of Selected MAR-M247 Specimens Tested At 774°C and 724MPa. 67

Figure 4-5 Stack-Of-Coins Model. 70

Figure 4-6 Interpretation Of The Stack-Of-Coins Model Using Stereographic Triangle Plotted In The 3-D Space. 71

Figure 5-1 Tensile Tests Of Rene N4 VF317 At 760°C. 76

Figure 5-2 Creep Tests Of Rene N4 VF317 At 760°C. 77

Figure 5-3 Experimental Data For Tensile Tests In The [100], [110], [111] And [321] orientations Of Rene N4 At 982°C. 81

Figure 5-4 Experimental Data For Fatigue Test Of Rene N4 In The [100] Orientation At 982°C. 82

Figure 5-5 Experimental Data For Fatigue Test Of Rene N4 In The [111] Orientation At 982°C. 83

Figure 5-6 Experimental Data For Fatigue Test Of Rene N4 In The [321] Orientation At 982°C. 84

Figure 5-7 Experimental Data For Fatigue Test With A 30-Second Peak Tensile Strain Hold Of Rene N4 In The [321] Orientation At 982°C. 85

Figure 5-8 Experimental Data For Fatigue Test With A 30-Second Peak Compressive Strain Hold Of Rene N4 In The [210] Orientation At 982°C. 85

Figure 5-9 Axis Systems For Equation (4.2). 89

Figure 5-10 Shear Stress And Back Stress Histories For Tensile Test Of Rene N4 In The [100] Orientation At 982°C. 98

PAGE

Figure 5-11 Back Stress Rate History For Tensile Test Of Rene N4 In The [100] Orientation At 982°C. 99

Figure 5-12 Evaluation Of G_1 Based On Linear Relationship Between Back Stress and Resolved Shear Stress. 101

Figure 5-13 Evaluation Of F_1 And n_{13} Using Relaxation Data In Double Tensile Test Of Rene N4 At 982°C. 103

Figure 5-14 Predicted Double Tensile Test In The [111] Orientation Using F_1 and n_{13} Values Determined From The Tensile Curve (Figure 5-14a) And From The Anelastic Recovery Data (Figure 5.14b). 105

Figure 5-15 Linear Relationship Between Saturated Back Stress, Ω_{SAT}, And Resolved Shear Stress, τ, For Creep Of Rene N4 VF317 At 760°C and 756MPa, 655MPa And 620MPa. 112

Figure 5-16 Relationship Between Elastic Back Stress, Ω_2, And Resolved Shear Stress, τ, During The Elastic Loading To Creep Stress For Rene N4 VF317 At 760°C. 113

Figure 5-17 Flow Chart For Material Parameter Evaluation Procedure. 115

Figure 6-1 Comparison Between Model Predictions And The Experimental Results In The Nominal [100], [110] and [310] Orientations For Rene N4 VF317 At 760°C. 120

Figure 6-2 Predicted Tensile Response Of Rene N4 VF317 In The [100] Orientation At Five Different Strain Rates at 760°C. 122

Figure 6-3 Comparison Between Calculated Local Slip Rate, $\dot{\gamma}$, Of Octahedral a/2<110> (SLIP 1) and a/2<112> (SLIP 14) Slip Systems For Tensile Response Of Rene N4 VF317 In The [100] Orientation At 760°C And Strain Rate Of 10^{-7}/sec. 123

Figure 6-4 Comparison Between Calculated Local Slip Rate, $\dot{\gamma}$, Of Octahedral a/2<110> (SLIP 1) and a/2<112> (SLIP 14) Slip Systems For Tensile Response Of Rene N4 VF317 In The [100] Orientation At 760°C And Strain Rate Of 10^{-4}/sec. 124

Figure 6-5 Predicted Cyclic Response Of Rene N4 VF317 In The [100] Orientation At 760°C. 126

Figure 6-6 Predicted Cyclic Response Of Rene N4 VF317 In The [110] Orientation At 760°C. 127

PAGE

Figure 6-7 Comparison Between Experimental Data and Predicted Creep Responses Of Rene N4 VF317 At 760°C and 756MPa, 655MPa And 620MPa In The [100] Orientation. 129

Figure 6-8 The Orientations In Which Creep Calculations Were Made. 130

Figure 6-9 Predicted Creep Responses Of Rene N4 VF317 At 760°C And 655MPa Along The [100]-[110] Boundary. 131

Figure 6-10 Predicted Creep Responses Of Rene N4 VF317 at 760°C And 655MPa In Orientations 10° Away From [100] And 9° Apart From Each Other (Label R-W In Figure 6-8). 133

Figure 6-11 Amount Of Lattice Rotation As A Function Of Time For Creep Calculations In Figure 6-10. 134

Figure 6-12 Correlation Between Model Calculations And Experimental Data For Tensile Tests Of Rene N4 In The [100] and [111] Orientations At 982°C. 136

Figure 6-13 Comparison Between Calculated Local Slip Rate $\dot{\gamma}$ For A Cube Slip System (Slip 25) And A Octahedral Slip System (Slip 11) In Tensile Response Of Rene N4 In The [111] Orientation At 982°C. 138

Figure 6-14 Comparison Between Experimental Data And Predicted Tensile Responses Of Rene N4 In The [110] And [321] Orientations At 980°C And Strain Rates Of 1.0×10^{-4}/sec And 5.0×10^{-4}/sec, Respectively. 139

Figure 6-15 Predicted Tensile Responses of Rene N4 In The [100] Orientation At 980°C And Strain Rates Of 1×10^{-4}/sec, 6×10^{-4}/sec and 1×10^{-3}/sec. 140

Figure 6-16 Comparison Between Experimental Data And Predicted Double Tensile Response Of Rene N4 In The [100] Orientation At 982°C. 142

Figure 6-17 Comparison Between Experimental Data And Predicted Double Tensile Response Of Rene N4 In The [111] Orientation At 982°C. 143

Figure 6-18 Comparison Between Predicted Anelastic Recovery And The Experimental Data In Double Tensile Test Of Rene N4 In The [100] and [111] Orientations At 982°C. 144

Figure 6-19 Comparison Between Experimental Data And Predicted Cyclic Response In The [100] Orientation For Rene N4 at 982°C. 146

PAGE

Figure 6-20 Comparison Between Experimental Data And Predicted Cyclic Response In The [111] Orientation For Rene N4 at 982°C. 147

Figure 6-21 Comparison Between Experimental Data And Predicted Cyclic Response In The [321] Orientation For Rene N4 at 982°C. 148

Figure 6-22 Predicted Cyclic Response In The [110] Orientation For Rene N4 At 982°C. 149

Figure 6-23 Comparison Between Experimental Data And Predicted Cyclic Response With Peak Compressive Strain Hold In The [321] Orientation For Rene N4 At 982°C. 151

Figure 6-24 Comparison Between Experimental Data And Predicted Cyclic Response With Peak Tensile Strain Hold In The [210] Orientation For Rene N4 At 982°C. 152

Figure 6-25 Predicted Cyclic Response In The [100] Orientation With Hypothetical Cyclic Hardening Parameters For Rene N4 At 982°C. 153

Figure A-1 Octahedral a/2<110> and a/2(112> slip systems. 165

Figure A-2 Cube a/2<110> slip systems. 172

CHAPTER I

INTRODUCTION

1.1 Single Crystal Superalloys Overview

Nickel base single crystal superalloys attracted considerable interest for use in rocket and gas turbine engines because their high temperature properties are superior to those of polycrystalline nickel-base superalloys. In high temperature applications, grain boundaries in polycrystalline alloys provide passages for fast diffusion and oxidation. Thus, intercrystalline cracks are frequently initiated at the grain boundaries and causes rupture failure.

The development of superalloy single crystals, by eliminating the grain boundaries, produces far superior thermal fatigue and creep properties to conventional superalloys. Also, the absence of grain boundary strengthening elements in single crystals provides considerable alloying and heat treatment flexibility (Gell et al, 1980), which also improves the strength and life of the material (VerSnyder and Piearcey, 1966; Kear and Piearcey, 1967). However, the lack of grain boundaries in single crystal alloys allows the exposure of material anisotropy. Which gives rise to complicated thermal-mechanical responses and increases the difficulty in mathematically characterizing the behavior of single crystal alloys for design of engine components.

1.1.1 Structural Properties

Developed in the late 1960's, nickel-base superalloy single crystals are based on the Ni-Cr-Al alloy system. Chemical compositions vary among alloys developed by different companies. Table 1-1 lists the compositions for some modern single crystal superalloys. All of these

Table 1-1 Compositions And Heat Treatment Of Modern Single Crystal Superalloys.

	Element, WT. %										
	Al	Ti	Ta	Nb	Cr	Mo	W	Co	C	B	Zr
[a]RENE N4	3.7	4.2	4.0	0.5	9.25	1.5	6.0	7.5	-	-	-
[b]PWA-1480	5.0	1.5	12	-	10	-	4.0	5.0	-	-	-
[c]SRR99	12	2.7	0.9	-	9.6	-	3.1	5.0	0.07	-	-

a. General Electric Co., Heat Treatment: 1260°C/2h/gas quench + 1080°C/4h/air cool + 900°C/16h/air cool.(Miner et al, 1986a)

b. Pratt & Whitney Co., Heat Treatment: 1288°C/4h/air cool + 1079°C/4h + 871°C/32h.(Milligam and Antolovich, 1987)

c. Messrs. Rolls-Royce Ltd., Heat Treatment: 1300°C/4h/water quench + 1100°C/1h + 871°C/16h. (Hopgood and Martin, 1986) modern single crystal materials are two-phase alloys with a large volume fraction of γ' precipitates, an ordered, face-centered cubic (f.c.c.) Ni_3Al inter-metallic compound, interspersed in a coherent f.c.c. γ solid solution as shown in Figure 1-1. The strength of the alloy is a function of the γ' size and the volumn fraction of γ'. Experiments have determined that the peak creep strength is achieved with a volume fraction of γ' of about 60% (Shah and Duhl, 1984; Pope and Ezz, 1984). Although the composition may be quite different among modern superalloy single crystals, the microstructure of these alloys are similar. For example, PWA1480 has much more Ta, less W, no Mo or Nb, and much higher ratio of Al to Ti than Rene N4. However, both alloys have similar γ' volume fraction of about 60-65% and the size of γ' about 0.25μm.

1.1.2 Mechanical Properties

Single crystal alloys exhibit cubic symmetry structure in the elastic range. The elastic stress-strain relationship can be uniquely described by using three independent material constants: Young's modulus E, shear modulus G and Poisson ratio ν. (Jones, 1977; Yang, 1984)

The inelastic response of single crystal materials is quite different from the behavior of polycrystalline nickel-base superalloys. The yield strength of single crystal alloys is a function of the material orientation, relative to the direction of the applied stress (Shah and Duhl, 1984; Dalal et al., 1984) and the strain rates (Milligan and Antolovich, 1987), as shown in Figures 1-2 and 1-3, respectively. Nickel-base single crystal alloys also exhibit significant tension/ compression asymmetry in yield strength (Figure 1-2, Lall et al., 1979; Ezz et al., 1982; Umakoshi et al., 1984; Heredia and Pope, 1986; Miner et al., 1986a). This behavior is primarily due to slip on the

ORIGINAL PAGE IS
OF POOR QUALITY

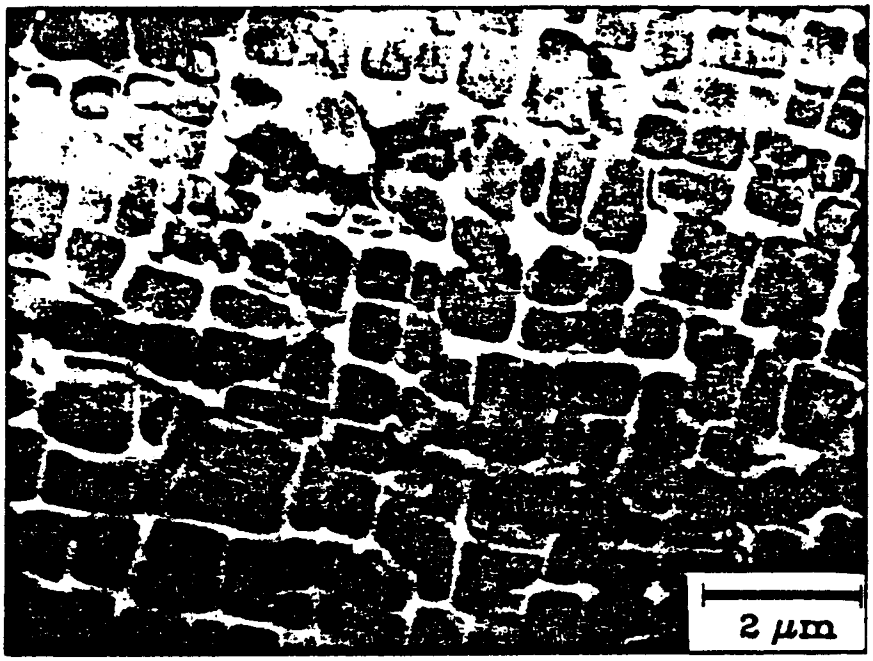

Figure 1-1 Microstructure Of Nickel-base Single Crystal Superalloy.

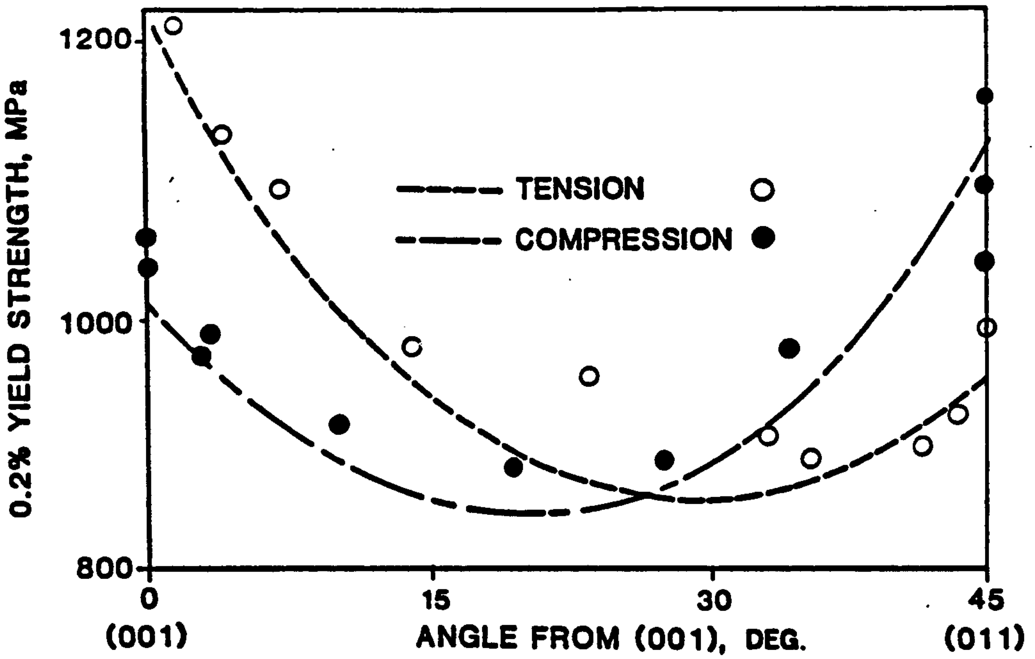

Figure 1-2 Yield Strength Of PWA1480 At 593°C As A Function of Orientation Along The [001]-[011] Boundary Of The Standard Stereographic Triangle.

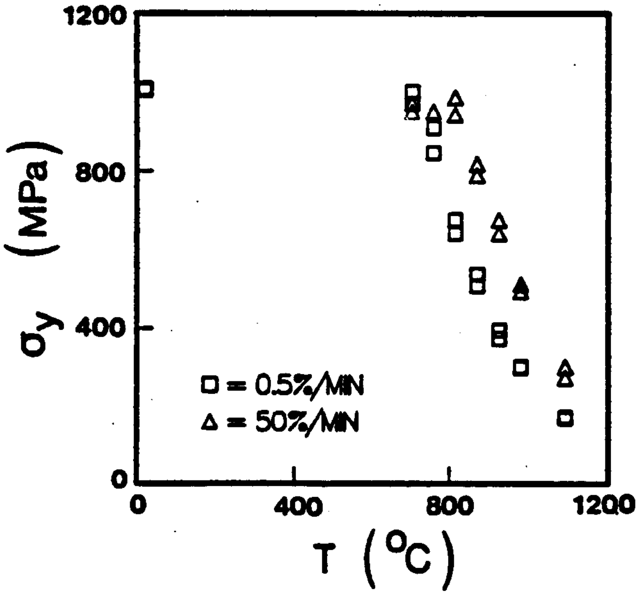

Figure 1-3 Yield Strength Of PWA1480 As A Function Of Temperature At Two Strain Rates For [100] oriented specimens.

octahedral slip system; i.e., dislocation in the {111} planes. The tension/compression asymmetry is negligible near the [111] orientation where cube slip (i.e., dislocation in the {100} planes) was found to be the primary slip system. Above the critical temperature, approximately 700-760°C, there is a sharp drop in the yield strength (see Figure 1-4), cube slip becomes more predominant, and the tension/compression asymmetry is less significant (Shah and Duhl, 1984; Heredia and Pope, 1986; Gabb et al., 1986).

In a pilot study of cast single crystal alloy SC 7-14-6 (Ni-6.8Al-13.8Mo-6W), Dalal et al. (1984) showed that the tensile strength is substantially less anisotropic at temperatures above 760°C (see Figure 1-5). The [011] orientation generally displays the lowest strength and greatest ductility and invariably produces an elliptically deformed (initially circular cross section) test sample. Whereas, the [111] orientation has the highest ultimate strength at 70°C and 760°C. These results are generally consistent with Rene N4 data published by Miner et al. (1986a).

Similar to isotropic nickel-base superalloys, single crystal alloys exhibit strain rate sensitivity and cyclic hardening (Milligan and Antolovich, 1987; Swanson, 1984a,b; Stouffer et al., 1987) as shown in Figures 1-6 and 1-7, respectively. In low cycle fatigue tests with fixed total strain range, fatigue life changes in decending order with [100], [111], and [110] crystal orientation. However, normalizing the strain range to a stress range by using the elastic modulus yields a linear relationship. This result indicates that the difference in low cycle fatigue life for different crystal orientation can be explained by elastic moduli and resultant stress range (Dalal et al., 1984; Dreshfield, 1986). While using fixed inelastic strain range. fatigue

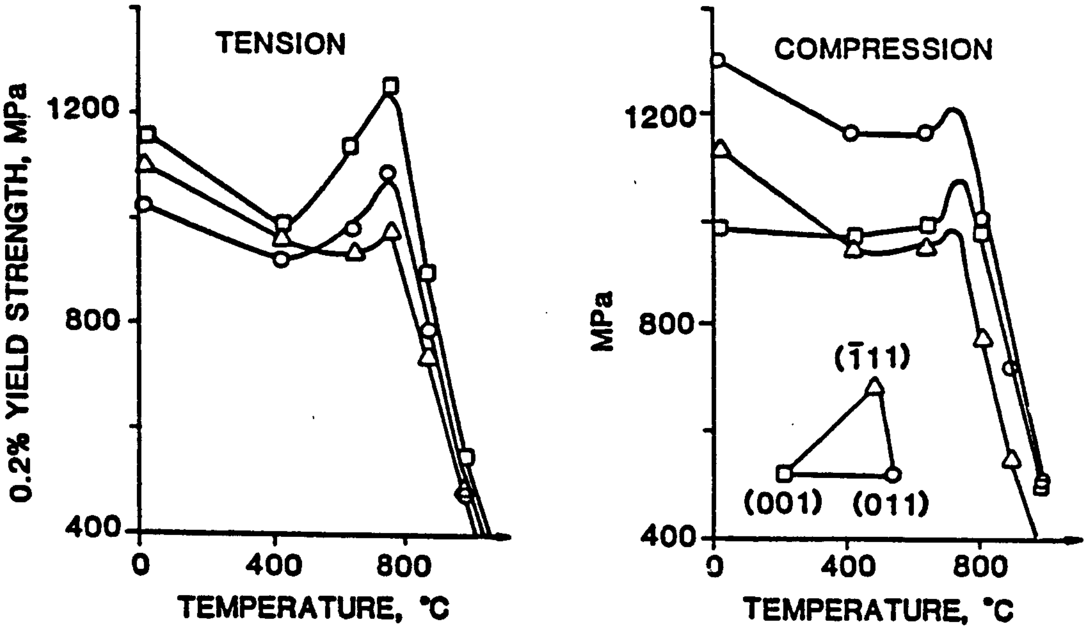

Figure 1-4 Yield Strength Of PWA1480 As A Function Of Temperature for the [001], [011] and [111] orientations in tension and compression.

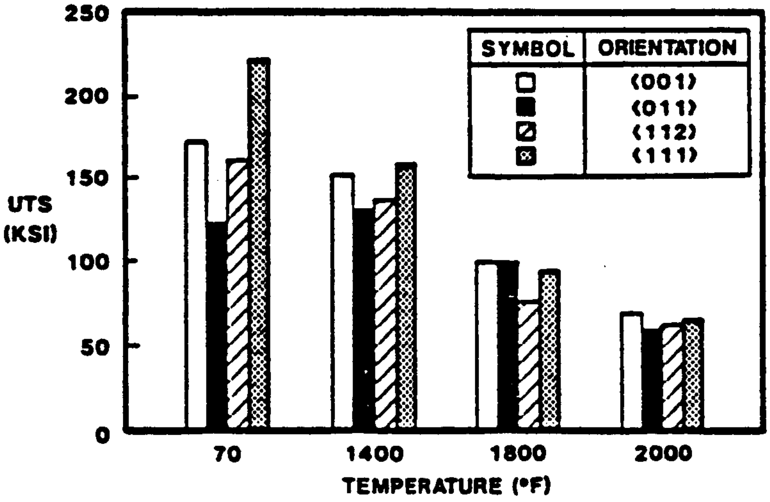

Figure 1-5 Effect Of Temperature On The Ultimate Tensile Strength Of SC 7-14-6

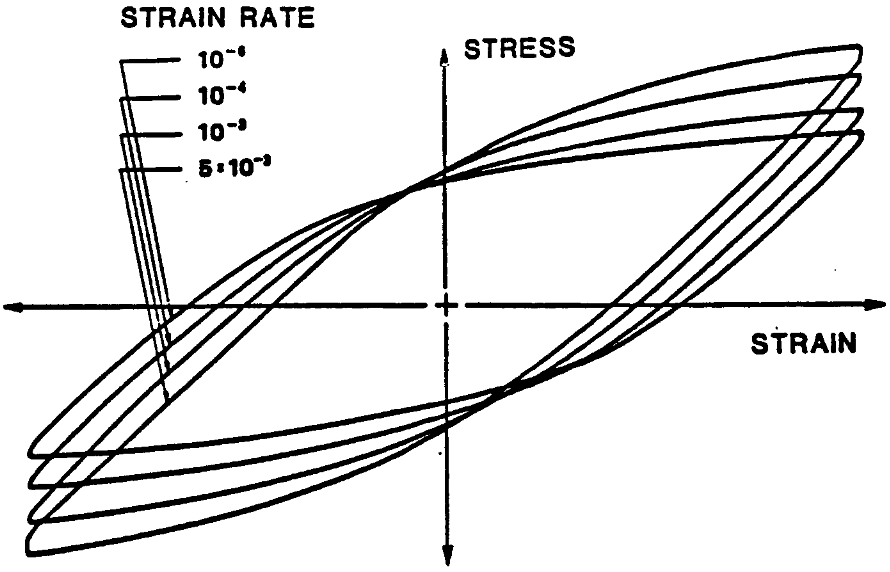

Figure 1-6 Strain Rate Sensitivity Of PWA1480 At 871°C In The [111] Orientation

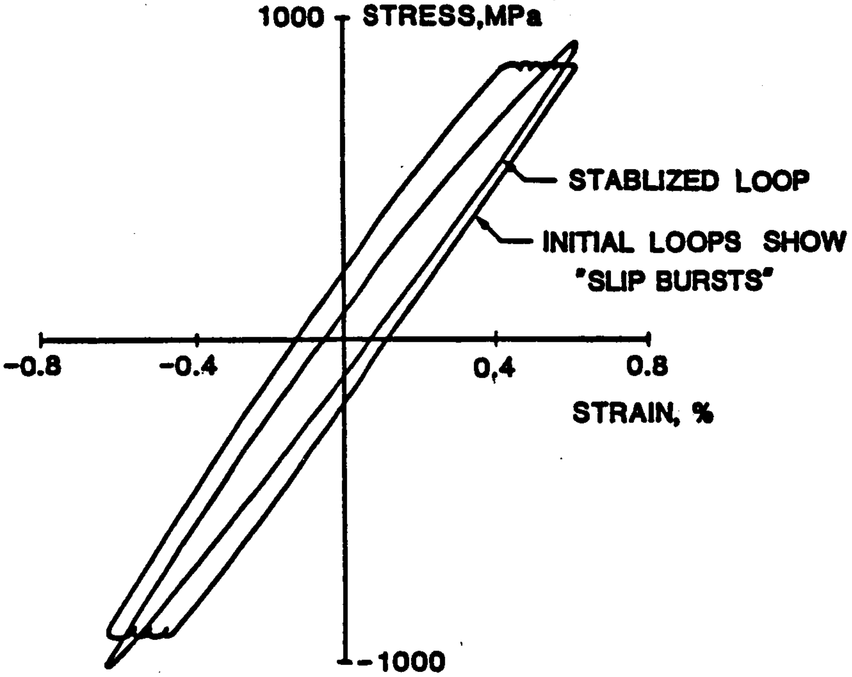

Figure 1-7 Cyclic Hardening Of PWA1480 In The [321] Orientation At 760°C

life was not significantly dependent upon crystal orientation at 760°C and modest orientation dependence at 980°C for Rene N4. (Gabb et al., 1986)

Nathal and Ebert (1985) studied the creep-rupture behavior of single crystal NASAIR 100 at temperatures of 925°C and 1000°C. Their results showed the steady state creep rate, time to failure, time to the onset of secondary creep exhibited power law dependencies on the applied stress for loading in the [100] direction.

For loading in directions other than [100], creep behavior is significantly anisotropic. In general, creep loading near the [011] orientation have much shorter rupture lives than near the [100] orientation (Kear and Piearcey, 1967; MacKey and Maier, 1982). Very long rupture lives were observed for samples loaded near the [111] direction (MacKay and Maier, 1982). This finding was initially explained by using Schmid's law and multiplicity of slip for the {111}<112> slip systems (Leverant and Kear, 1970). MacKay and Maier (1982) later found that the stress rupture lives at intermediate temperatures were greatly affected by the amount of lattice rotation required to produce intersecting slip. For example, crystals that required large rotations to become oriented for intersecting slip exhibited large primary creep strain and shorter rupture lives. In the MacKay/Maier study, the stress rupture lives were also found influenced by the relative orientations of the [001]-[011] boundary to the loading axis.

Both of the above studies (i.e. Leverant and Kear, 1970, MacKay and Maier, 1982) are fully reviewed in Section 3.1.3, Chapter III. For convenience, they are summarized here. Both showed the same trend; namely, longer rupture life is generally associated with less crystal rotation, smaller Schmid's factor, smaller primary creep strain and strain rate, and smaller secondary creep rate. Thess results correlate with the deformation and rotation mechanisms found in creep samples.

The complicated mechanical behavior of single crystal alloys clearly demonstrates the complexity involved in establishing a constitutive model for this material. Understanding the deformation physics is essential to formulating such a model.

1.2 Constitutive Modeling History

Constitutive modeling of anisotropic material, which includes single crystal alloys in this study, can be divided into two categories: continuum mechanics approach and crystallographic approach. Most continuum mechanics approachs are based on a mathematical form similar to yield surface plasticity theory for isotropic materials (Lee and Zaverl, 1978, 1979; Shih and Lee, 1978; Eisenberg and Yen, 1981; Gilat, 1985). Material anisotropy is introduced by including an anisotropy matrix in the yield function. Kinematic hardening is modeled by utilizing a back stress tensor or a displacement of the yield surface. Isotropic hardening is accounted for with a change in yield surface size.

The most significant shortcoming of the continuum mechanics approach is that the actual deformation mechanisms are not correlated to the theory. This lack of correlation limits the predictive capability of the model outside the range for which it was calibrated.

1.2.1 Crystallographic Approach

The crystallographic approach is based on identifying the active slip planes and slip directions. Shear stresses are computed on each of the slip planes from the applied stress. The slip deformation is computed on each slip system. The macroscopic inelastic strain rates or strain increments are then the sum of the contributions from each individual slip system.

Early developments in the crystallographic approach are attributed to Taylor (1938), Bishop and Hill (1951a,b) and Bishop (1952). This approach was successful in the modeling of texture evolution for both f.c.c. and b.c.c. (body-centered cubic) materials (Asaro and Needleman, 1985; Bacroix et al., 1986; Molinari et al., 1987). This approach has also been used widely in polycrystal plasticity (Hill, 1965, 1966; Hutchinson, 1970; Hill and Havner, 1982; Asaro, 1983, 1985) and localized plastic deformation (Asaro and Rice, 1977; Peirce et al., 1982, 1983; Asaro and Needleman, 1984).

The advantages for the crystallographic approach are as follows:

- The kinematic framework is concise and easy to correlate with experimental observations.
- A significant portion of this approach is based on the physics of deformation mechanisms. Presumably, this will enhance the predictive capability of the model.
- Theories developed based on this approach can be easily verified and modified as additional information is obtained about deformation mechanisms at various loading conditions. This applies particularly since advanced electro-optical instruments were available (such as transmission electron microscope and scanning electron microscope).

1.2.2 Dame and Stouffer's Model (1985)

The application of the crystallographic approach to single crystal nickel-base superalloys began with the work of Paslay et al. (1970, 1971), and continued with the work of Shah (1983) to the γ' phase of these alloys. Recently, an anisotropic constitutive model using crystallographic approach was developed by Dame and Stouffer for nickel-base single crystal superalloys at isothermal condition (1985, 1986). This model is discussed in detail below.

The Dame and Stouffer model is also based on the concept of unified theory that the total strain is decomposed into elastic and inelastic components. The elastic strains were calculated by using cubic symmetry. The inelastic strain rate was calculated by summing the contributions of slip in each slip system. The inelastic slip rate on each slip system was computed from a local inelastic constitutive equation that depended on local resolved shear stress components in each slip direction and local state variables.

Because of the different mechanical responses exhibited by octahedral slip samples and cube slip samples (Miner, 1986a,b), two separate flow equations were used in Dame and Stouffer's model to compute the inelastic strain rate of the two slip systems. A non-Schmid's law formulation was used to model the tension/compression asymmetry and orientation dependence in the octahedral slip system. This was achieved by incorporating the core-width effect proposed by Lall, Chin and Pope (1979). With the core-width effect, stress-aided Shockly partials and thermally-aided cross-slip mechanisms were used to explain the tension/compression asymmetry in yield stress.

A second flow equation, based on Schmid's law concept, was used to model the inelastic response in the cube systems because tension/

compression asymmetry was insignificant. In both octahedral and cube slip systems, a Bodner-Partom (1975) type of flow equation was used to model the response at higher strain rate (i.e., tensile response). At lower strain rates (i.e., creep response), where diffusion is the controlling mechanism, a diffusion model similar to the Bodner-Partom equation was used.

Dame and Stouffer's model was also based on a system of state variables similar to the drag stress. Their model was considered successful for predicting both the orientation dependence and tension/compression asymmetry for tensile and creep histories for single crystal alloy Rene' N4 at 760°C. However, certain properties including fatigue and anelastic recovery were not satisfactorily modeled.

1.3 Scope of the Present Study

Recent experimental observations (Swanson, 1984; Stouffer et al., 1987) have shown that single crystal alloys could have an anelastic effect; i.e., negative inelastic strain rate at a positive stress level, or vice versa. This effect is demonstrated by loading the sample into the plastic region and unloading the sample to a certain stress or strain level and holding that stress or strain for a period of time.

For example, Figure 1-8 shows the cyclic response of PWA1480 at 760°C (Swanson, 1984b). The test was interrupted with stress or strain hold periods at several locations on the hysteresis loop. After each hold period, cycling continued until the hysteresis loop again stabilized.

The relaxation that occurs when the stress level is above zero is thought to be similar to the internal stress, or back stress relaxation in most polycrystalline alloys. This result also suggests that using a

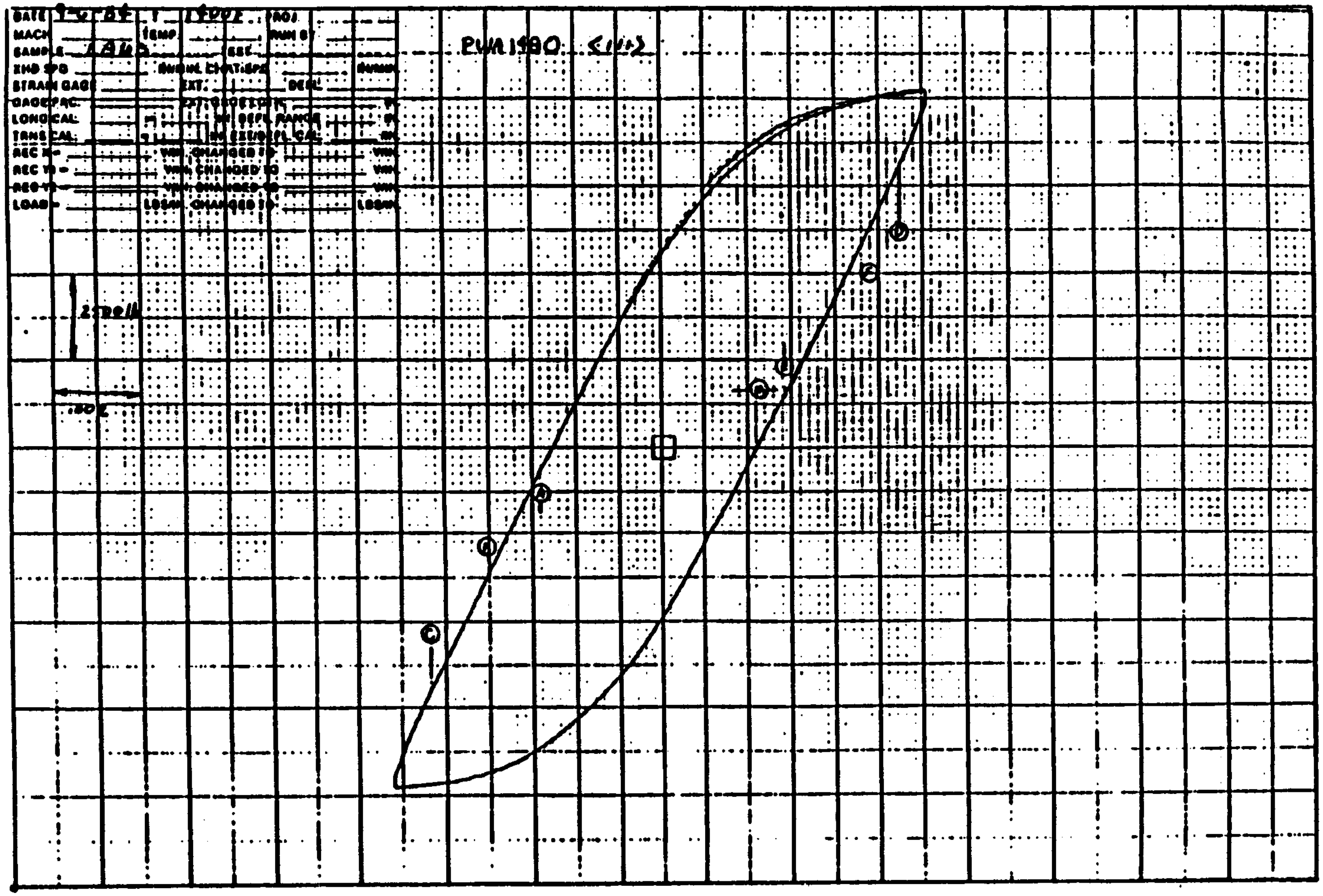

Figure 1-8 Cyclic Response Of PWA1480 At 760°C

ORIGINAL PAGE IS
OF POOR QUALITY

single drag stress state variable (such as Dame and Stouffer's model) is insufficient to simultaneously model the cyclic hardening/softening and the relaxation behavior. A more detailed discussion on this topic will appear in Sections 2.4 and 2.5, Chapter II.

Creep modeling, as proposed by Dame and Stouffer, is also inappropriate from the deformation kinematics point of view. According to a number of creep studies on nickel-base single crystal superalloys (e.g., Leverant and Kear on MAR-M200 (1970, 1971); MacKay and Maier on MAR-M247 (1982); Hopgood and Martin on SRR99(1986)) the active slip mechanisms were primarily <121>{111} rather than <101>{111} slip systems which were used in Dame and Stouffer's model. Use of <112>{111} slip systems yields entirely different distribution of Schmid factor and resolved shear stress from the <110>{111} slip systems for each slip system.

The creep studies also showed that significant crystal lattice rotation can occur during the test of samples with single slip. The direction of lattice rotation was controlled by the active slip systems. As a result, creep modeling must be modified to use the correct slip systems. Also, the kinematics must be extended for lattice rotation.

Considering the problems disscussed above, the objectives of this study are as follows:

⊙ To continue the development of the crystallographic model by incrporating a back stress state variable. It has been shown in polycrystalline materials that back stress/drag stress representation has several advantages over a drag stress model, including the ability to accurately predict strain hardening and cyclic hardening or softening. (Walker, 1981; Ramaswamy, 1985; James, et al., 1987). The work involved in this phase includes:

  - Reformulating the inelastic flow equation
  - Formulating appropriate back stress and drag stress evolution equations
  - Generating computer codes to evaluate experimental data, estimate material constants, and perform constitutive modeling.

- ⊙ To investigate single crystal creep behavior and lattice rotation characteristics and improve the physical basis of the model. The work involves
  - Survaying the literature on the creep properties; i.e., the slip mechanisms, the relationship between primary creep and secondary creep, and lattice rotation characteristics
  - Re-examining the kinematics required for rotational properties; i.e., a small strain, finite deformation formulation, and implementing such a formulation into the model
  - Investigating the interaction between slip systems for high strain rate and low strain rate calculations
- ⊙ To support the experimental program at 760 - 980°C in various crystal orientations. This type of support was performed in cooperation with Dr. N. Jayaraman and Mr. D. Alden in the Material Science and Engineering Department at the University of Cincinnati.

CHAPTER II

BACK STRESS AND DRAG STRESS

The primary reason for incorporating a back state variable in the current model is that back stress/drag stress representation has several advantages over a drag stress model. One such advantage is the ability to accurately predict cyclic fatigue response. Before formulating such a model, an understanding of the state variable modeling approach is required.

2.1 State Variable Constitutive Modeling

State variable modeling began to flourish in the early 1970's and has gained wide recognition in recent years. The state variable modeling recognized the limitations of classical plasticity theory, i.e., the rate-independent idealization of metal behavior, separation of creep and plasticity, and complex yield surface behavior in multiaxial loading.

An important feature of state variable modeling is its ability to bring together different disciplines; namely, materials science, experimental mechanics, and analytical mechanics. The interactions among these three disciplines is demonstrated in Figure 2-1. Material science introduces a physical basis into the formulation of the constitutive models. Experimental mechanics conducts appropriate mechanical tests to explore the properties of the materials, and to calibrate and verify the analytical models. Analytical mechanics is used to explain some materials behavior, to motivate some experimental test protocols, and to translate the relationship between materials and mechanics into appropriate tensorial form for use in today's powerful

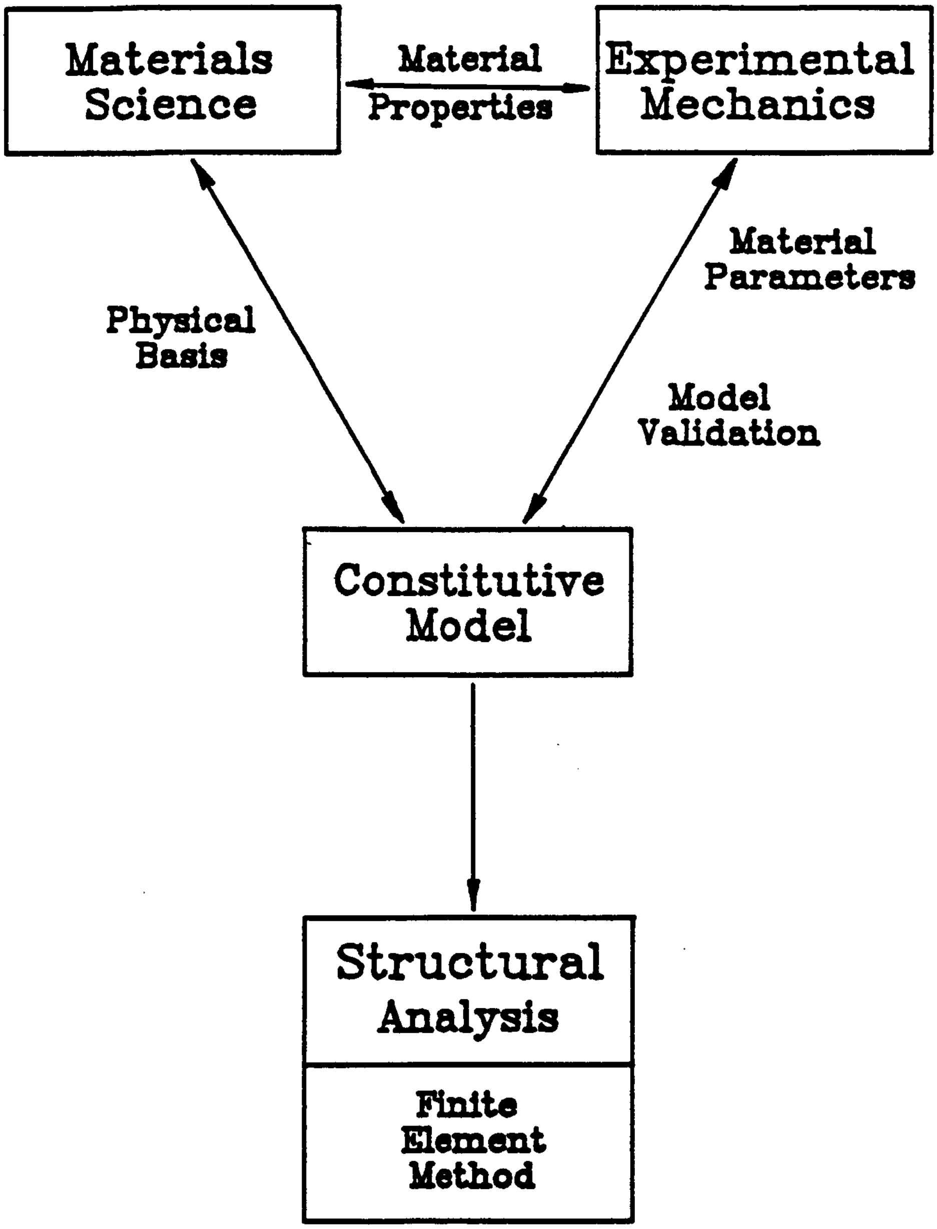
Materials Science
Material Properties
Experimental Mechanics
Physical Basis
Material Parameters
Model Validation
Constitutive Model
Structural Analysis
Finite Element Method

Figure 2-1 The interdisciplinary approach to constitutive Modeling

structural analysis schemes such as finite element methods. This interdisciplinary approach will permit establishment of deformation models that satisfy the laws of micromechanics (materials science) and continuum theory.

State variable modeling is also based on the concept that the microstructure of the material is a function of deformation histories. It assumes that the instantaneous state of the material can be defined by prescribing the current values of independent state variables. These variables are then placed into the constitutive relations that determine deformation or motion of an element, subject to a given loading condition.

Two kinds of state variables, that is, external and internal variables were classified by Swearengen and Holbrook (1985). The external variables are microstructure-insensitive and externally observable or measurable; external variables include the applied stress, pressure, strain rate and temperature. Internal state variables, represent the evolution of the microstructure during the deformation process; these variables comprise the information that affects the thermodynamic state and the response to applied loads. Internal state variables are likely to represent the evolution microstructure, including the density of dislocations and their patterns of arrangement, subgrain size and misorientation, grain boundary energy, and so forth.

A constitutive model that incorporates all external and internal variables to model the deformation is too complicated and practically impossible with our current technology. Also, it is difficult to precisely characterize internal variables in experimental programs and to interpret them in the constitutive equation.

Thus, instead of these explicitly defined internal variables, 'implicit' internal variables or synthetic variables have been formulated in the past to characterize the key accumulative effects in the evolution of the microstructure. Such a model is composed of a set of equations that are solved simultaneously. These equations include a kinetic law for the inelastic strain rate tensor:

$$\dot{\underset{\sim}{\epsilon}}^{I} = \dot{\underset{\sim}{\epsilon}}^{I}(\underset{\sim}{\sigma}, T, \alpha_i) \tag{2.1}$$

where $\underset{\sim}{\sigma}$ is the stress tensor, T is the absolute temperature and α_i is the synthetic variable or state variable, and equations that describe the evolution of the individual α_i; that is:

$$\dot{\alpha}_i = \dot{\alpha}_i(\dot{\underset{\sim}{\epsilon}}^{I}, \sigma, T, \alpha_i) \tag{2.2}$$

State variable approach can mathematically simulate details of extremely complicated phenomena without requiring detailed knowledge of individual components in the evolution of microstructure. This approach should be viewed as a mathematical simulation of the response of a continuum. With an appropriate mathematical functional form for each state variable, this type of model is extremely efficient when it is implemented into strructural analysis computer codes such as the finite element method. (Ramaswamy, 1985; James et al., 1987)

It has been suggested that at least one state variable is necessary in order to avoid hereditary integrals of strain rate history (Swearengen et al., 1976). However, consititutive models with a single state variable were found insufficient to provide predictive capability for situations other than steady monotonic deformation (Turner, 1979; Turner and Hasegawa, 1979; Swearengen and Holbrook, 1985). Swearengen and Holbrook (1985) also concluded that at least two state variables would be required if applied loads vary in time or stress space, but one may be sufficient for monotonic deformation.

To date, state variables including work hardening rate, recovery rate, hardness, creep deceleration parameter, and internal stress have been proposed. Some internal stress variables (such as frictional stress, over stress, kinematic stress, drag stress, back stress) were frequently used by metallugists and mechanists. The primary use of internal stress variable was to account for hardening, yielding, and inelastic strain rates in metals and alloys. These are usually achieved by replacing the applied stress σ in Equation (2.1) with the effective stress σ_{eff} according to:

$$\sigma_{eff} = \sigma - \sigma_i \qquad (2.3)$$

Despite the numerical interpretation of internal stress, σ_i, in Equation (2.3), the presence of internal stress has been observed experimentally. Internal stress has also been used to explain the discrepency between theory and experimental results. Hence, Equation (2.3) was frequently found in phenomenological models.

2.2 Phenomenological Modeling Using Internal Stress

The concept of internal stress in a number of material models results from the idea that the plastic deformation of crystalline solids occurs under a portion of the applied stress not under the entire stress (Cadek, 1987). This concept is used to discuss the discrepency between third power dependence of steady state creep rate and the experimentally observed higher power in metals and solid solution alloys which exhibits metal class behavior (Oikawa and Langdon, 1985). The temperature and stress dependence of steady state creep rates is generally described by the phenomenologically derived equation, which is frequently called the Dorn equation:

$$\frac{\dot{\epsilon}_s b^2 kT}{DG\nabla} = A(\frac{\sigma}{G})^n \tag{2.4}$$

where D is an appropriate diffusion coefficient, A is a dimensionless constant, G is the shear modulus, ∇ is the atomic volume, b is the length of Burgers vector, k is the Boltzmann constant, and is T the absolute temperature. When the homologous temperature T/T_m (T_m is the melting temperature) is above 0.5, the creep rate is controlled by lattice diffusion and the value of the stress exponent n is typically 5. At a lower homologous temperature, the creep rate is assumed to be controlled by dislocation core diffusion and the exponent n is typically 7. Weertman (1975) shown that all the theoretical models of creep should follow the third power law (n=3) for lattice diffusion and fifth power law (n=5) for dislocation core diffusion. The explanation for the discrepency between the natural and the experimental stress dependence is now widely accepted as the absence of internal stress in Equation (2.4).

According to the concept of internal stress, Cadek (1987) showed that the steady state creep rate can be described by:

$$\frac{\dot{\epsilon}_s b^2 kT}{DG\nabla} = A(\frac{\sigma}{G} - \frac{\sigma_i}{G})^m \tag{2.5}$$

where σ_i is the internal stress. Setting m=3 and comparing Equations (2.4) and (2.5), gives:

$$\frac{\sigma_i}{G} = \frac{\sigma}{G} - C(\frac{\sigma}{G})^\beta \tag{2.6}$$

and $\beta = n/3$.

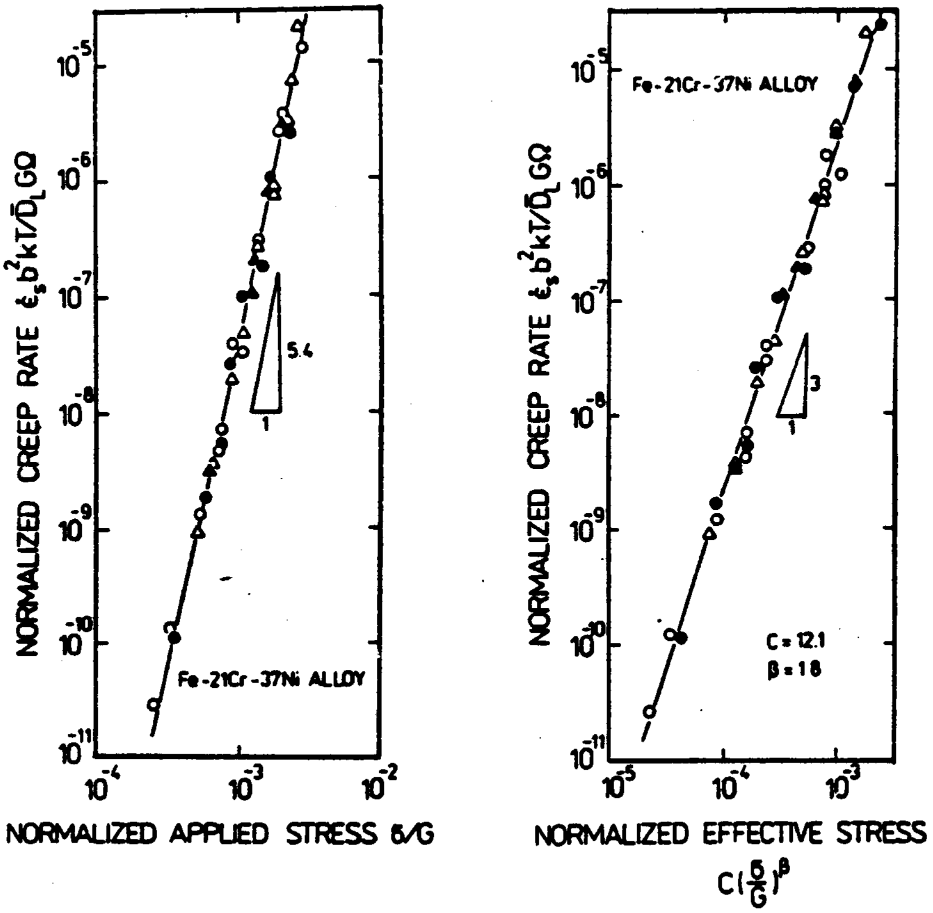

Figure 2-2 Phenomenological model utilizing back stress concept to explain discrepency in creep-stress dependence between theory and experiment: (a) the model without back stress; (b) the model with back stress.

With the above modification, Equation (2.5) can be used to explain the discrepency described earlier (see Figure 2-2). This model has proven successful for a number of metals, including aluminium, α-Fe, Cu-xZn solid solution alloys, and Ni-Cu austenitic stainless steels (Cadek, 1987). It is noticed that Equation (2.6) also indicates the internal stress varies as a function of applied stress in creep conditions.

Equations with a slightly different form have also revealed that significant variation in material parameters could occur without the internal stress term. For example:

$$\dot{\epsilon}_s = A\left(\frac{\sigma - \sigma_i}{G}\right)^n \frac{Gb}{kT} \exp\left(- \frac{Q_e}{RT}\right) \tag{2.7}$$

Where Q_e is the effective activation energy. With modification similar to Equation (2.3), models similar to Equation (2.7) have been successfully applied to polycrystalline nickel-base superalloys, including IN718 (Han and Chaturvedi, 1987a,b), IN738 (Steen et al., 1985), and NASAIR100 (Nathal and Ebert, 1987).

2.3 Experimental Evaluation of Internal Stress

The existence of internal stress implies that on unloading, if the applied stress is less than the internal stress, $\sigma<\sigma_i$, the material should exhibit a backward strain rate similar to that shown in Figure 1-8. To confirm Equations (2.5) and (2.7), several experimental techniques were developed in the past to determine σ_i. These include:

- Exhaustion of stress relaxation (Holbrook et al., 1981)
- Controlled unloading analysis (Swearengen and Holbrook, 1985)
- Analysis of Bauschinger effect (Miller and Ziaai-Moayyed, 1982; Lowe and Miller, 1983)
- Strain-transient dip test (Jones et al., 1982, 1983)

Details of each technique are summarized by Swearengen and Holbrook (1985) and Cadek (1987). All the above techniques have several things in common. First, they all depend upon interruption of the deformation process by maintaining one external variable constant (stress or strain) and subsequent observation of the plastic strain rate behavior during or after some amount of unloading. Second, these techniques also assume that the internal stress is the stress achieved on unloading, which produces a zero plastic strain rate. And last, with all these techniques except the strain-transient dip test, some plastic deformation must be created before σ_i can be measured (Swearengen and Holbrook, 1985).

In spite of the difficulty and accuracy of each technique, there are still some open questions:

- Does the internal stress remain constant during the change in external conditions?
- Is the measured variable precisely the one operating during inelastic flow?
- What are the effects of anelasticity?

The answers to these questions are still not clear (Swearengen and Holbrook, 1985). However, the concept of using internal stress as one of the state variables in material modeling has proven successful.

2.4 Physical Background For State Variables

A number of studies have tried to determine the explicit microstructural basis for internal variables (Alexopoulous et al., 1982; Alden, 1973; Turner, 1979; Turner and Hasegawa, 1982; Rhode et al., 1981; Kassner et al., 1977; Blum and Finkel, 1982). These microstructural patterns under study (e.g., dislocation density, forest density, subgrain size, subgrain misorientation) were all insensitive or insufficient to characterize the material state as determined by the mechanical response.

Use of the aggregate effect of the above patterns as the physical basis for a synthetic state variable, such as the internal stress, is easier than to use them individually. This is particularly important and appealing to state variable theory development. This approach has a broader picture of the material behavior and opens a larger area for interpreting different state variables. For example, the evolution of microstructure under low or high cycle fatigue was not considered by any of the four methods mentioned above. However, different microstructures and deformation mechanisms have been frequently observed for both loading conditions. This indicates that such a difference could be represented by different state variables.

As illustrated in Figure 1-8, the internal stress represents a measure of the resistence to dislocation glide. Therefore, when the internal stress build-up in the opposite direction of the dislocation glide is greater than the resolved shear stress in the direction of dislocation, a backward inelastic flow occurs.

Such an internal stress (or resistence) build-up can be attributed to several sources. For pure metals, these could be interactions between dislocations, cross-slip, interactions between soft and hard regions of the dislocation structure (Cadek, 1987), and most distinctly, the repulsive stress that arises when dislocations piled up against permanent barriers, such as grain boundaries. Strengthening mechanisms in alloys provide other sources for internal stress, including lattice resistance of the matrix, solid solution hardening of the matrix, ease of cross-slip, dislocation network, and, most markedly, precipitate hardening, and others.

From a microscopic point of view, the above processes are rather difficult to model individually because they are often coupled. The aggregate effect is also difficult to simulate when using only internal stress. However, all these effects have some similarities.

In general, these effects are either elastic or accumulative in nature. The elastic effect can be represented by a dislocation pile-up mechanism; i.e., when the applied stress is removed the pile-up is relaxed. This type of resistence was traditionally termed back stress because back leads to the meaning of stress in the opposite direction. The accumulative type of resistence, traditionally termed drag stress, can be represented by the precipitate hardening mechanism. Drag stress is used to simulate the resistance to inelastic flow; i.e., dislocation motions due to obstacles, such as precipitates (including the resistence when dislocations pass through or around the precipitates by means of a shearing or looping mechanism).

Deformation characteristics of different microstructures can alter the variation of back stress and drag stress. For example, if precipate shearing occurs there may be a small increase in drag stress relative to back stress. Alternatively, the presence of large unshearable precipates may increase drag and back stresses simultaneously. The independent influence of dislocation pile-ups and resistance have been assumed by several models. A typical drag stress/back stress model (Walker, 1981; Ramaswamy, 1985; Krempl et al., 1986) for polycrystalline metals has the functional form:

$$\dot{\epsilon}^{I}_{ij} = F\left(\frac{Z}{|\sigma_{ij}-\Omega_{ij}|}\right) \mathrm{sign}(\sigma_{ij}-\Omega_{ij}) \qquad (2.8)$$

where Z is the drag stress and Ω_{ij} is the back stress. The scalar form of the drag stress indicates its accumulative properties. Whereas, back stress takes the tensorial form representing its stress character. The independent influence of back stress and drag stress is assumed in many models; e.g., back stress is usually for modeling short-term strain hardening and drag stress is for modeling long-term cyclic hardening.

2.5 Back Stress in Single Crystals

Dame and Stouffer (1985) assumed that back stress should not be present or, if present, it should be negligible in single crystal alloys because of lack of grain boundaries (the main source of back stress build-up). Thus, only the drag stress was included in their model. Assuming that back stress can only be created by a dislocation pile-up mechanism is too restrictive as discussed earlier that other mechanisms may also be operative.

Milligan and Antolovich (1987) showed in their study of deformation behavior of single crystal superalloy PWA1480, that when dislocations emerge from precipitates, constrictions of the dislocations occur because of high anti-phase boundary energy (APBE). That is, portions of the dislocation which exit the precipitates are split because of elastic repulsion. This suggests that elastic repulsion (i.e., a form of back stress) should be a component in the local force equilibrium equation.

Other mechanisms have also been suggested for single crystals (Jackson, 1985, 1986). These include cross-slip, which establishes a framework of dislocation cells; secondary slip, which completes the formation of relatively stress-free dislocation cells; and local slip within dislocation-rich load-bearing cell walls.

Experimental evidence supports the existence of back stress in nickel-base single crystals. Swanson and co-worker (1984) tested PWA1480 under cyclic loading conditions with strain or stress hold interruption, and observed backward (negative) inelastic flow at tensile (positive) stress hold (Figure 1-8). An early goal in this research was to confirm the existence of back stress for the Rene N4 at 982°C.

Examination of Equation (2.8) reveals a method to evaluate the existence, not the magnitude, of back stress. Setting the applied stress, σ_{ij}, equal to zero after significant plastic strain to establish back stress build-up, a negative inelastic flow should be observed. Using this hypothesis, two specially designed mechanical tests on single crystal Rene N4 were conducted early in the research period to verify the existence of back stress in the proposed inelastic flow equation.

Figures 2-3 and 2-4 show the results of double tensile tests on specimens in [100] and [111] orientation, respectively, with a 120 second hold at zero stress. In both tests, samples were first loaded to 1.5% strain at a strain rate of $1x10^{-4}$/sec, unloaded immediately to zero stress within 10 seconds, and then reloaded at a higher strain rate of $6x10^{-4}$/sec following the 120 second hold period. Shown in Figure 2-5 are inelastic strain-time histories during hold period for both samples. Significant anelastic recovery occurred during the hold period for the [100] sample. Whereas the recovery is minimal for the [111] oriented specimen.

These results clearly demonstrate the existence of internal stress and the orientation dependency of the recovery mechanism. They also indicate that without the presence of the back stress term similar to Equation (2.8), a single drag stress formulation cannot predict this

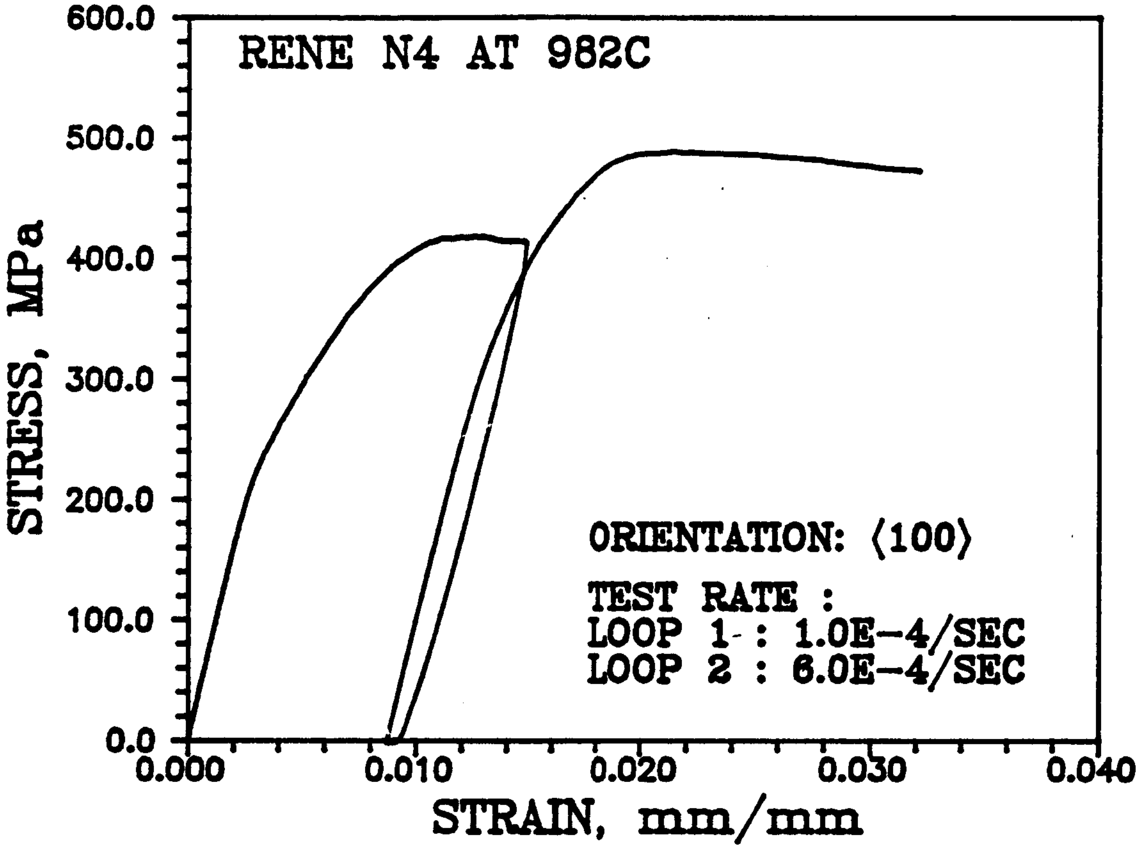

Figure 2-3 Double Tensile Test In The [100] Orientation With A 120 Second Hold Period

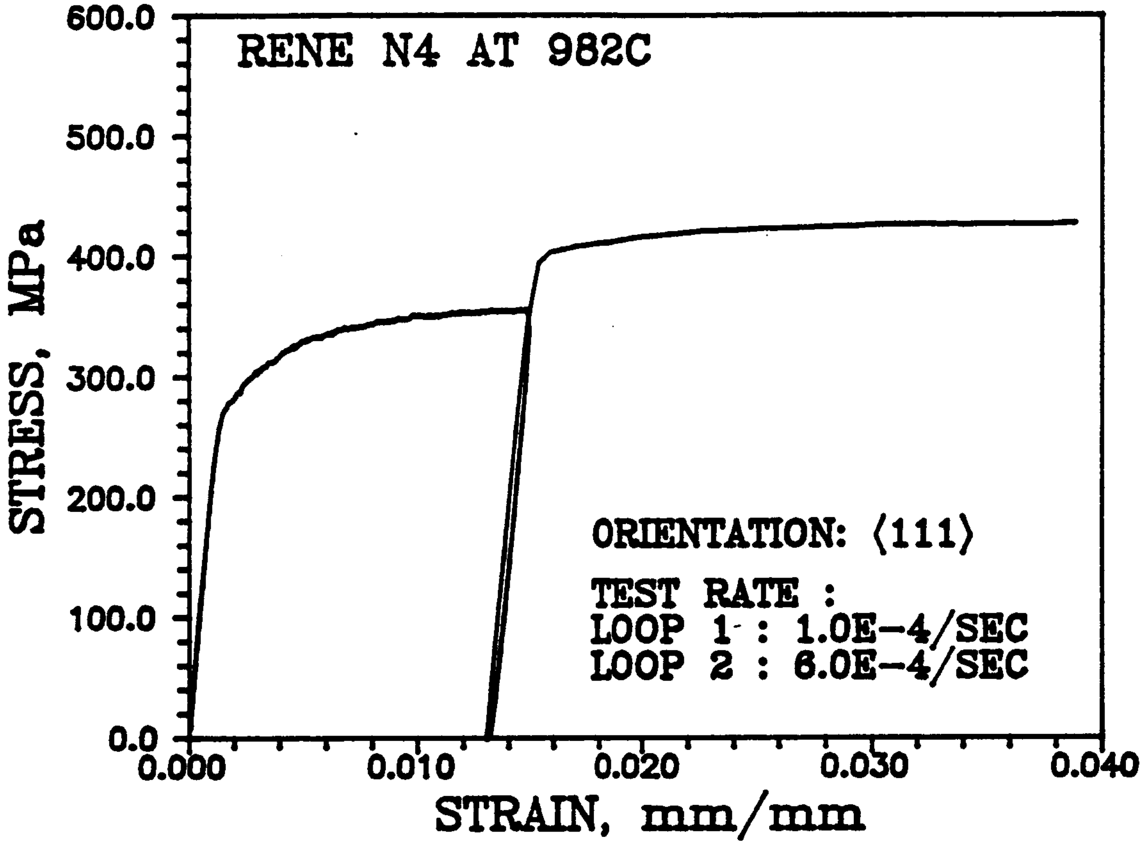

Figure 2-4 Double Tensile Test In The [111] Orientation With A 120 Second Hold Period

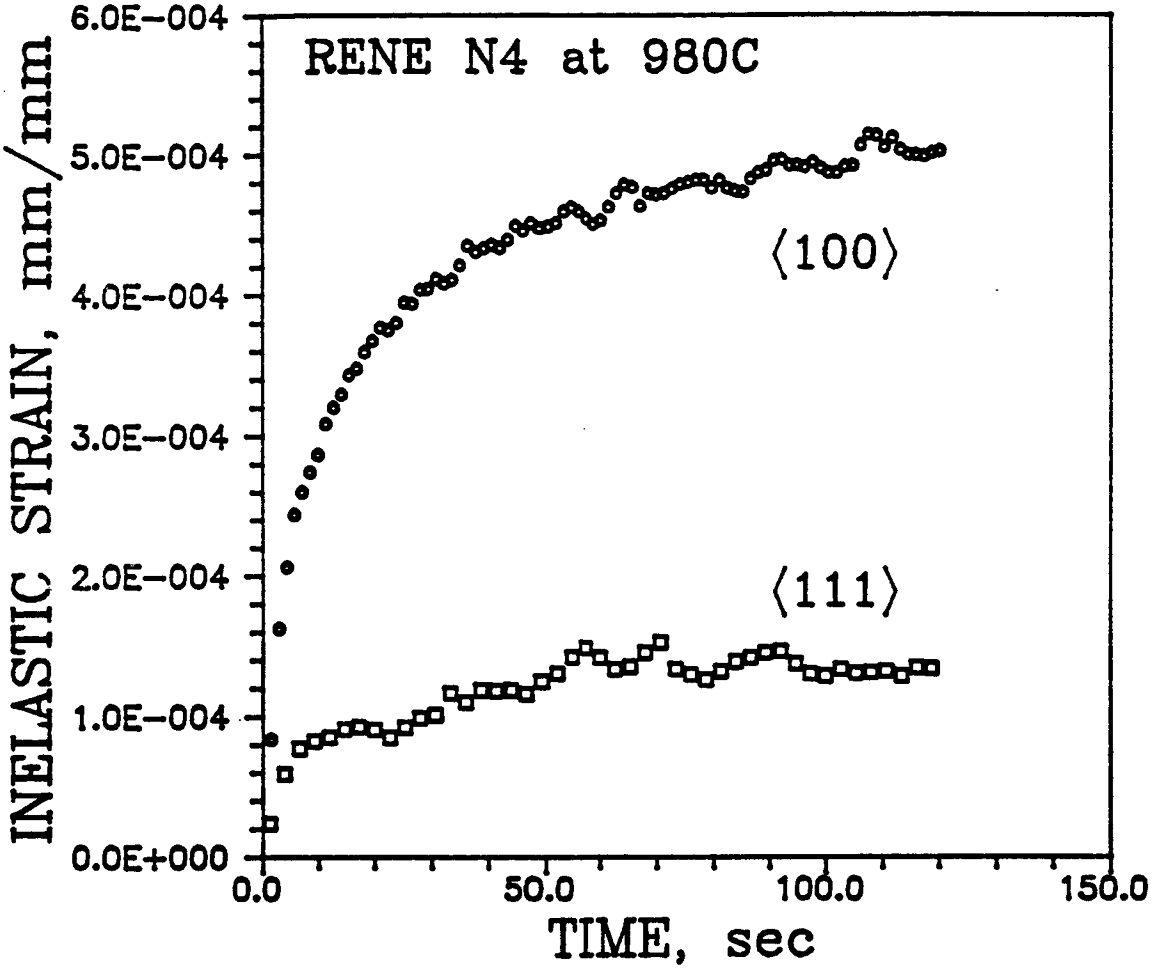

Figure 2-5 Inelastic Strain-Time Histories For The [100] And [111] Orientations During The 120 Seconds Hold Period In The Double Tensile Test

anelastic behavior. These experiments motivated the development of a new model which uses back stress and drag stress for single crystal superalloys at elevated temperatures. The development of this model is discussed in the next two chapters.

CHAPTER III

DEFORMATION MECHANISM OF NICKEL-BASE SINGLE CRYSTAL SUPERALLOYS

Constitutive modeling based on the crystallographic approach requires extensive understanding of the deformation mechanisms of the material at various temperatures and loading conditions. The deformation mechanism affects the formulation of kinematic equations that transform the calculations at crystallographic (or local) level to macroscopic (or global) level. Because of this relationship between material modeling and deformation physics, this chapter is focused on the deformation mechanisms of nickel-base single crystals at elevated temperatures.

The active slip systems for nickel-base superalloy single crystals, which depend on crystal orientation with respect to the stress axis, temperature, and strain rate, could involve one or more types of slip. These slip systems include:

- Slip on the four octahedral planes in the three directions similar to the $[\bar{1}01]$ direction
- Slip on the four octahedral planes in the three directions similar to the $[\bar{1}2\bar{1}]$ direction
- Slip on the three cube planes in the two directions similar to the $[\bar{1}01]$ direction

There are thirty possible slip systems in total. A slip system number has been assigned to each slip system as given in Table 3-1. Detailed descriptions of each slip system appear in Appendix A.

These slip sytems are not operative simultaneously. Slip systems is activated depending upon the loading conditions and temperatures.

Table 3-1 List Of Slip Plane And Slip Direction For Each Slip System And The Associated Slip Number.

SLIP NO.	SLIP PLANE	SLIP DIRECTION*
	OCTAHEDRAL SLIP a/2<110>{111}	
1	[1 1 1]	[1 0 -1]
2	[1 1 1]	[0 -1 1]
3	[1 1 1]	[1 -1 0]
4	[-1 1 -1]	[1 0 -1]
5	[-1 1 -1]	[1 1 0]
6	[-1 1 -1]	[0 1 1]
7	[1 -1 -1]	[1 1 0]
8	[1 -1 -1]	[0 -1 1]
9	[1 -1 -1]	[1 0 1]
10	[-1 -1 1]	[0 1 1]
11	[-1 -1 1]	[1 0 1]
12	[-1 -1 1]	[1 -1 0]
	OCTAHEDRAL SLIP a/2<112>{111}	
13	[1 1 1]	[-1 2 -1]
14	[1 1 1]	[2 -1 -1]
15	[1 1 1]	[-1 -1 2]
16	[-1 1 -1]	[1 2 1]
17	[-1 1 -1]	[1 -1 -2]
18	[-1 1 -1]	[-2 -1 1]
19	[1 -1 -1]	[-1 1 -2]
20	[1 -1 -1]	[2 1 1]
21	[1 -1 -1]	[-1 -2 1]
22	[-1 -1 1]	[-2 1 -1]
23	[-1 -1 1]	[1 -2 -1]
24	[-1 -1 1]	[1 1 2]
	CUBE SLIP a/2<110>{100}	
25	[1 0 0]	[0 1 1]
26	[1 0 0]	[0 1 -1]
27	[0 1 0]	[1 0 1]
28	[0 1 0]	[1 0 -1]
29	[0 0 1]	[1 1 0]
30	[0 0 1]	[-1 1 0]

* The direction expressed by the Miller indices does not represent the unit vector in the direction.

Combination of the effect from active slip systems produces a far more complicated mechanical response for single crystal superalloys than for polycrystalline superalloys. For example, the anomalous yielding behavior and orientation dependence for the single crystal alloys (see Figure 1-5).

In the following reviews, particular attention is given to the type of deformation mechanisms and corresponding kinematic relationships; the relationship between time, strain rates, applied stress or resolved shear stress or both, and accumulated work; the components that establish the state variable evolution equations. This information can be obtained by correlating the mechanical test data with the TEM (transmission electron microscopy) analysis of tested samples. Because the inelastic material behavior has high strain rate (plasticity) and low strain rate (creep) characteristics, each strain rate domain must be analyzed separately in order to obtain the most appropriate information for the development of the constitutive equations.

3.1 High Strain Rate Deformation Mechanism

Milligan and Antolovich (1987) thoroughly investigated the yielding and deformation behavior of single crystal superalloy PWA1480 in the temperature range from 20 to 1093°C at strain rates of 0.5 and 50%/min. This study showed that at low temperatures (20°C to 760°C) the deformation for loading in the [001] orientation with 0.1-0.3% plastic strain was dominated by pairs of $a/2\langle 110\rangle\{111\}$ dislocations shearing through the γ'. In this temperature range, dislocations traveled through the γ' as closely-spaced pairs in order to minimize the antiphase boundary (APB) area created by the a/2<110> displacement of the superlattice (Flinn, 1966).

In contrast to the shearing mechanism observed at low temperature, γ' bypass mechanism was predominant for small strain deformation at temperatures of 815°C and up. For specimens tested to failure at 871° and 982°C, high dislocations density within the γ' was observed. The occurrence of high density of dislocations indicated that early in the test, deformation was controlled by looping or bypass of the γ' and was followed by shearing of the γ' later in the test. Shearing of the γ' was also observed after a large increase in the matrix dislocation density and significant strain hardening. In the intermediate temperature range, from 760°C to 927°C, a transition from shearing to bypass deformation mechanism was observed (Milligan and Antolovich, 1987).

Miner et al. (1986) tested single crystal Rene N4 at 760°C and 980°C. They reported that primary cube slip supplanted normal octahedral slip for loading in the $[\bar{1}12]$ orientation during tensile tests, whereas, tensile loading near both [100] and [110] crystallographic directions exhibited only octahedral slip at all temperatures. It was also observed that for loading in orinetations near the $[\bar{1}12]$ direction at 760°C, some a/2<$\bar{1}$10> dislocations were found in widely spaced pairs in the γ' phase. Wide spacing is indicative of low antiphase boundary energy between two dislocations on the cube plane (Flinn, 1960). This finding seems to suggest that back stress may be different for octahedral and cube slip, which is consistent with results presented in Section 2.5, Chapter II.

For Rene N4 at elevated temperatures, cube slip occurred for specimens having orientation in $[\bar{1}11]$, $[\bar{1}12]$, $[\bar{1}67]$ and [023] directions. Whereas, octahedral slips were found for specimens in the [001], [011], [023], $[\bar{1}67]$, $[\bar{1}26]$ and $[\bar{2}36]$ orientations at 870°C and 980°C (Miner et al., 1986b). This result, as illustrated in Figure 3-1 through use of the stereographic triangle, indicates that deformation mechanisms are mixed octahedral and cube slip at high strain rate loading conditions. This rule does not apply to the entire stereographic triangle, however, near the [100] orientation only octahedral slip occurs and near the [111] orientation only cube slip occurs for all temperatures.

3.2 Low Strain Rate Deformation Mechanism

Studies on the orientation and temperature dependence of the creep properties of nickel-base superalloy single crystals (Kear and Piearcey, 1967; MacKay et al., 1980, MacKay, 1981) have revealed that substantial improvement in the creep life occurred between 760°C and 871°C for the crystals with orientations near [001] or $[\bar{1}11]$ directions. Conversely, very short lives were exhibited by single crystals with orientation near the [011] direction. At a higher temperature, crystallographic orientation had less influence on the creep life. The reduction in influence of crystal orientation with increasing temperature on creep life is believed to result because additional slip systems become operative at elevated temperatures (Kear and Piearcey, 1967).

Studies on the creep deformation of MAR-M200 single crystals at 760°C and 857°C (Leverant and co-workers, 1969, 1970, 1973) reported that primary creep occurred on <112>{111} slip systems rather than on

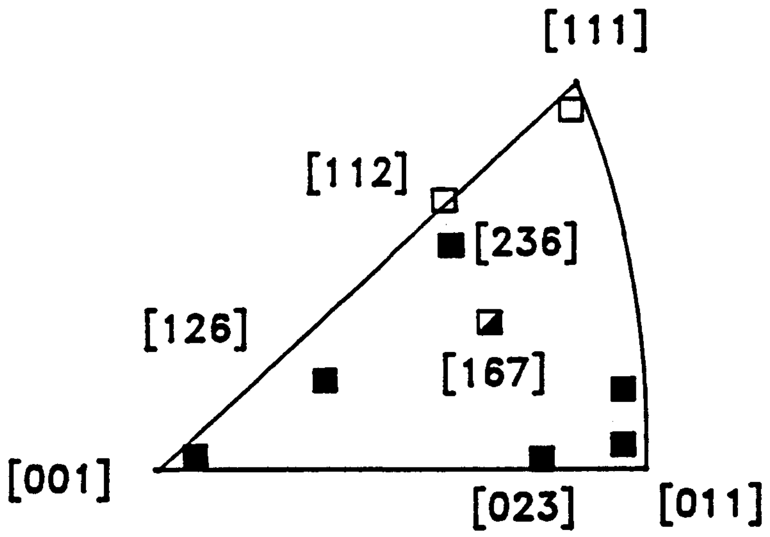
[111]
[112]
[236]
[126]
[167]
[001]
[023]
[011]

Figure 3-1 Orientations Of Single Crystals That Exhibited Octahedral Slip (symbol □) or cube slip (symbol ■) or mixed Octahedral And Cube Slip (symbol ◪).

<110>{111} systems. It was determined that (a/2)<112> dislocations were generated and dissociated into (a/6)<112> and (a/3)<112> superpartials. These (a/3)<112> superpartial dislocations then controlled the primary creep by a diffusion-assisted process.

Secondary creep begins only after sufficient strain hardening occurs because of the interaction of the <112>{111} slip systems. An activation energy study (Tien et al., 1972) suggested that secondary creep deformation occurred by the shearing of the γ' by (a/2)<110> dislocation pairs. For creep tests at 857°C, pairs of (a/2)<110> dislocations were observed to shear the γ' in both primary and secondary creep domains (Leverant et al., 1973).

In the creep study by Leverant and Kear on MAR-M200 at 760°C and 689MPa (1970), primary creep strain and primary creep rate were reported to increase with orientation in the following order: [001] tensile axis, tensile axis on $[001]$-$[0\bar{1}1]$ boundary, tensile axis between $[001]$-$[0\bar{1}1]$ and $[001]$-$[1\bar{1}1]$ boundaries, and tensile axis on $[001]$-$[1\bar{1}1]$ boundary. The secondary creep rate increases with orientation, in order similar to the primary creep rate, but does not exhibit as large a variation as the primary creep rate.

The Schmid factors and multiplicity of slip for the <112>{111} slip systems were used to correlate the orientation dependence of the creep in single crystal MAR-M200 by Laverant and Kear (1970). Their results showed that, along the $[001]$-$[0\bar{1}1]$ duplex slip boundary, the primary creep strain and primary creep rate followed the same variation pattern as the Schmid factor (shown in Figure 3-2); i.e., the values increase to a maximum and then decrease. Also, crystals in single slip orientations exhibit the largest primary creep strains and rates.

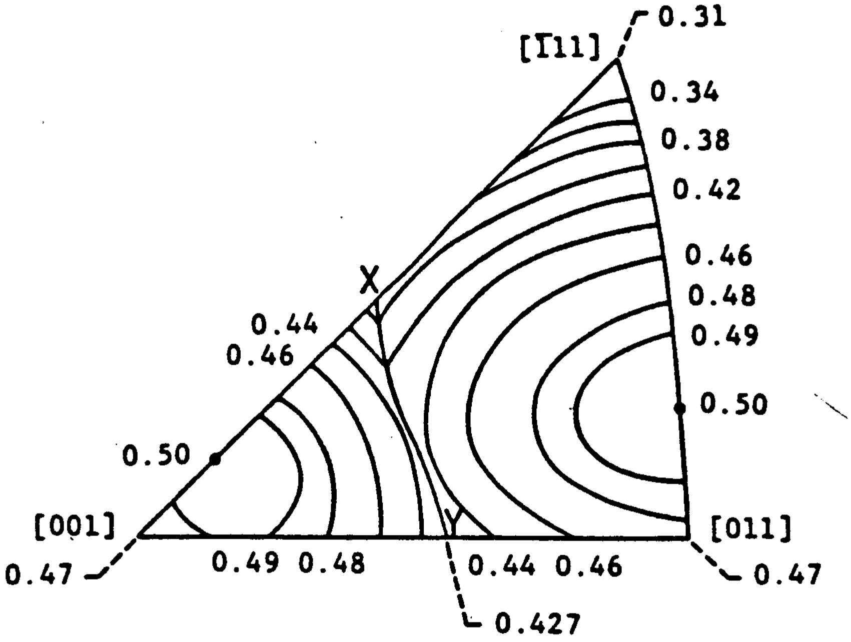
0.31
[1̄11]
0.34
0.38
0.42
0.46
0.48
0.49
0.50
X
0.44
0.46
0.50
[001]
0.47
0.49 0.48
Y
0.44 0.46
0.427
[011]
0.47

Figure 3.2 Schmid factor contour for <112>{111} slip systems.

Milligan and Antolovich (1987) observed that specimens tested under creep conditions at stresses equal to 70-80% of the low strain rate yield strength exhibited a similar type of deformation microstructure to those developed during yielding. The only difference between tensile and creep was the increased γ' coarsening during creep.

Recent studies on creep properties of single crystal MAR-M247 at 774°C and 724MPa (MacKay and Maier, 1982) and single crystal SRR99 at 750°C and 800MPa (Hopgood and Martin, 1986) showed that stress rupture life is greatly influenced by the lattice rotation required to produce intersecting slip. Secondary creep does not begin until the onset of duplex slip. MacKay and Maier also summarized that specimens required a large rotation to initiate duplex slip produced a large primary creep strain, a large effective stress level (defined as $(\epsilon_s + 1)P/A_0$, where ϵ_s is the strain at onset of secondary creep, P/A_0 is the nominal stress) at the onset of secondary creep, and a shorter creep rupture life.

In the above creep studies on various nickel-base single crystal superalloys, strain at the onset of secondary creep ranged from 6% to 10% for specimens having orientations 5° to 10° from the [100] orientation. These strains are in the range which small strain theory can not apply. MacKay and Maier (1982) showed that the elongation required for a crystal gliding in single slip to rotate into duplex slip orientation is primarily controlled by the amount of rotation. Thus, crystal rotation is an element essential for calculating the primary creep response.

3.3 Crystal Lattice Rotation During Creep

During plastic deformation, single crystals in a single slip orientation rotate toward their slip direction. The direction of rotations within the stereographic triangle is shown in Figure 3-3 for crystals that deform by <112>{111} slip systems. There are two different regions of rotation; e.g., crystal rotation toward $[2\bar{1}\bar{1}]$ pole in region I and toward the [112] pole in region II.

The two regions of rotation are separated by a boundary (X,Y) where the Schmid factor is 0.427. The [100]-Y and X-[111] boundaries exhibit duplex slip in the stereographic triangle. Duplex slip occurs when Schmid factors are identical for two slip systems, and thus equal slip activities can occur on both slip systems. In Figure 3-3, note that because both [100] and [111] orientations exhibit maximum crystallographic symmetry, no lattice rotation occurs.

At temperatures near and above 760°C, single crystals oriented within the borders of the stereographic triangle initially deformed during creep by single glide and rotation, as indicated by the arrows in Figure 3-3. After the crystal orientation reached a duplex boundary, the transition from primary to secondary creep began. This transition was completed only after sufficient intersecting slip between the <112>{111} slip systems strain-hardened the material (Leverant and Kear, 1970). During secondary creep, the $[\bar{1}01](111)$ slip systems were deduced to be operative (Levarent and Kear, 1970); however, that analysis of crystal rotation did not seem to support this argument (MacKay and Maier, 1982).

Experimental evidence provided by Mackay and Maier (1982) showed that crystals with orientations within approximately 25° of the [001] pole exhibited longer lives when their orientations were nearer to the [001]-[011] boundary of the stereographic triangle than to the [001]-[111] boundary. From Figure 3-3, those specimens which are close to the [001]-[011] boundary require smaller amounts of rotation to produce

CRYSTAL LATTICE ROTATION

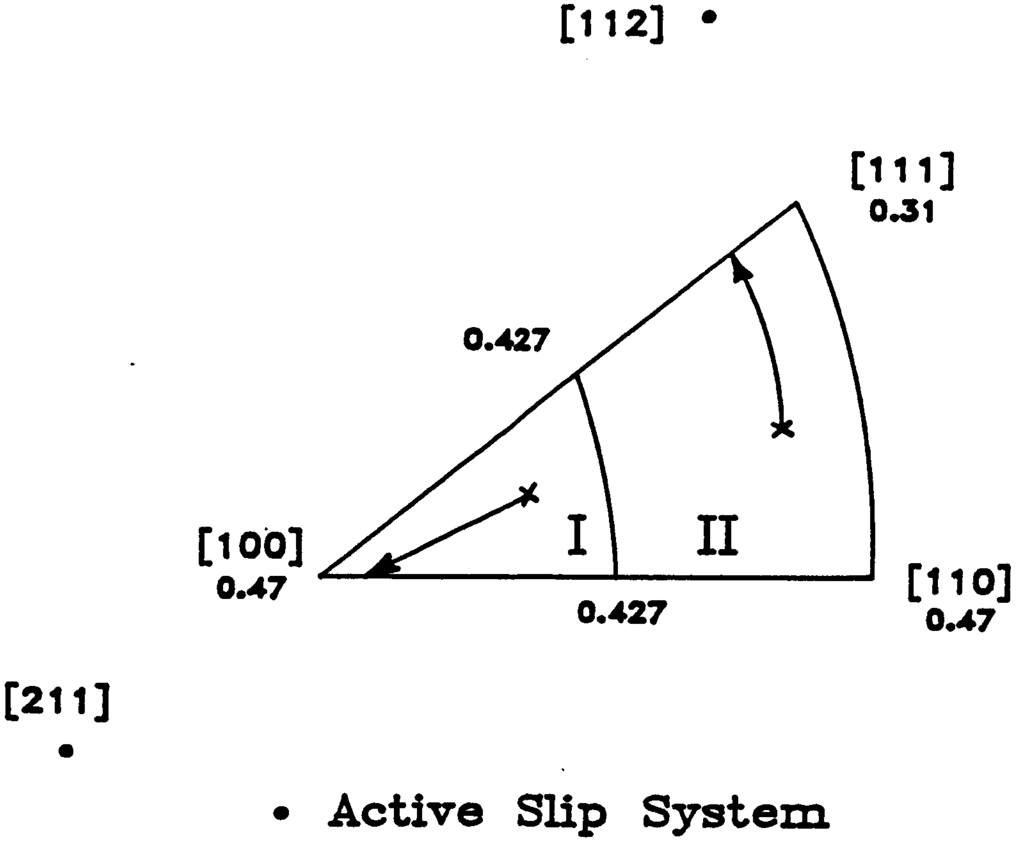
[112]
[111]
0.31
0.427
[100]
0.47
I
II
0.427
[110]
0.47
[211]
• Active Slip System

Figure 3-3 Directions Of Crystal Lattice Rotation In Standard Stereographic Triangle For Single Crystals Under <112>{111} slip.

duplex slip and reach the onset of secondary creep.

The MacKay/Maier study also showed that the steady state creep rates were increasing with the increasing specimen angle off the [100] orientation. For example, steady state creep rate for specimens 10^0 off the [100] are approximately two to three times larger than crystals only 5^0 off the [100]. These results are consistent with the creep study by Leverant and Kear(1970) on single crystal MAR-M200.

For a better understanding of the relationship between creep properties and the lattice rotation, the data on MAR-M247 reported by MacKay and Maier (1982) were graphically analyzed in Figure 3-4. The accumulated primary creep strain, as shown in Figure 3-4a, is generally proportional to the angle away from the [100] pole. However, the secondary creep rate is in better agreement to the trend of Schmid factor, as illustrated in Figures 3-4b and 3-4c, respectively.

3.4 Summary Of Physcial Backgroung For Single Crystal Constitutive Model

The overview of deformation mechanisms in the previous sections and the state variable concept in Chapter II provides the physical background for building the constitutive model. This important information is summarized below:

- The need for a back stress state variable in the proposed inelastic flow equation is evidenced in the double tensile experiments (Figures 2-4 and 2-5).
- Experimental evidence in Figures 2-4 and 2-5 and the spacing between superpartial dislocations in γ' for ctahedral and cube slip indicates that the back stress in octahedral and cube slip systems may not be the same.

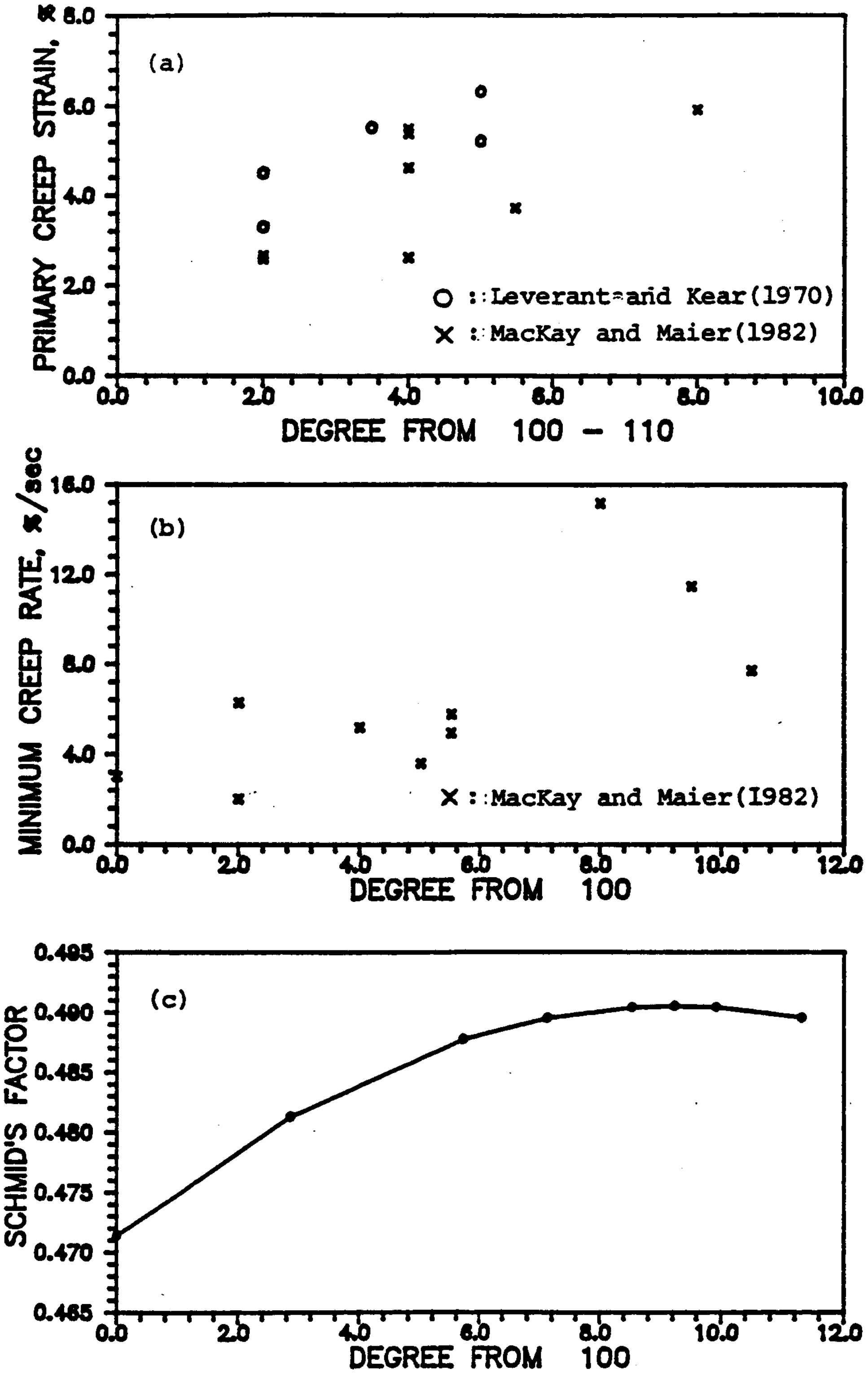

Figure 3-4 MAR-M247 Creep Data Shown As A Function Of Orientation For Single Crystals Tested At 774°C And 724MPa: (a) Primary Creep Strain; (b) Secondary Creep Rate; and (c) the Schmid factor along the [100]-[110] boundary.

- Back stress is a function of the applied stress for creep loading condition.
- The active slip systems at intermediate to high temperatures involve mixed octahedral, a/2<110>{111}, and cube, a/2<110>{100}, slip for high strain rate single crystal deformation. However, pure octahedral slip is observed for [100] orientation at all temperatures.
- At intermediate to high temperature, low strain rate single crystal deformation is controlled by octahedral slip of the <112>{111} type.
- The deformation mechanisms of bypass and shearing of γ' were not representative of either high or low strain rate deformation; thus, they need ot be treated separately in the drag stress.
- Crystal lattice rotation is observed in creep samples and is shown to dominate the primary creep response.
- Two distinct crystal rotation characteristics exist (see Figure 3-3) in the stereographic triangle.

CHAPTER IV

ANISOTROPIC CONSTITUTIVE MODEL DEVELOPMENT

The objectives of the current model are two fold: the ability to predict single crystal tensile, cyclic fatigue, and creep responses at isothermal conditions. In particular, the ability to model the anisotropic characteristics such as orientation dependence, elastic modulus, strain hardening characteristics, tension/compression asymmetry, and lattice rotation.

Following concepts used by Dame and Stouffer, the current model is also based on the unified theory which separates the total strain into elastic and inelastic components. The elastic strain is calculated from cubic symmetry and the inelastic strain is computed by summing the contribution of slip on each slip system. The local inelastic strain rate of each slip system is calculated by using a local flow equation similar to Equation (2.8).

Based on the physical background summarized in Scetion 3.4, Chapter III, formulation of the current model follows the requirements below:

- Three separate inelastic flow equations are required for each type of slip.
- High strain rate single crystal responses (i.e., tensile and cyclic fatigue) are modeld by using the octahedral, a/2<110>{111}, and cube, a/2<110>{100}, slip systems.
- Low strain rate single crystal responses (i.e., creep) are modeled by using the octahedral a/2<112>{111} slip systems. Although a/2<112>{111} dislocations disociate into a/3<112>{111} and a/6<112>{111} superpartials, the current model only

considers the aggregate effect; e.g., deformation in the <112> slip directions on the octahedral planes.

- Tension/compression asymmetry needs to be modeled through use of the octahedral a/2<110>{111} slip systems.
- Back stress state variable is required for the current model to account for the anelastice recovery.
- Separate evolution equations for state variable in each slip system are required to simulate the evolution of microstructure during deformation because of various active slip systems.
- Crystal lattice rotation during creep indicates that such behavior may be a time-dependent material property; hence, it should be modeled by using the octahedral a/2<112>{111} slip systems.
- Two rotational kinematic rules are required for each of the two rotation characteristics within the stereographic triangle.
- Large primary creep strain because of crystal lattice rotation in diffusion-controlled creep, suggests the need for a finite strain formulation.

4.1 Local and Global Kinematic Relationships

Because the constitutive equations are applied at the crystallographic level, the kinematic relationships is required to relate the stress tensor and the resolved shear stresses on the slip systems. The stress vector σ_j on a slip plane α is given by:

$$\sigma_j = \sum_i \sigma_{ij} n_i^{\alpha} \qquad (4.1)$$

where σ_{ij} is the applied stress tensor in the material principal axes and $\underset{\sim}{n}^{\alpha}$ is the unit vector normal to the α plane. The resolved shear stress component in the β direction on the α plane is given by:

$$\tau^{\alpha\beta} = \sum_{j} \sigma_j \ell_j^{\alpha\beta} \tag{4.2}$$

where $\underset{\sim}{\ell}^{\alpha\beta}$ is the unit vector in the β direction on the α plane. Substituting σ_j in the above equation by using Equation (4.1) gives:

$$\tau^{\alpha\beta} = \sum_{ij} \sigma_{ij} \, n_i^{\alpha} \, \ell_j^{\alpha\beta} \tag{4.3}$$

i.e., transformation between global stress, in principal axes of the material, and local shear stress components on each slip plane in each slip direction. The sign conventions of $\underset{\sim}{n}^{\alpha}$ and $\underset{\sim}{\ell}^{\alpha\beta}$ for each slip system and the details of Equation (4.3) are given in Appendix A.

The relationship between the crystallographic shear strain rates and the macroscopic inelastic strain rate tensor is also necessary. In Dame and Stouffer's model (1985), the rate of displacement of a point located at x_i because of a uniform shear strain rate $\dot{\gamma}^{\alpha\beta}$ parallel to the β direction in the α plane is assumed to be:

$$\dot{u}_i = \sum_{j} \dot{\gamma}^{\alpha\beta} \, n_j^{\alpha} x_j \ell_i^{\alpha\beta} \tag{4.4}$$

The sum for all planes and slip directions and application of the linear strain displacement relation:

$$\dot{\epsilon}_{ij} = \frac{1}{2} \left(\frac{\partial \dot{u}_i}{\partial x_j} + \frac{\partial \dot{u}_j}{\partial x_i} \right) \tag{4.5}$$

gives the relationship between the crystallographic shear strain rates and global strain rates, $\dot{\epsilon}_{ij}$; that is:

$$\dot{\epsilon}_{ij} = \sum_{\alpha\beta} \frac{1}{2} \dot{\gamma}^{\alpha\beta}(\ell_i^{\alpha\beta} n_j^{\alpha} + \ell_j^{\alpha\beta} n_i^{\alpha}) \quad . \tag{4.6}$$

The assumed displacement field (as illustrated in Figure 4-1) is solely contributed by the shear strain in the plane which contains the slip plane normal, $\underset{\sim}{n}^{\alpha}$, and slip direction, $\underset{\sim}{\ell}^{\alpha\beta}$. However, this displacement field does not correspond to a pure shear condition. Instead, this field also contains a rigid body rotation with respect to the axis determined by $\underset{\sim}{\ell}^{\alpha\beta} \times \underset{\sim}{n}^{\alpha}$ (e.g., $\underset{\sim}{z}$ in Figure 4-1). The corresponding rate of spin tensor, calculated from the displacement field, is:

$$\dot{\omega}_{ij} = \frac{1}{2} \left(\frac{\partial \dot{u}_i}{\partial x_j} - \frac{\partial \dot{u}_j}{\partial x_i} \right) \tag{4.7}$$

Replacing $\dot{u}_i$ in Equation (4.7) using Equation (4.4) yields:

$$\dot{\omega}_{ij} = \sum_{\alpha\beta} \frac{1}{2} \dot{\gamma}^{\alpha\beta}(\ell_i^{\alpha\beta} n_j^{\alpha} - \ell_j^{\alpha\beta} n_i^{\alpha}) \tag{4.8}$$

This rate of rigid body rotation does not comply with the nature of crystal lattice rotation. For creep samples near the [110] orientation, there are two equally active slip systems in the $<\bar{1}\bar{1}2>$ and <112> direction, respectively. Because of symmetry, Equation (4.8) predicts no lattice rotation. However (as illustated in Figure 3-3) these samples exhibited the greatest amount of lattice rotation for <112>{111} slip system. In contrast, single slip specimens showed insignificant amounts of lattice rotation during the high strain rate tests. This

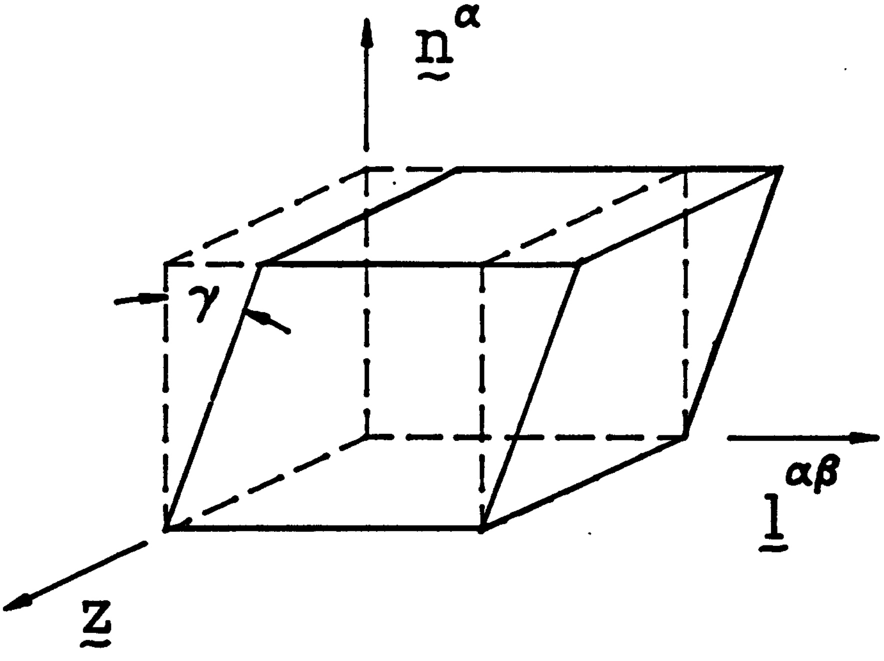
$\underset{\sim}{n}^{\alpha}$
γ
$\underset{\sim}{1}^{\alpha\beta}$
$\underset{\sim}{Z}$

Figure 4-1 Displacement Field Assumed In Dame And Stouffer's Model

indicates the rate of rotation, $\dot{\omega}_{ij}$, calculated by Equation (4.8) may not be proportional to the local slip rate, $\dot{\gamma}^{\alpha\beta}$.

In the current study, the above assumption of the displacement field is modified. A displacement field is proposed to include a pure shear to account for the inelastic strain. The lattice rotation, however, is calculated by using another set of kinematic equations.

For a single-slip system which is operative under monotonic low strain rate loading condition, crystal rotates toward its slip direction. Therefore, the plane of local lattice rotation contains the unit vector in the slip direction, $\underline{\ell}^{\alpha\beta}$, and the unit vector along the tensile axis, $\underline{s}$ (which is also the current crystal orientation [hkℓ]). As illustrated in Figure 4-2a, the rotation plane normal, $\underline{n}^{\kappa}$, is calculated by:

$$\underline{n}^{\kappa} = (\underline{\ell}^{\alpha\beta} \times \underline{s})/|\underline{\ell}^{\alpha\beta} \times \underline{s}| \qquad (4.9)$$

which is different from the $\underline{z}$ axis in Figure 4-1.

Thus the displacement field is proposed to comprise two independent elements; a pure shear (Figure 4-2b) and a pure rotation (Figure 4-2a). The inelastic strain rate in the principal material axes is given by Equation (4.6) and the rate of lattice rotation is calculated by:

$$\dot{\omega}_{ij} = \sum_{\kappa\beta} \frac{1}{2}\, \dot{\omega}^{\kappa\beta}(\ell_i^{\alpha\beta} n_j^{\kappa} - \ell_j^{\alpha\beta} n_i^{\kappa}) \qquad (4.10)$$

where $\dot{\omega}^{\kappa\beta}$ is the rate of local lattice rotation about the axis $\underline{n}^{\kappa}$. Note that slip plane α and rotation plane κ intercept each other along the

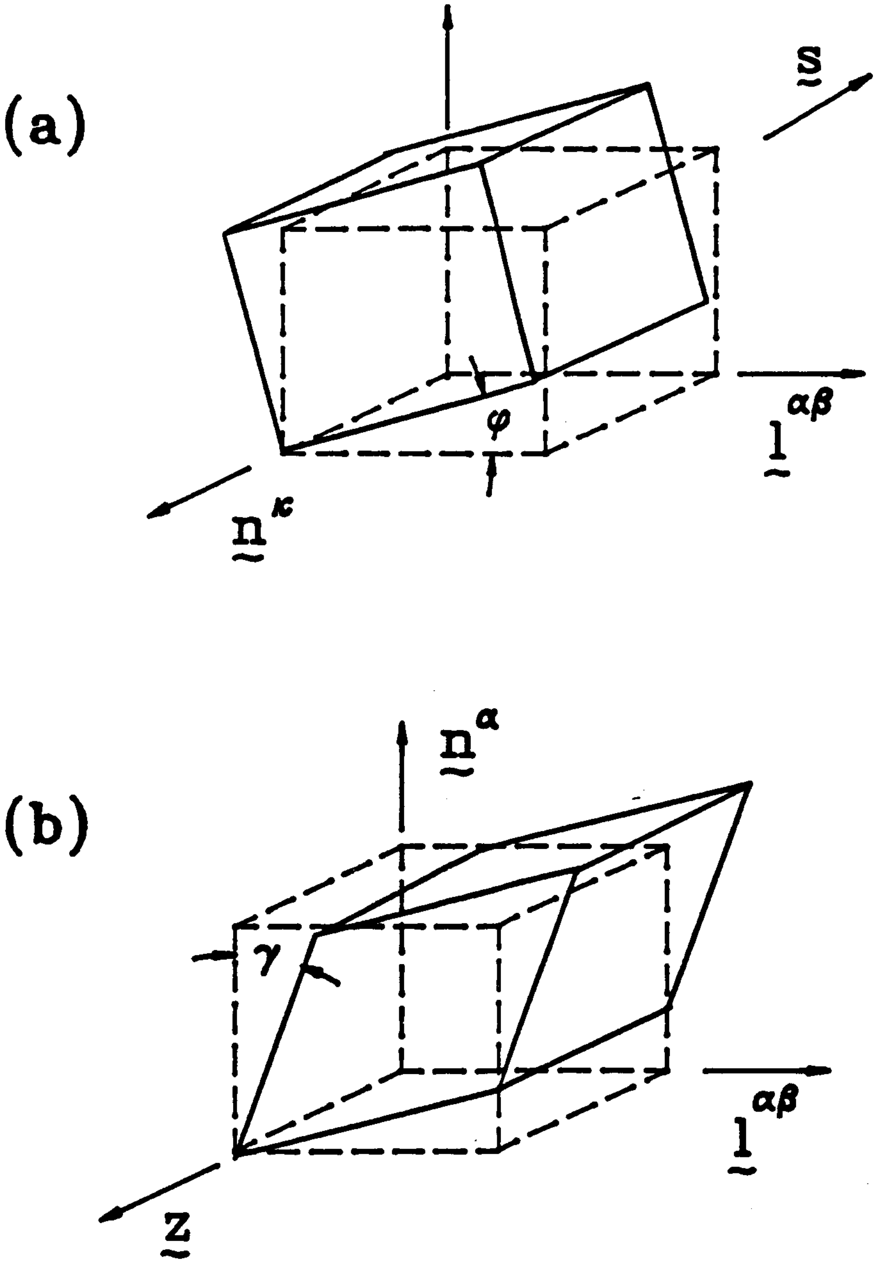

Figure 4-2 The proposed kinematics in the current model: (a) A Pure Rotation In The κ Plane (Plane Normal $\underset{\sim}{n}^{\kappa}$) and (b) A Pure Shear On The α Slip Plane (Plane Normal $\underset{\sim}{n}^{\alpha}$) In The β Direction

slip direction $\ell_i^{\alpha\beta}$.

4.2 The Constitutive Equations

The constitutive model is based on unified theory that separates the total strain into elastic, inelastic, and thermal components only, that is:

$$\epsilon_{ij}^{T} = \epsilon_{ij}^{E} + \epsilon_{ij}^{I} + \epsilon_{ij}^{\theta} \tag{4.11}$$

where ϵ_{ij}^{T} is the total strain, ϵ_{ij}^{E} is the elastic strain component, ϵ_{ij}^{I} is the inelastic strain component, and ϵ_{ij}^{θ} is the thermal strain component. Elastic strains are computed according to cubic symmetry and the applied stress tensor. The elastic constitutive equation in the material principal axes can be written as:

$$\begin{bmatrix} \epsilon_{11} \\ \epsilon_{22} \\ \epsilon_{33} \\ \epsilon_{23} \\ \epsilon_{31} \\ \epsilon_{12} \end{bmatrix}^{E} = \begin{bmatrix} \frac{1}{E} & -\frac{\nu}{E} & -\frac{\nu}{E} & 0 & 0 & 0 \\ -\frac{\nu}{E} & \frac{1}{E} & -\frac{\nu}{E} & 0 & 0 & 0 \\ -\frac{\nu}{E} & -\frac{\nu}{E} & \frac{1}{E} & 0 & 0 & 0 \\ 0 & 0 & 0 & \frac{1}{2G} & 0 & 0 \\ 0 & 0 & 0 & 0 & \frac{1}{2G} & 0 \\ 0 & 0 & 0 & 0 & 0 & \frac{1}{2G} \end{bmatrix} \begin{bmatrix} \sigma_{11} \\ \sigma_{22} \\ \sigma_{33} \\ \sigma_{23} \\ \sigma_{31} \\ \sigma_{12} \end{bmatrix} \tag{4.12}$$

where the stress and elastic strain tensors are denoted by σ_{ij} and ϵ_{ij}, respectively. The compliance matrix in Equation (4.12) contains three independent material constants: the Young's modulus E, the Poisson ratio ν, and the shear modulus G. Using this elastic stress-strain relationship, the orientation dependence in the elastic range can be modeled by transforming Equation (4.12) into any other orientation. The thermal strain in Equation (4.11) can be written as:

$$\epsilon_{ij}^{\theta} = \alpha_{ij}\Delta T \tag{4.13}$$

where α_{ij} are the thermal expansion coefficients and ΔT is the temperature difference from the reference temperature. Because the current model is developed for isothermal conditions, the thermal strain is not evaluated.

The orientation dependence in the inelastic region and the different hardening characteristics are then modeled using the local inelastic flow equations. From the deformation mechanisms described earlier, three separate flow equations are required to characterize the inelastic response, that is:

$$\dot{\epsilon}^{I}_{ij} = (\dot{\epsilon}^{I}_{ij})_{OCT^1} + (\dot{\epsilon}^{I}_{ij})_{OCT^2} + (\dot{\epsilon}^{I}_{ij})_{CUBE} , \qquad (4.14)$$

where $(\dot{\epsilon}^{I}_{ij})_{OCT^1}$ and $(\dot{\epsilon}^{I}_{ij})_{OCT^2}$ represent the inelastic strain rates resulting from octahedral slips on the {111} planes and in the <110> and <112> directions, respectively. And $(\dot{\epsilon}^{I}_{ij})_{CUBE}$ represents the inelastic strain rates resulting from cube slip systems.

Based on experimental evidence, high strain rate behavior, such as tensile and fatigue, is modeled by using slip systems in the <110> directions on the octahedral and cube planes, corresponding OCT¹ and CUBE terms. The low strain rate behavior, creep and associated crystal lattice rotation are primarily modeled in the second term, OCT², corresponding to octahedral slip in <112> directions.

The total inelastic strain rate is calculated by summing the contributions from each of the crystallographic slip systems using Equation (4.6). The inelastic strain is obtained by integrating the total inelastic strain rate with time. Formulation of the local inelastic flow equations for each of the three slip systems is introduced next.

4.2.1 Octahedral Slip of a/2<110>{111} Type

4.2.1.1 Flow Equation

Based on the work of Ramaswamy on Rene 80, a polycrystalline nickel-base superalloy with essentially the same chemical composition as Rene N4, the octahedral flow equation for the inelastic shear strain rate, $\dot{\gamma}^{\alpha\beta}_{OCT1}$, in the α octahedral plane and β direction is assumed to have similar exponential form with both drag and back stress; that is:

$$\dot{\gamma}^{\alpha\beta}_{OCT1} = D_1 \exp\left[-A_1\left(\frac{Z_1^{\alpha\beta}}{|\tau^{\alpha\beta} - \Omega_1^{\alpha\beta}|}\right)^{n_{11}}\right] \frac{\tau^{\alpha\beta} - \Omega_1^{\alpha\beta}}{|\tau^{\alpha\beta} - \Omega_1^{\alpha\beta}|} \tag{4.15}$$

where $Z_1^{\alpha\beta}$ is the drag stress state variable to characterize the mobile dislocation resistance to motion due to obstacles, and $\Omega_1^{\alpha\beta}$ is the back stress state variable used to describe the dislocation interaction and/or rearrangement. The difference between the resolved shear stress $\tau^{\alpha\beta}$ and the back stress, $\Omega_1^{\alpha\beta}$, serves as the driving force for the inelastic flow. The direction of the local slip rate, $\dot{\gamma}^{\alpha\beta}_{OCT1}$, is then dependent on the sign of $\tau^{\alpha\beta} - \Omega_1^{\alpha\beta}$, i.e., the net effect of the shear stress and back stress. Constants D_1 and A_1 are scale factors and n_{11} is the strain rate sensitivity exponent.

Drag stress in Equation (4.15) is used to capture the long term cyclic hardening whereas the back stress is for the short time strain hardening and recovery in the monotonic tensile tests. This is distinctly different from the model proposed by Dame and Stouffer (1985) where a single drag stress was used to account for both the strain and cyclic hardening mechanisms.

4.2.1.2 Back Stress Evolution Equation

Formulation of back stress varies among different investigators. Ramaswamy and Stouffer (1988) suggested elastic and inelastic components; that is:

$$\dot{\Omega}^{\alpha\beta} = (\dot{\Omega}^{\alpha\beta})^{E} + (\dot{\Omega}^{\alpha\beta})^{I} \tag{4.16}$$

The elastic back stress rate in the current model is assumed to be power-law proportional to the resolved shear stress rate; that is:

$$(\dot{\Omega}_1^{\alpha\beta})^{E} = G_1\left(\frac{|\tau^{\alpha\beta}|}{\tau_o}\right)^{n_{12}} \dot{\tau}^{\alpha\beta} \tag{4.17}$$

where G_1 and n_{12} are material constants. Parameter τ_o is a scalar factor of the dimension in stress unit. The inelastic component, similar to Walker's and Ramaswamy's models, is given by:

$$(\dot{\Omega}_1^{\alpha\beta})^{I} = F_1|\dot{\gamma}^{\alpha\beta}|^{n_{13}}\left[\ \mathrm{sign}(\dot{\gamma}^{\alpha\beta}) - \frac{\Omega_1^{\alpha\beta}}{\Omega_{SAT^1}}\ \right] \tag{4.18}$$

except for an exponent n_{13} which is added for more generality. Combining Equations (4.17) and (4.18) gives the desired back stress evolution equation:

$$(\dot{\Omega}_1^{\alpha\beta}) = F_1|\dot{\gamma}^{\alpha\beta}|^{n_{13}}\left[\mathrm{sign}(\dot{\gamma}^{\alpha\beta}) - \frac{\Omega_1^{\alpha\beta}}{\Omega_{SAT^1}}\right] + G_1\left(\frac{|\tau^{\alpha\beta}|}{\tau_o}\right)^{n_{12}} \dot{\tau}^{\alpha\beta} \tag{4.19}$$

where n_{12}, n_{13}, F_1, G_1, and Ω_{SAT^1} are material constants. The saturated back stress at high strain rate loading condition is denoted as Ω_{SAT^1}. Current formulation uses the quantity $\dot{\gamma}^{\alpha\beta}$ as the principal measure of back stress growth. However, it may be possible to use the local inelastic work rate as the measure (i.e., $(\dot{W}^{I})^{\alpha\beta} = \tau^{\alpha\beta}\dot{\gamma}^{\alpha\beta}$). Both $\dot{\gamma}^{\alpha\beta}$

and $\dot{\tau}^{\alpha\beta}$ terms are used for modeling strain hardening behavior during high strain rate tests.

Anelasticity or dynamic recovery effect is primarily controlled by $G_1\left(\frac{|\tau^{\alpha\beta}|}{\tau_o}\right)^{n_{12}} \dot{\tau}^{\alpha\beta}$ term. If the elastic component G_1 has a larger value, the changes in back stress during loading and unloading will be significant. Thus, for the double tensile test described in Section 2.5, Chapter II, back stress decreased significantly during a unloading and result in a smaller remaining back stress in the beginning of the 120-second hold period. This smaller back stress might not be able to produce meaningful negative inelastic strain rates during the hold period. However, if the material has a less sensitive elastic component (e.g., smaller G_1) the negative inelastic strain rate may be significant during the hold period because of larger remaining back stress in the beginning of the hold period.

Other sources, such as the magnitude of Ω_{SAT1}, would also affect the anelastic behavior. Also note that the back stress in the current model has a scalar form rather than the tensorial back stress in the Walker and Ramaswamy models. This occurs because local slip is unidirectional. Dynamic thermal recovery is also included through the $[\mathrm{sign}(\dot{\gamma}^{\alpha\beta})-\Omega_1^{\alpha\beta}/\Omega_{SAT1}]$ term. Static thermal recovery is not included in the current model at this time.

4.2.1.3 Drag Stress Evolution Equation

The variables $Z_1^{\alpha\beta}$ include work or strain hardening which arises from the development of a dislocation microstructure and include the tension/ compression asymmetry. The drag stress, $Z_1^{\alpha\beta}$, has a form similar to Dame and Stouffer's model, which is given by:

$$Z_1^{\alpha\beta} = H_1^{\alpha\beta} + V_1 \ \tau_1^{\alpha\beta} + V_2 \ |\tau_2^{\alpha\beta}| + V_3 \ \tau_3^{\alpha\beta} \qquad (4.20)$$

where the parameter $H_1^{\alpha\beta}$ is a measure of work hardening and $\tau_1^{\alpha\beta}$and $\tau_2^{\alpha\beta}$ are the shear stress components associated with the core width effect and the cross slip mechanism suggested by Lall et al. (1978). This mechanism, as illustrated in Figure 4-3, was used to explain the tension /compression asymmetry in many $L1_2$ single crystal alloys (Ezz et al., 1982; Umakoshi at al, 1984; Heredia and Pope, 1986; Miner et al., 1986a). The shear stress $\tau_1^{\alpha\beta}$ is on the same octahedral plane and is perpendicular to $\tau^{\alpha\beta}$. The shear stress $\tau_2^{\alpha\beta}$ is the resolved shear stress on the cube plane in the same direction as $\tau^{\alpha\beta}$ and contributes to cross slip. The direction of $\tau_1^{\alpha\beta}$ controls the constriction or expansion of the two Shockly partial dislocations (λ_1 and λ_2 in Figure 4-3) and the ability of the dislocation to cross-slip to the cube plane. Thus, the tension/compression asymmetry is caused by the magnitude and sign of $\tau_1^{\alpha\beta}$. But the contribution from thermally-aided cross-slip because of $\tau_2^{\alpha\beta}$ is not dependent on the sign. Therefore, the absolute value of $\tau_2^{\alpha\beta}$ is used in the equation.

Lall, Chin, and Pope's model was later modified by Paidar, Pope and Vitek (1984) to include the resolved shear stress, $\tau_3^{\alpha\beta}$, in the $[\bar{1}01]$ direction on the secondary slip plane, $(\bar{1}11)$. A listing of the

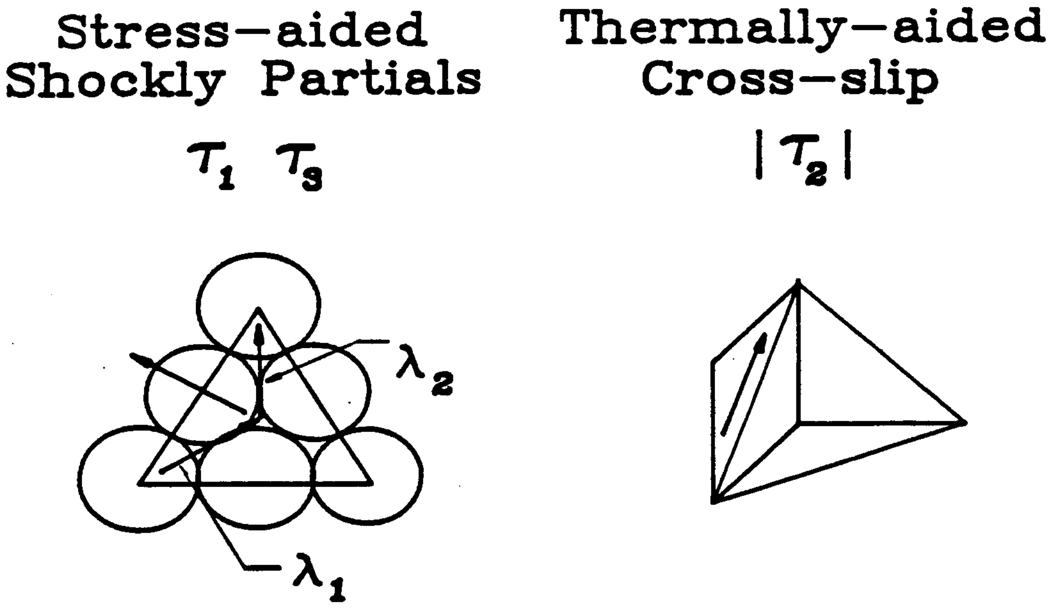
Stress–aided
Shockly Partials
τ_1 τ_3
Thermally–aided
Cross–slip
$|\tau_2|$
λ_2
λ_1

Figure 4-3 Lall, Chin, And Pope's Model (1979) For Tension/ Compression Asymmetry

Table 4-1 Corresponding Slip System Number For Resolved Shear Stresses, τ_1, τ_2, And τ_3 In Equation (4,19).

	RESOLVED SHEAR STRESS		
τ	τ_1	τ_2	τ_3
1*	13	28	16
2	14	26	20
3	15	30	24
4	16	28	13
5	17	29	19
6	18	25	22
7	19	29	17
8	20	26	14
9	21	27	23
10	22	25	18
11	23	27	21
12	24	30	15

* Slip system number.

corresponding slip system number for τ_1, τ_2 and τ_3 is given in Table 4-2. Paider at al. (1984) found that $\tau_3^{\alpha\beta}$ has a similar effect as $\tau_1^{\alpha\beta}$, which also affects the anomalous yield behavior in $L1_2$ alloys. Thus, $\tau_3^{\alpha\beta}$ is included in the proposed equation. The parameters V_1, V_2 and V_3 are then used to establish the tension/compression asymmetry. Note that the current model uses the shear stress to account for the asymmetry in yielding and the orientation dependence on the ultimate tensile strength. This will later be discussed in Section 4.3.1, Chapter V.

The increase in flow resistance caused by cyclic hardening, $H_1^{\alpha\beta}$, is governed by the evolution equation:

$$\dot{H}_1^{\alpha\beta} = m_{11}(H_{12} - H_1^{\alpha\beta})\tau^{\alpha\beta}\dot{\gamma}^{\alpha\beta} \tag{4.21}$$

By replacing $\tau^{\alpha\beta}\dot{\gamma}^{\alpha\beta}$ with $(\dot{W}^I)^{\alpha\beta}$, the local inelastic work rate, and rearranging, Equation (4.21) can be rewritten as:

$$\dot{H}_1^{\alpha\beta}/(H_{12} - H_1^{\alpha\beta}) = m_{11}(\dot{W}^I)^{\alpha\beta} \tag{4.22}$$

The integration of Equation (4.22) gives:

$$H_1^{\alpha\beta} = H_{12} + (H_{11} - H_{12}) \exp(-m_{11}W^{I\alpha\beta}) \tag{4.23}$$

Quantities H_{11} and H_{12} are the initial and saturated values of $H_1^{\alpha\beta}$, respectively. The cyclic hardening or softening is modeled by the increase or decrease of $H_1^{\alpha\beta}$ depending upon the values of H_{11} and H_{12}. The accumulated inelastic work, denoted by $W^{I\alpha\beta}$, is used as the measure of cyclic hardening. The parameter m_{11} is the exponent associated with $W^{I\alpha\beta}$ to model the rate of cyclic hardening or softening.

Equations (4.21) and (4.23) are similar to the drag stress equations in Ramaswamy's model, except that the tension/compression asymmetry terms in Equation (4.20) are added to the current model. The static thermal recovery term is not included in the current model, and its significance has been questioned in other models (Ramaswamy, 1985; Krempl et al., 1986; Sherwood, 1986).

4.2.2 Cube Slip of a/2<110>{100} Type

Cube slip systems are active for high strain rate loading near the [111] orientation. Mixed cube slip and octahedral slip systems were operative during tensile tests in the orientations away from the [111]. Thus, parallel to the octahedral slip equations, cube slip equations are developed similarly to account for the cube slip characteristics.

4.2.2.1 Flow Equation

Similar to Equation (4.15), the flow equation for the inelastic shear strain rate on the α cube plane in the β direction is given by

$$\dot{\gamma}^{\alpha\beta}_{\mathrm{CUBE}} = D_s \exp\left[-A_s\left(\frac{Z_s^{\alpha\beta}}{|\tau^{\alpha\beta} - \Omega_s^{\alpha\beta}|}\right)^{n_{s1}}\right] \frac{\tau^{\alpha\beta} - \Omega_s^{\alpha\beta}}{|\tau^{\alpha\beta} - \Omega_s^{\alpha\beta}|} \qquad (4.24)$$

where $Z_s^{\alpha\beta}$ and $\Omega_s^{\alpha\beta}$ are the drag stress and back stress state variables for the cube slip, respectively. Constants D_s and A_s are scaling factors and n_{s1} is the strain rate sensitivity exponent for the cube slips.

4.2.2.2 Back Stress Evolution Equation

The back stress evolution equation for cube slip is also similar to the octahedral slip a/2<110>{111} and has the form:

$$(\dot{\Omega}_3^{\alpha\beta}) = F_3|\dot{\gamma}^{\alpha\beta}|^{n_{33}}[\mathrm{sign}(\dot{\gamma}^{\alpha\beta}) - \frac{\Omega_3^{\alpha\beta}}{\Omega_{SAT3}}] + G_3(\frac{|\tau^{\alpha\beta}|}{\tau_o})^{n_{32}}\dot{\tau}^{\alpha\beta} \quad (4.25)$$

where n_{32}, n_{33}, F_3 and G_3 are material constants. The saturated back stress for the cube slip is denoted as Ω_{SAT3}, which is also a material parameter.

4.2.2.3 Drag Stress Evolution Equation

The drag stress evolution equation for cube slip is similar to Equation (4.20) but it lacks the tension/compression dependence terms (i.e., τ_1, τ_2 and τ_3 terms) because tension/compression asymmetry is insignificant in cube slip. Therefore, the formulation is similar to Schmid's law. The drag stress evolution equation for cube slip system in integrated form is given by:

$$Z_3^{\alpha\beta} = H_{32} + (H_{31} - H_{32})\exp(-m_{31}W^{I\alpha\beta}) \quad (4.26)$$

where H_{31}, H_{32} and m_{31} are determined from the fatigue response of the cube slip system. The static thermal recovery is also neglected.

4.2.3 Octahedral Slip of a/2<112>{111} Type

Octahedral a/2<112>{111} slip systems are active for low strain rate loading conditions (i.e., creep). As mentioned earlier, the back stress was found to be a function of the creep stress.

4.2.3.1 Flow Equation

Similar to equation (4.15), the flow equation for inelastic shear strain rate, $\dot{\gamma}_{OCT2}^{\alpha\beta}$, in α octahedral slip plane in β direction is given by:

$$\dot{\gamma}^{\alpha\beta}_{OCT^2} = D_2\exp[-A_2(\frac{Z_2^{\alpha\beta}}{|\tau^{\alpha\beta} - \Omega_2^{\alpha\beta}|})^{n_{21}}]\frac{\tau^{\alpha\beta} - \Omega_2^{\alpha\beta}}{|\tau^{\alpha\beta} - \Omega_2^{\alpha\beta}|} \quad (4.27)$$

where $Z_2^{\alpha\beta}$ and $\Omega_2^{\alpha\beta}$ are the drag stress and back stress state variables for the octahedral a/2<112>{111} slip systems, respectively. Constants D_2 and A_2 are scaling factors and n_{21} is the strain rate sensitivity exponent for the a/2<112>{111} slip.

4.2.3.2 Back Stress Evolution Equation:

The back stress evolution equation is then

$$(\dot{\Omega}_2^{\alpha\beta}) = F_2|\dot{\Phi}^{\alpha\beta}|^{n_{23}}[\mathrm{sign}(\dot{\gamma}^{\alpha\beta}) - \frac{\Omega_2^{\alpha\beta}}{\Omega^{\alpha\beta}_{SAT^2}}] + G_2(\frac{|\tau^{\alpha\beta}|}{\tau_o})^{n_{22}}\dot{\tau}^{\alpha\beta} \quad (4.28)$$

where n_{22}, n_{23}, F_3 and G_3 are material constants. The saturated back stress $\Omega^{\alpha\beta}_{SAT^2}$, different from Ω_{SAT^1} and Ω_{SAT^3}, is a function of the resolved shear stress $\tau^{\alpha\beta}$; that is:

$$\Omega^{\alpha\beta}_{SAT^2} = C_0\tau^{\alpha\beta} + C_1 \quad (4.29)$$

where C_0 and C_1 are material constants. The proposed linear relationship between saturated back stress and resolved shear stress is similar to the linear relationship between saturated back stress and applied stress observed for polycrystalline nickel-base superalloys Rene 80 (Ramaswamy, 1985) and Rene 95 (Sherwood, 1986).

4.2.3.3 Drag Stress Evolution Equation:

The drag stress evolution equation for octhedral a/2[112](111) slip should have a form similar to Equation (4.26). The accumulated inelastic work during a creep test is relatively small. Thus, it is assumed the hardening term is unchanged during creep. The influence of lattice rotation on the drag stress is assumed to be present. Hence, the drag stress evolution equation for octahedral a/2<112>{111} slip systems has the form:

$$Z_2^{\alpha\beta} = H_{21} + H_2^* \quad , \tag{4.30}$$

where H_{21} is a material parameter. The influence on drag stress caused by crystal lattice rotation is denoted by H_2^* . This term will be discussed in the next section.

4.3 Crystal Lattice Rotation

Crystal lattice rotation reported in the literature for uniaxial loading only occurs for octahedral a/2<112>{111} slip system during creep conditions. Several assumptions made in the development of this model should be noted before introducing the equations:

- The current model is based on the assumption that the crystal lattice rotation only operates under single glide. That is, the rotation terminates when a duplex slip boundary is reached. For example, specimens with the orientation in region I (as shown in Figure 3-3) will rotate toward [001]-Y boundary under single glide of $[1\bar{1}2]$ slip system. Based on the assumption, the rotation will terminate when the tensile axis reaches the [001]-Y boundary to activate duplex slip (which corresponds to the begining of secondary creep).
- The rate of lattice rotation is assumed to be a function of the local inelastic shear strain rate or inelastic work rate. For example, Figure 4-4 shows the creep curves for five MAR-M247 samples. The creep strain is treated as the combination of both

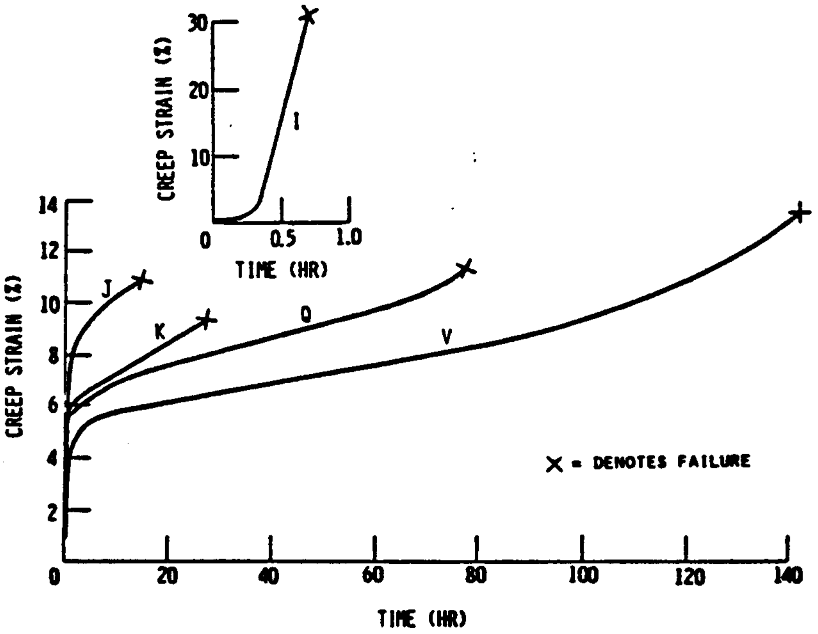

SPECIMEN	PRIMARY CREEP STRAIN, Pct	ORIENTATION, DEGREES FROM [001]	[011]
I	34.7	43.0	6.5
J	5.9	8.0	39.5
K	5.5	9.5	36.0
Q	3.7	5.5	41.0
V	2.2	2.0	43.0

Figure 4-4 Creep Curves Of Selected MAR-M247 Specimens Tested At 774°C and 724MPa.

inelastic strain and the lattice rotation. Because the overall creep strain rates are gradually decreasing for both rotated (smaple J, for example) and non-rotated (sample V) samples. Thus the contribution from lattice rotation to the total creep rate must follow the same decreasing trend. Also, because lattice rotation only occurs at low strain rate, it is assumed that a relationship between creep strain rates and the lattice rotation rates is present.

- The lattice rotation is assumed to increase the drag stress (i.e., measure of material hardening). It has frequently been reported that γ' precipitates link together during creep to form platelets, or rafts, perpendicular to the applied stress axis. This directional coarsening of γ' begins during primary creep and continues to develop well after the onset of secondary creep. The thickness of the raft, however, remaines constant through the onset of tertiary creep (Fredholm and Strudel, 1984; MacKay and Ebert, 1984). It is hypothesized that the rate of alignment of the rafts with the tensile axis affects the microstructure resistance to the external loads. Thus, the lattice rotation is assumed to affect the drag stress and this effect is controled by H^* in Equation (4.30).

In Equation (4.10), the rate of spin tensor $\dot{\omega}_{ij}$ represents the rate of crystal lattice rotation from the tensile axis toward the primary slip direction with respect to the material principal coordinates. The skew-symmetric spin tensor has the following form:

$$\omega_{ij} = \begin{bmatrix} 0 & \omega_{12} & \omega_{13} \\ -\omega_{12} & 0 & \omega_{23} \\ -\omega_{13} & -\omega_{23} & 0 \end{bmatrix} \tag{4.32}$$

where ω_{12}, ω_{13} and ω_{23} represent the lattice rotation about the material principal axes z, y and x, respectively. For any skew-symmetric tensor such as ω_{ij}, a dual vector, $\underset{\sim}{t}^R$ can be found as:

$$\underset{\sim}{t}^R = -(\,\omega_{23}\hat{i} + \omega_{31}\hat{j} + \omega_{12}\hat{k}) \tag{4.33}$$

to represent the rotation vector. Equation (4.33) can be further expressed as:

$$\underset{\sim}{t}^R = \sin\theta \;\; \underset{\sim}{n}^R \tag{4.34}$$

where $\underset{\sim}{n}^R$ is a unit vector in the direction along the axis of rotation and θ is the right-hand rotation angle (Lai et al., 1978).

For lattice rotation caused by single slip under uniaxial loading, the amount of stretch due to lattice rotation can be calculated by using the stack-of-coins model (illustrated in Figure 4-5). The interpretation of the calculated result is shown in Figure 4-6 in which the stereographic triangle is plotted in 3-D space. For region I single slip (refer to Figure 3-3), a local coordinate system in Figure 4-5 is defined by three axes: the tensile axis $\underset{\sim}{s}$, which is also the current crystal orientation [hkℓ]; the axis of rotation $\underset{\sim}{t}^R$; and axis $\underset{\sim}{X}$ (i.e., $\underset{\sim}{X} = \underset{\sim}{t}^R \times \underset{\sim}{s}$). Axes $\underset{\sim}{s}$ and $\underset{\sim}{t}^R$ are also plotted in Figure 4-6. For constant projected atomic distance t, the projected distance between two adjacent atomic layers at the initial configuration is:

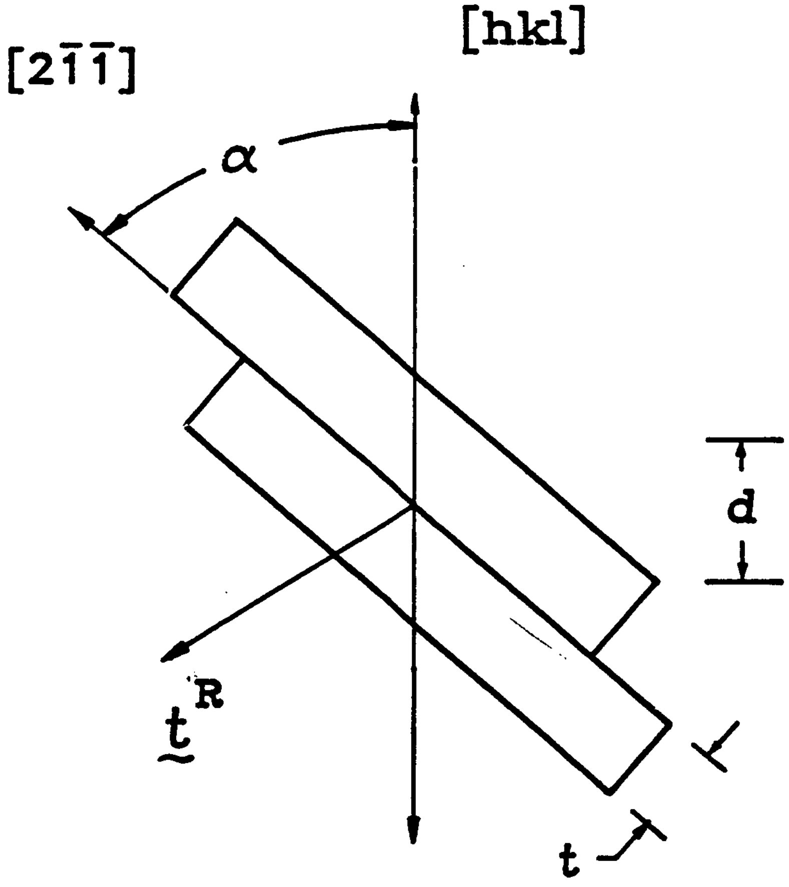
[hkl]
[2$\bar{1}\bar{1}$]
α
d
$\underset{\sim}{t}^{R}$
t

Figure 4-5 Stack-Of-Coins Model

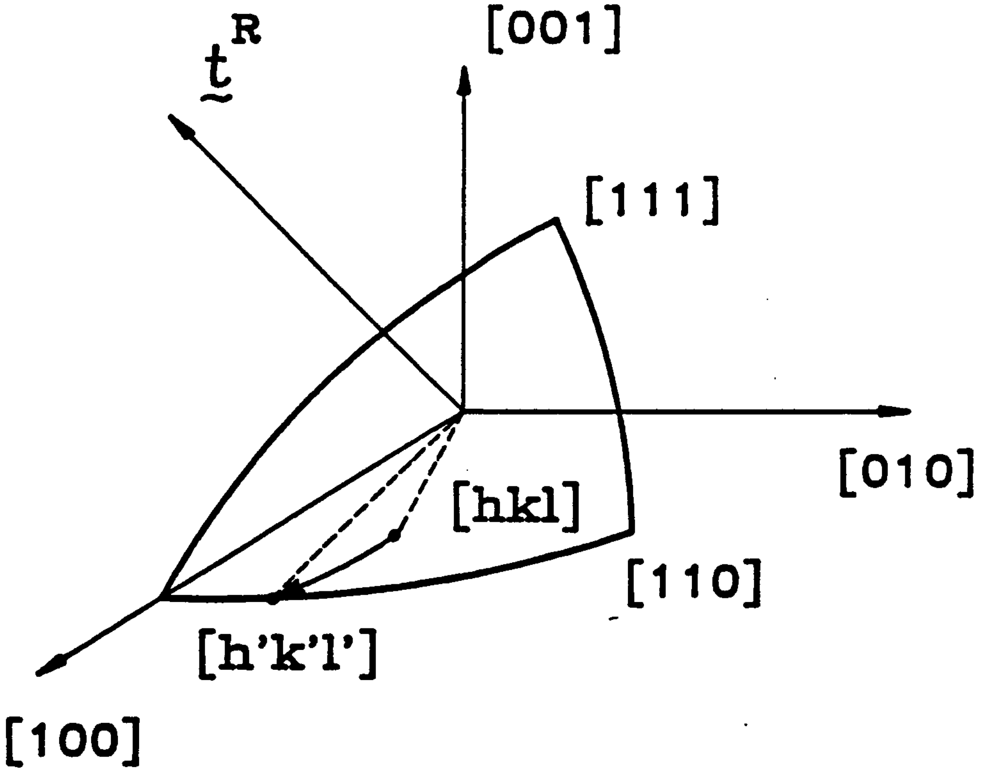
$\underset{\sim}{t}^R$
[001]
[111]
[010]
[hkl]
[110]
[h'k'l']
[100]

Figure 4-6 Interpretation Of The Stack-Of-Coins Model Using Stereographic Triangle Plotted In The 3-D Space.

$$d_0 = \frac{t}{\sin\alpha_0} \tag{4.35}$$

After rotation, this quantity becomes

$$d_1 = \frac{t}{\sin\alpha_1} \tag{4.36}$$

When using the local coordinate system, the stretch ratio caused by rotation from α_0 to α_1 can be calculated as:

$$\lambda_{11} = \frac{d_1}{d_0} = \frac{\sin\alpha_0}{\sin\alpha_1} \qquad \lambda_{33} = \frac{\cos\alpha_1}{\cos\alpha_0}$$

$$\text{and} \quad \lambda_{22} = 0 \tag{4.37}$$

Or in terms of strain:

$$\epsilon_{11} = \frac{\sin\alpha_0}{\sin\alpha_1} - 1 \quad , \quad \epsilon_{33} = \frac{\cos\alpha_1}{\cos\alpha_0} - 1$$

$$\text{and} \quad \epsilon_{22} = \epsilon_{12} = \epsilon_{23} = \epsilon_{13} = 0 \tag{4.38}$$

These quantities are then transformed back to the material principal coordinates. The rotation angle $\Delta\alpha=\alpha_1-\alpha_0$ is identical to the rotation angle θ defined in Equation (4.34).

As stated in the beginning of this section, the current model assumes that the rate of lattice rotation is a function of the total inelastic work rate and is proposed to have the power form. That is:

$$\dot{\theta} = K_1(|\ln(\dot{W}^I)|)^{m_{22}} \left(1 - \frac{\theta}{\theta_{max}}\right) \tag{4.39}$$

where K_1 and m_{22} are material parameters. The maximum amount of rotation, θ_{max} is pre-determined as the angle from initial sample orientation to the duplex boundary. The value of θ_{max} has an upper limit of 10° ,according to experimental data (MacKay and Maier, 1982).

The increases of drag stress, H_2^*, due to strain hardening by crystal lattice rotation is assumed to be linearly proportional to the amount of rotation. That is:

$$H_2^* = K_2\left(\int_0^t \dot{\theta} dt\right) \quad . \qquad (4.40)$$

4.4 Summary Of Model Development

Comparing the current model with Dame and Stouffer's model, there are several major modifications. First, a back stress state variable and the associated evolution equation were added into the current model to account for anelastic material response. Second, instead of octahedral a/2<110>{111} slip systems, octahedral a/2<112>{111} slip systems were used for modeling single crystal creep response. Because of crystal lattice rotation, a set of rotation kinematics equations were developed.

The materials presented in previous sections have two major characteristics:

- The formulation of the constitutive equation is closely associated with the observed deformation mechanisms
- The functional form of the flow equation and state variable evolution equations for the three slip systems are identical.

These characteristics should enhance the predictive capability of the model and offer a systematic way to evaluate material parameters for all three slip systems.

Experimental data were not available to further address the interrelationship between crystal lattice rotation, evolution of microstructure and the observed mechanical response. Thus on several occasions, assumptions were made to allow the estimation of the material parameters. This topic will be further discussed in the next chapter.

CHAPTER V

EXPERIMENTAL DATA AND EVALUATION OF MATERIAL CONSTANTS

Identification of material parameters is perhaps the most difficult task for the unified theory. These material constants are presumably calculatable by using experimental data. However, the evaluation procedure varies significantly among various models. A general rule for evaluating material parameters does not seem to exist. sometimes, hypothetical values are assigned to certain parameters.

In this study, a special evaluation procedure was developed. This procedure consists of four major steps. Each step corresponds to the evaluation of specific material parameters.

This chapter contains a review of the data base that was available for the research. Also described are methods for using the data in each step of the parameter evaluation procedure in order to determine the material constants for the constitutive equations.

5.1 Experimental Data for Single Crystal Alloys

Experimental data for Rene N4 came from two sources:

- Data that were used in Dame and Stouffer's model, including tensile and creep tests at 760°C for an earlier version of Rene N4 designated as VF317.
- The data at 982°C that were generated in this research for Rene N4.

The later experiments were performed in cooperation with Dr. N. Jayaraman and Mr. D. Alden at the MTS Material Testing Laboratory in the Material Science and Engineering Department, University of Cincinnati.

5.1.1 Rene N4 VF317 at 760°C

The tensile data for Rene N4 VF317 at 760°C consist of three tests on specimens at [100], [110] and [930] directions, respectively. The specimens had a Codep coated cylindrical gage section which was 18mm long by 3.3mm in diameter. The tensile tests were conducted at a constant strain rate of 8.333×10^{-5}/sec to inelastic strains of 0.2%. At 0.2% yield, the extensometers were removed and the specimens were pulled to failure at a constant head rate of 0.02117 mm/sec. The response to approximately 1% strain (as shown in Figure 5-1) displays considerable orientation dependence. The stress increased about 30% between the 0.2% yield stress and ultimate stress for all specimens.

Tensile creep rupture test data at 760°C were also available for Rene N4 VF317 in the same three orientations. These tests utilized Codep-coated specimens, of 3.175 mm in diameter. A total of seven creep tests at three orientations were conducted (the results are shown in Figure 5-2).

Two of the creep tests at 620 MPa were terminated before failure. The reduction in area ranged from 17% to 48%. Note that the specimens in the [310] orientation were stronger in both the tensile and creep tests than expected when compared to the other data or to PWA 1480 (Figure 1.2). Also, the specimens at this orientation were nearly as strong as the specimens in the [100] orientation. The reason for this anomaly is not known.

The above data set is insufficient to provide information regarding tension/compression asymmetry. Pertinent information, however, was obtained from the published data by Miner et al. (1986b) on tension/compression asymmetry of Rene N4 at 760°C. In the Miner study, the variability of the yield stress between crystals was as large as

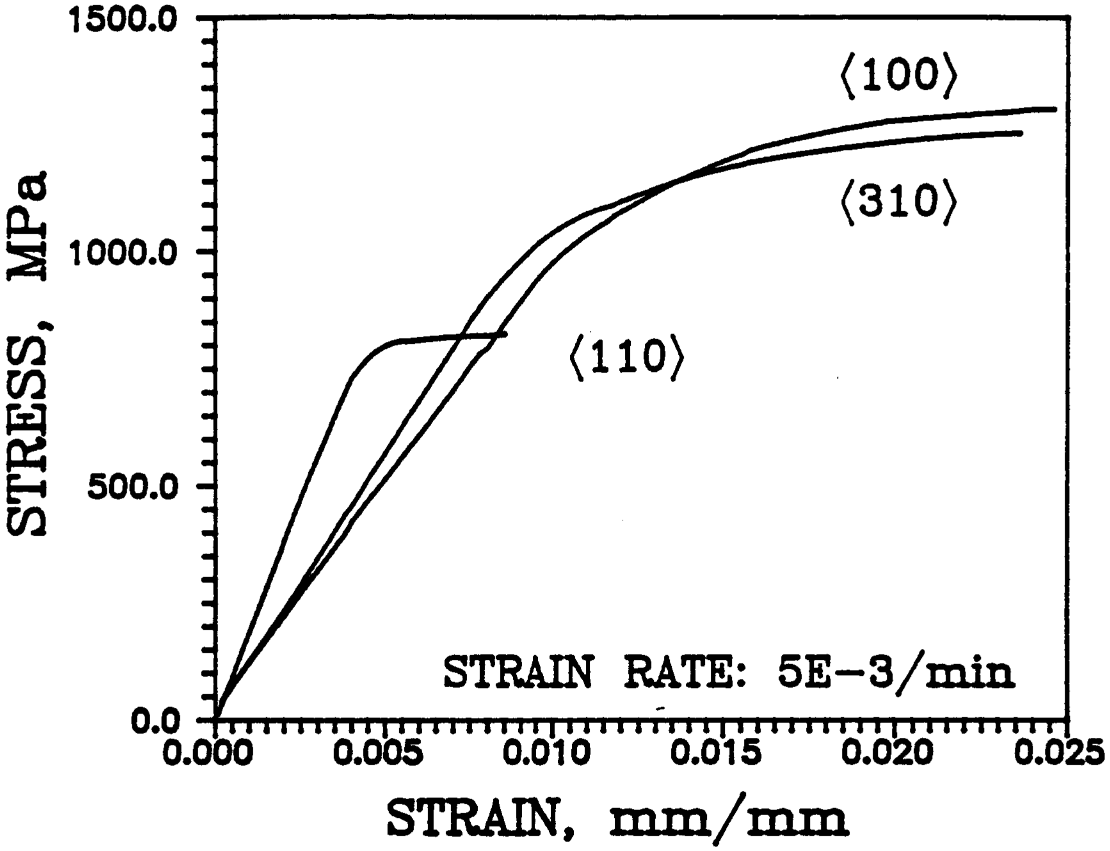

Figure 5-1 Tensile Tests Of Rene N4 VF317 At 760°C.

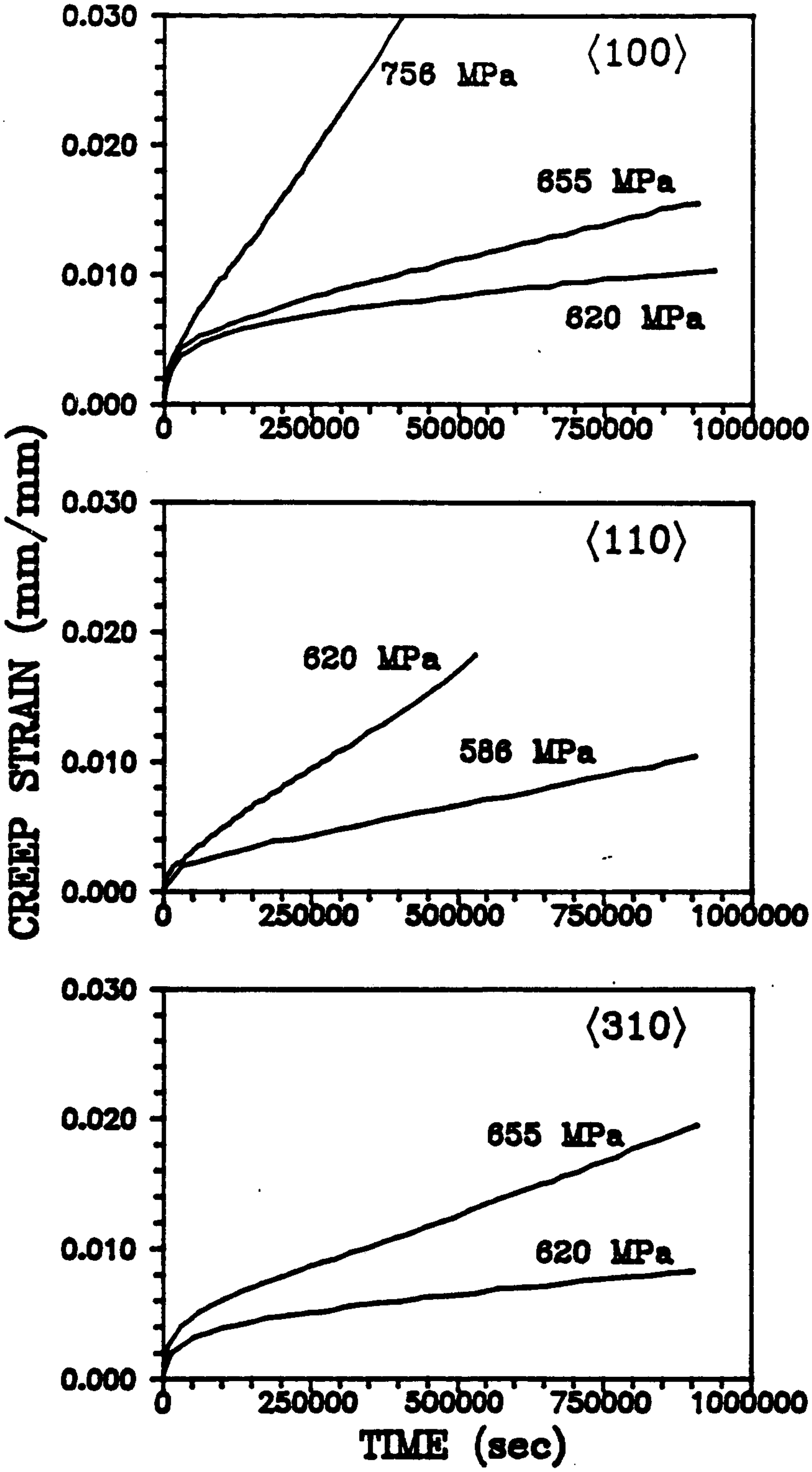

Figure 5-2 Creep Tests Of Rene N4 VF317 At 760°C.

23%. Note that the tensile responses reported by Gabb, Gayda, Minor, and Voigt (1986) for specimens oriented in the [100] direction were about 30% weaker than VF317 in tension. With this information, the VF317 data were used to develop the constants at 760°C for octahedral slip at high strain rates in tension and low stress levels in creep.

5.1.2 Rene N4 at 982°C

Early in this research an experimental program was initiated. The goal was to generate data for constitutive modeling and identification of deformation mechanisms. Test samples were purchased in the nominal orientations of [100], [110], [111], [210] and [321]. Samples were electropolished and the orientation was determined by the Laue X-ray diffraction technique.

The mechanical tests were performed on a MTS closed loop material test system with a 20,000 kip load frame. The tests were conducted under total strain control at 982°C. The control of the MTS unit and data acquisition was done by using a computer with software developed by Mr. D. Alden, University of Cincinnati.

To date, five different types of tests have been conducted on specimens in the five nominal crystal orientations. These tests are:

- Monotonic tensile test
- Double tensile test with a 120-seconds hold period at zero stress
- Fully reversed fatigue test
- Fatigue with a 30-second peak tensile strain hold time in each cycle
- Fatigue with a 30-second peak compressive hold time in each cycle

Detailed descriptions of each test are given in Table 5-1. The tensile results of Rene N4 at 982°C are shown in Figure 5-3. The material exhibited less anisotropy than that at 760°C, as shown in Figure 5-1. However, strain hardening characteristics were dramatically different for samples with different orientations. The hardening characteristics were similar for samples with the same orientation which were tested at different temperatures. In Figure 5-1, for example, specimens in [110] orientation showed almost elastic-perfect plastic behavior, whereas [100] samples had a much longer hardening period.

Fatigue loops for samples in [100], [111] and [123] directions are shown in Figures 5.4 through 5.6, respectively. These fatigue tests stabilized within 10 cycles and exhibited no cyclic hardening or softening throughout the remaining life. Tension/compression asymmetry in peak stresses was observed for sample in the [100] orientation and was insignificant for sample in the [111] orientation. The tensile and compressive strain hold tests are shown in Figures 5.7 and 5.8, respectively. The compressive strain hold fatigue test is similar to the fully reversed fatigue tests, and stabilized within the first ten cycles. The tensile strain hold test exhibited gradual softening of the material. This is believed to be caused by an increasing damage rate (or crack opening rate) of the material caused by the tensile hold.

Part of the 982°C data was used for evaluation of material constants and the rest of the data was used for model verification. Because no creep data were available at this temperature, the constants for the octahedral a/2<112>{111} slip were not evaluated.

5.1.3 Creep Data From Other Single Crystals

The creep data of Rene N4 VF317 at 760°C showed no indication of lattice rotation including the samples in the [110] orientation (see

Table 5-1 Discriptions Of Mechanical Tests For Rene N4 At 982°C.

NOMINAL [hkℓ]	ACTUAL [hkℓ]	DIAMETRAL [hkℓ]	STRAIN RATE	NOTES
TENSILE				
[321]	[-37 -28 10]	[1 -1 1]	5E-4/s	
[321]	[-27 39 10]	[1 1 1]	1E-4/s	
[110]	[46 1 35]	[0 -1 0]	1E-4/s	Pulled to 0.23%
[110]	[-9 -7 -2]	[-1 1 1]	1E-4/s	
[100]	[-26 1 1]	[0 0 1]		Double tensile*
[111]	[-14 -10 13]	[1 0 1]		Double tensile*
FATIGUE				STRAIN RANGE
[100]	[-4 -1 57]	[0 -1 0]	3E-4/s	±0.85%
[111]	[-10 11 -11]	[-1 -1 0]	3E-4/s	±0.30%
[321]	[10 33 54]	[-2 -1 1]	3E-4/s	±0.30%
[321]	[49 38 10]	-	3E-4/s	±0.30% †
[321]	[-20 -3 -7]	-	3E-4/s	±0.30% ††

* Double tesile: specimen was first loaded to 1.5% at strain rate of $1\text{x}10^{-4}$/sec, unloaded immediately to zero stress within 10 seconds, followed by 120 seconds hold period, and then reloaded at higher strain rate of $6\text{x}10^{-4}$/sec .

† A 30 seconds hold was superimposed to each cycle at peak compressive strain.

†† A 30 seconds hold was superimposed to each cycle at peak tensile strain.

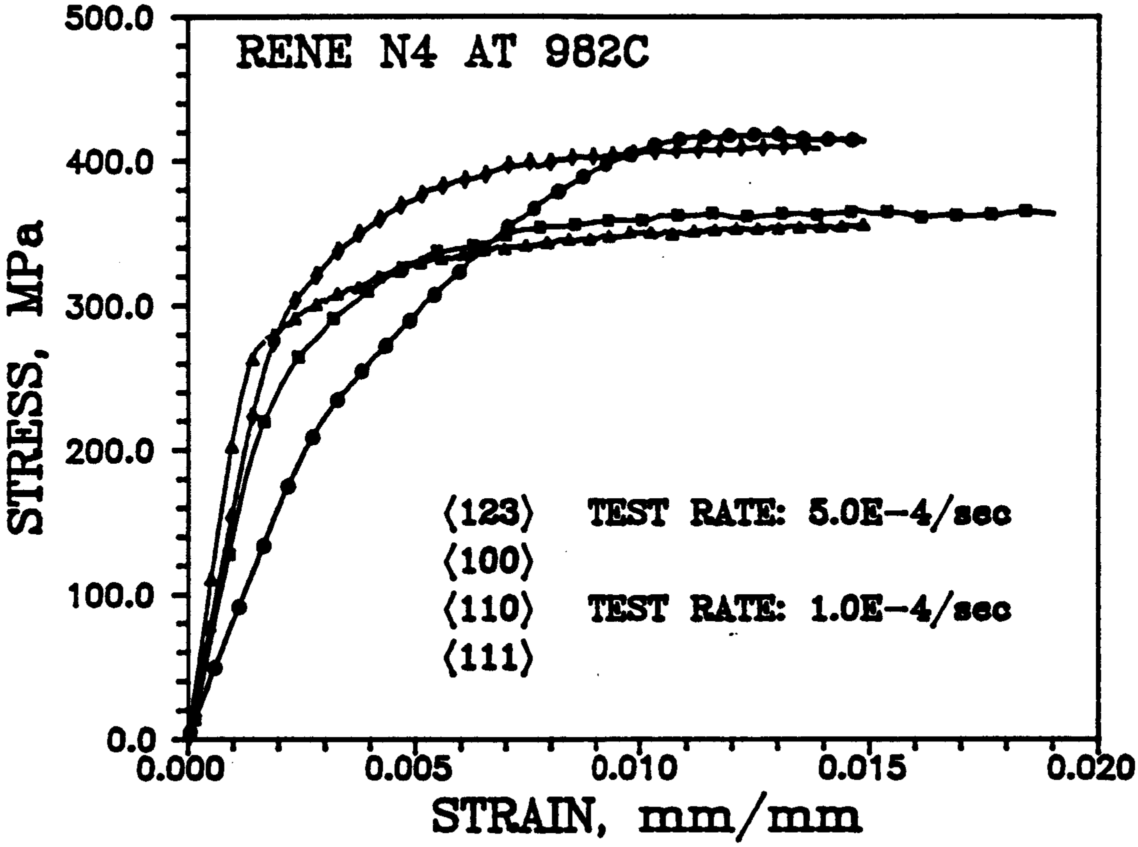

Figure 5-3 Experimental Data For Tensile Tests In The [100], [110], [111] And [321] orientations Of Rene N4 At 982°C

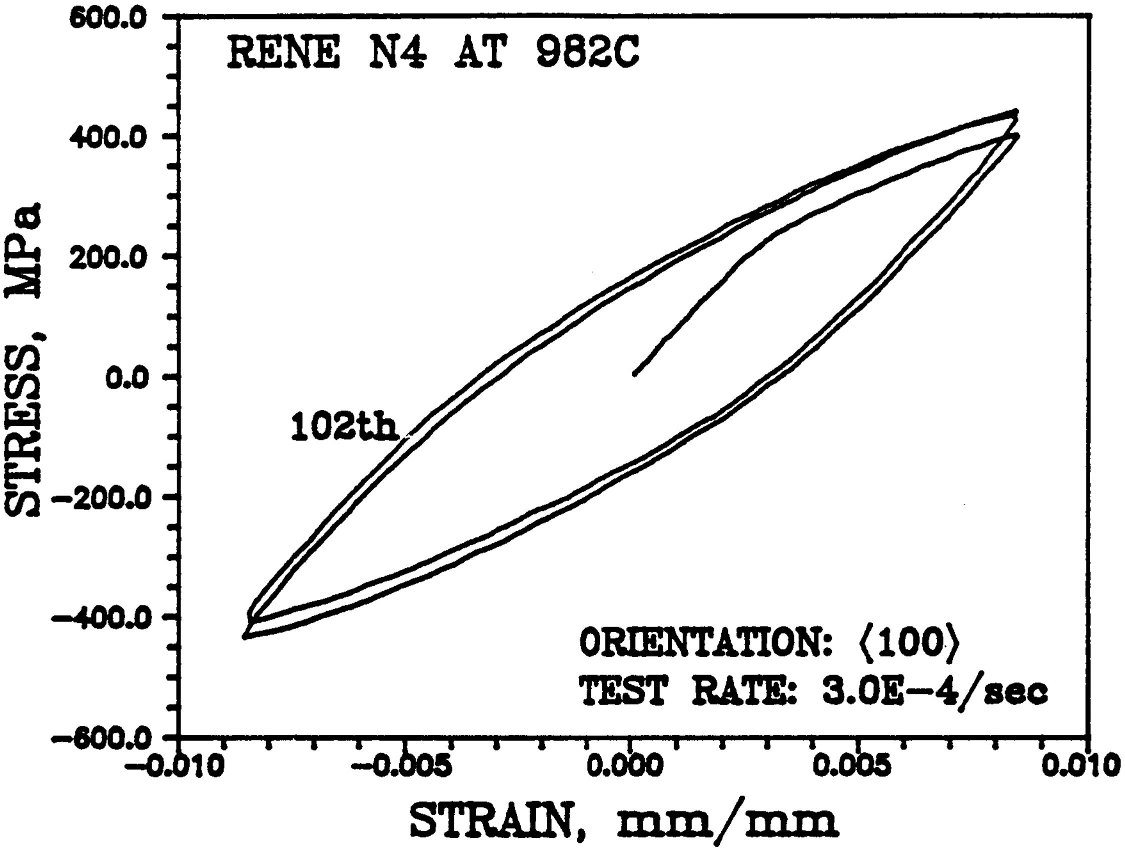

Figure 5-4 Experimental Data For Fatigue Test Of Rene N4 In The [100] Orientation At 982°C

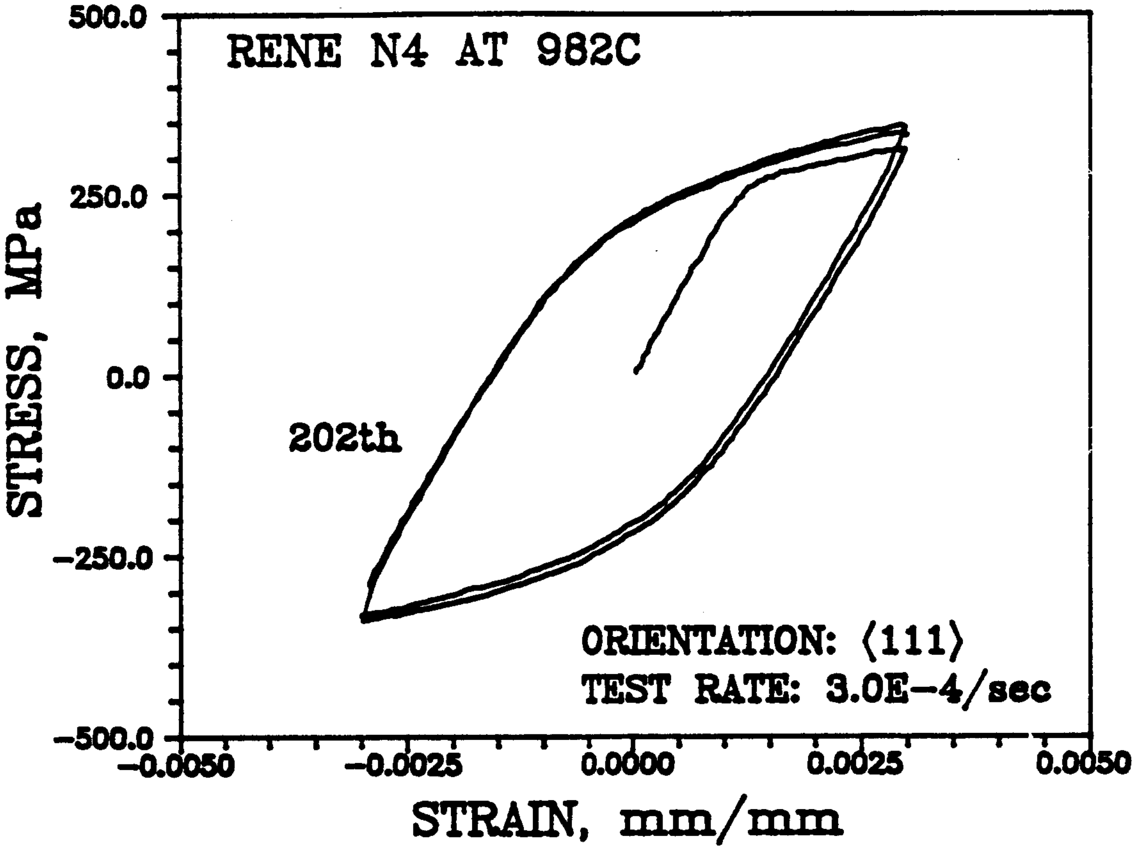

Figure 5-5 Experimental Data For Fatigue Test Of Rene N4 In The [111] Orientation At 982°C

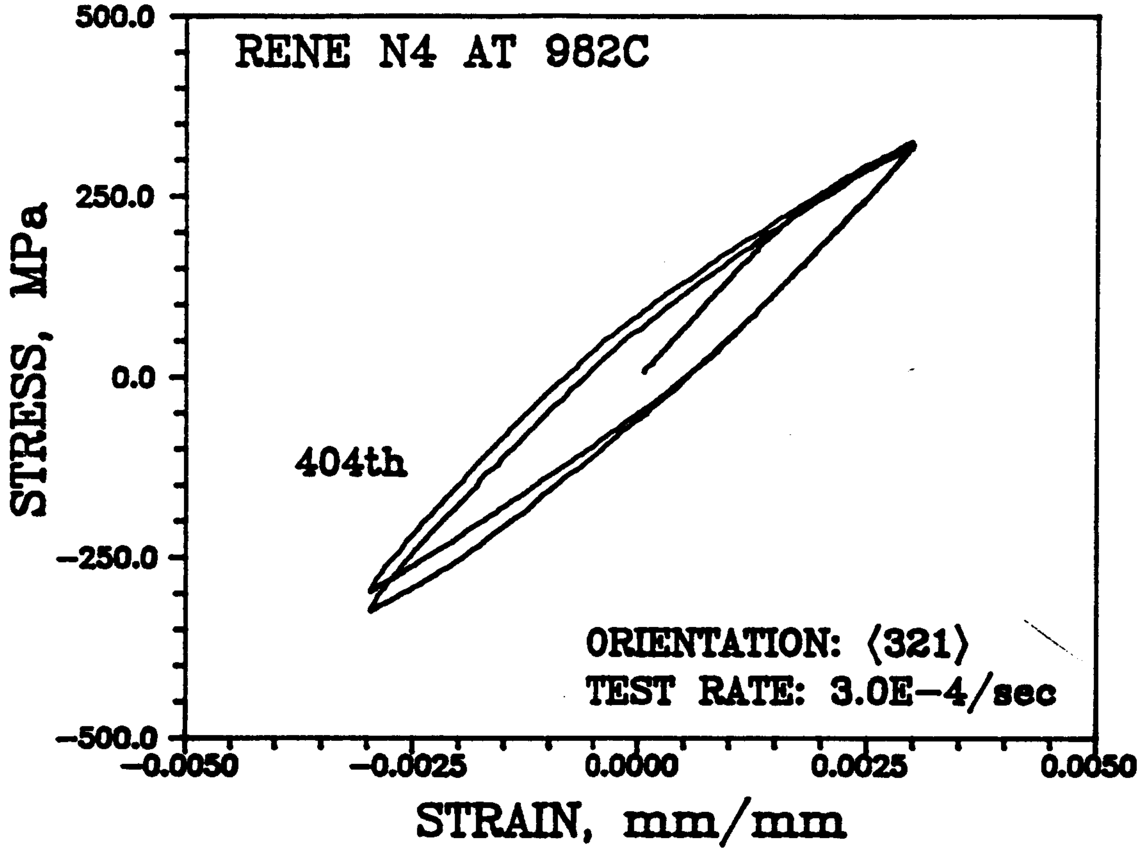

Figure 5-6 Experimental Data For Fatigue Test Of Rene N4 In The [321] Orientation At 982°C

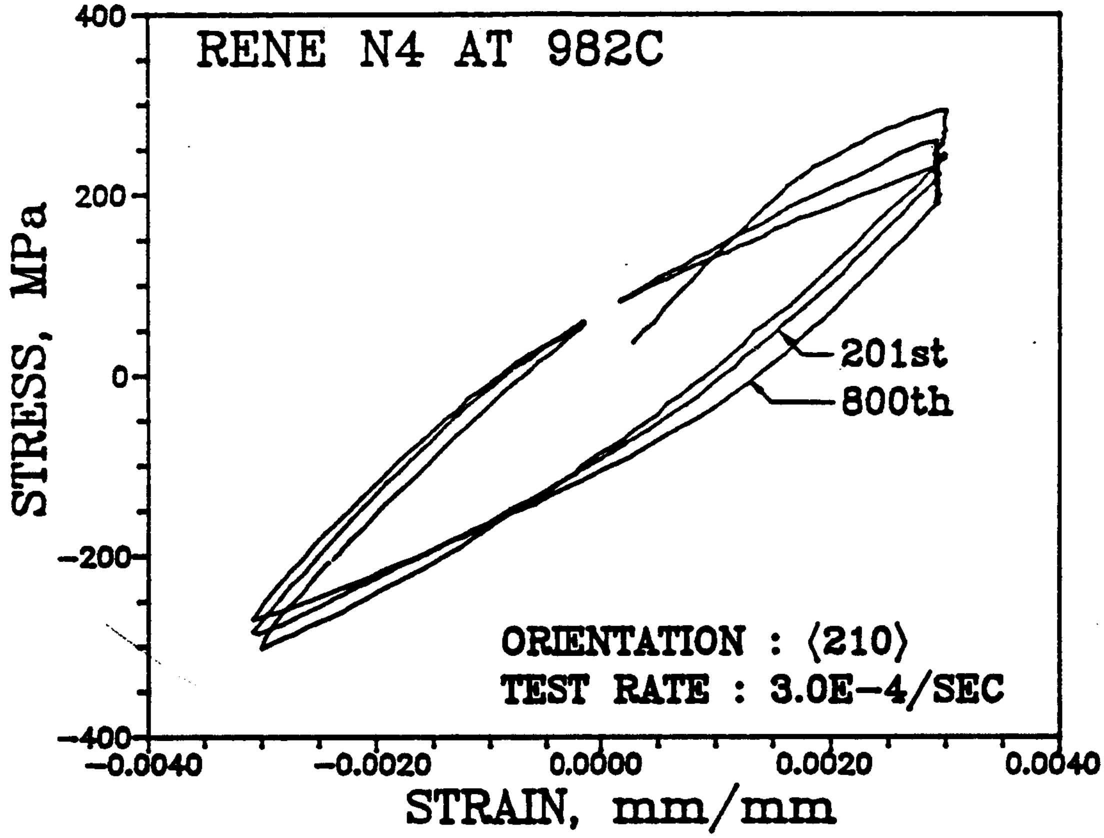

Figure 5-7 Experimental Data For Fatigue Test With A 30-Second Peak Tensile Strain Hold Of Rene N4 In The [321] Orientation At 982°C

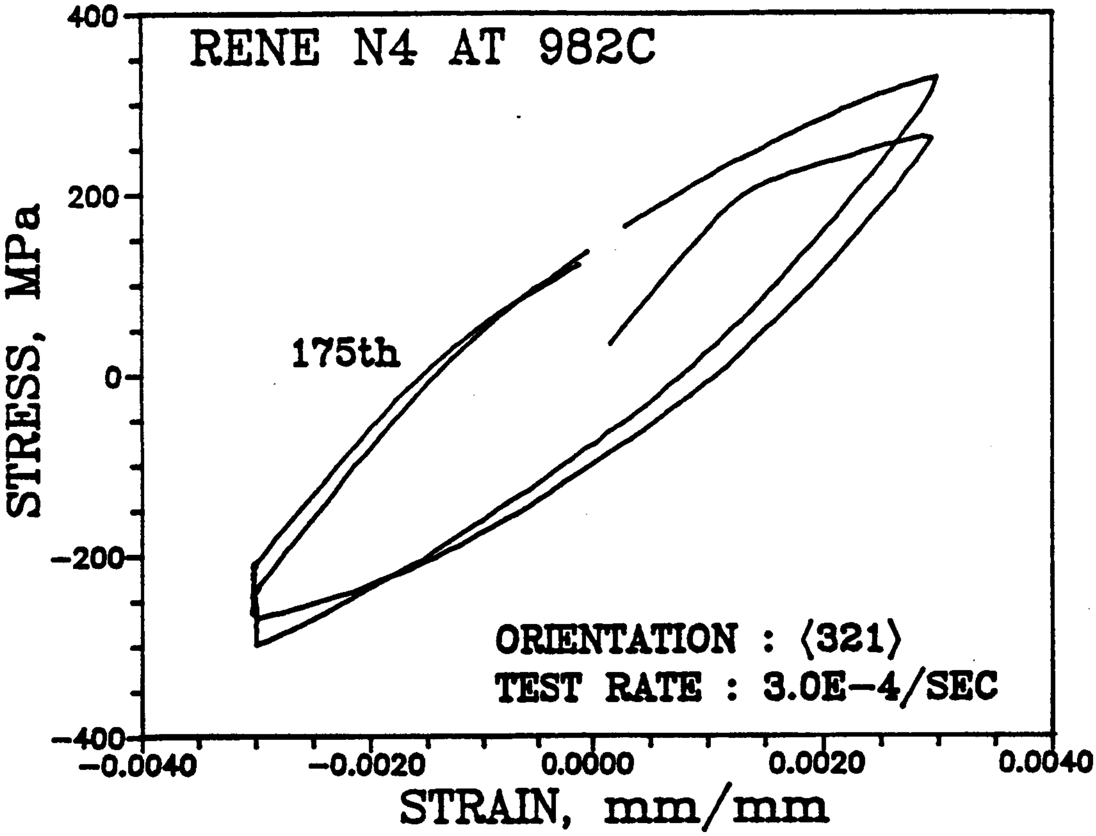

Figure 5-8 Experimental Data For Fatigue Test With A 30-Second Peak Compressive Strain Hold Of Rene N4 In The [321] Orientation At 982°C

Figure 5-2) For example, the primary creep strains and the strains at the onset of the secondary creep are much smaller than the values presented in Figure 4-4 for MAR-M247. However, note that the stress levels for Rene N4 is about 100MPa less than for MAR-M247. Through personal communication, it was found that single crystal CMSX-3 did not show lattice rotation either.

In this research, the lattice rotation calculation was made only for prediction of the trends that have been demonstrated; i.e., that large rotation is associated with large primary creep strain, large primary creep strain rate, and large secondary creep rate. Model calculations were then compared with results published by MacKay and Maier (1982) and by Leverant and Kear (1970) in Chapter VI.

5.2 Evaluation of Elastic Material Constants

Material constant derivation is divided into two categories; the elastic material constants and the material constants in the inelastic constitutive equation. The three independent elastic material constants for nickel-base single crystals are Young's modulus E, Poisson ratio ν, and shear modulus G in the principal orientation of the material. These elastic constants as shown in Equation 4.12); they are used to predict the elastic response of single crystals. Equation (4.12) can be also expressed as:

$$\epsilon_{ij} = S_{ijk\ell}\sigma_{k\ell} \tag{5.1}$$

In the material principal axis, $S_{1111} = 1/E$, $S_{1122} = -\nu/E$, and $S_{2323} = 1/4G$. For loading in the [hkℓ] direction, the associated S'_{2211} in the relationship of $\epsilon_{22} = S'_{2211}\sigma_{11}$ can be calculated by:

$$S'_{2211} = [S_{1122}A(\theta) + 2(S_{1111} - 2S_{2323})B(\theta)]/d^4(d^2-1) \qquad (5.2)$$

where $d^2 = h^2+k^2+1$ and θ is defined graphically (shown in Figure 5-9). Functions $A(\theta)$ and $B(\theta)$ in Equation (5.2) are computed as follows:

$$\begin{aligned} A(\theta) = {} & [(d^2-1)(d^4-2d^2+2) + 2h^2k^2] \sin^2\theta \\ & + d^2[d^2(d^2-1) - 2h^2k^2] \cos^2\theta \\ & + 2hkd(h^2 - k^2) \sin\theta\cos\theta \end{aligned} \qquad (5.3)$$

and

$$\begin{aligned} B(\theta) = {} & [(d^2-1) - h^2k^2] \sin^2\theta \\ & + h^2k^2d^2 \cos^2\theta \\ & - hkd(h^2 - k^2) \sin\theta\cos\theta \end{aligned} \qquad (5.4)$$

Another equation which also available for calculating S'_{1111} is

$$S'_{1111} = (1-2J)S_{1111} + 2J(S_{1122}+2S_{2323}) \qquad (5.5)$$

where

$$J = h^2k^2 + k^2\ell^2 + \ell^2h^2 \qquad (5.6)$$

Because limited data available on Rene N4 VF317 at 760°C, the elastic material constants at this temperature were not evaluated in this research. The values of E, G, and ν were taken from Dame and Stouffer's model; that is, 100.0 GPa, 96.5 GPa and 0.38 for E, G, and ν, respectively.

The experimental data for Rene N4 at 982°C were used to compute E, G, and ν; these data are listed in Table 5.2. The known values are the elastic moduli in the $[hk\ell]$ direction and Poisson's ratios in the transverse, $[h'k'\ell']$, direction (see Figure 5-9). The least square routine was utilized to calculate the best values of S_{1122} and $(S_{1111}-2S_{2323})$ in Equation (5.2) and the best values of S_{1111} and $(S_{1122}+2S_{2323})$ in Equation (5.5). The best values of S_{1111} and S_{1122} are then

C-2

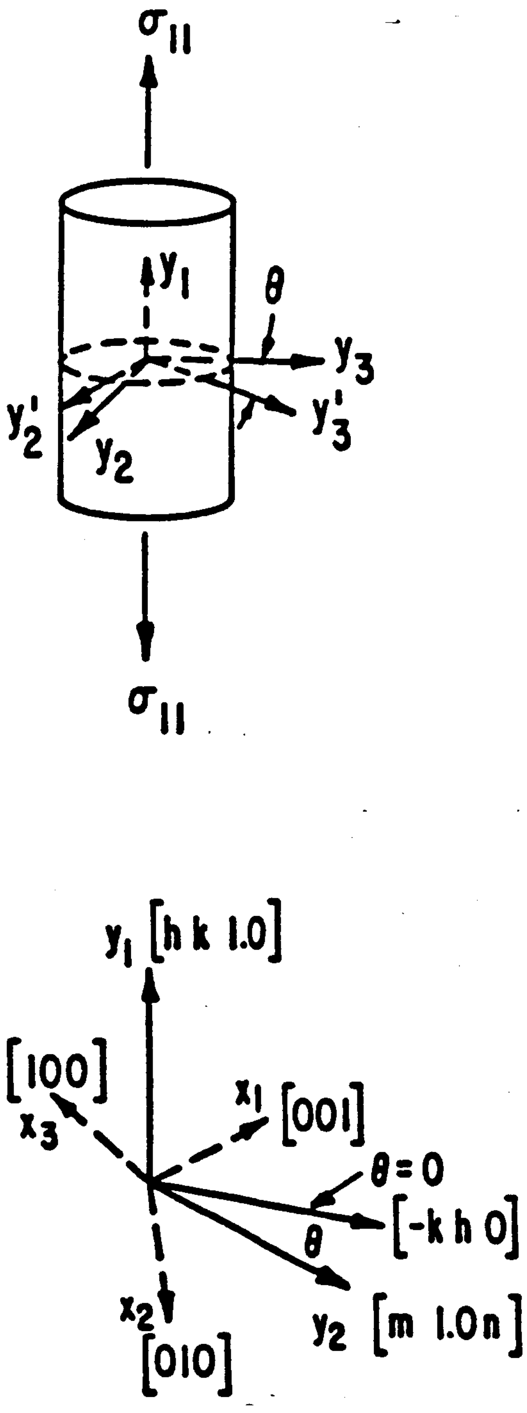
σ_{11}
y_1
θ
y_3
y_2'
y_2
y_3'
σ_{11}
y_1 [h k 1.0]
[100]
x_3
x_1 [001]
$\theta = 0$
[-k h 0]
θ
x_2
[010]
y_2 [m 1.0n]

Figure 5-9 Axis Systems For Equation (4.2).

Table 5-2 Experimental Data For Determining Elastic Material Constants Of Rene N4 At 982°C

NOMINAL [hkℓ]	ACCTUAAL [hhkℓ]]	DIAMETRAL [hkℓ]	E, GPa	ν
TENSILE				
[321]	[-37 -28 10]	[1 -1 1]	162.5	-0.095
[110]	[46 1 35]	[0 -1 0]	136.3	-0.667
[100]	[-26 1 1]	[0 0 1]	80.5	-0.426
[111]	[-14 -10 13]	[1 0 1]	218.0	-0.062
FATIGUE				
[100]	[-4 -1 57]	[0 -1 0]	82.1	-0.37
[111]	[-10 11 -11]	[-1 -1 0]	238.7	-0.211
[321]	[10 33 54]	[-2 -1 1]	133.4	-0.264

compared with the test results in the [100] orientation (e.g., the material principal axis). After the averaging process, the best value of S_{2323} was computed by using either Equation (5.2) or (5.5). The best set of elastic constants was then recovered from S_{1111}, S_{1122} and S_{2323}. These values for Rene N4 at 982°C were 81.3GPa, 90.9GPa, and 0.398 for E, G, and ν, respectively.

5.3 Evaluation of Material Constants in the Constitutive Equation

Some general information and assumptions should be noted prior to the introduction of the material parameter evaluation procedure. These are described as follows.

- The material parameters were evaluated under isothermal conditions. The temperature dependency of the material parameter is not clear because of the variation of the composition and heat treatment of the Rene N4 samples.
- The parameter evaluation procedure was developed for using strain-controlled uniaxial loading data.
- Single crystal tensile response is due to mixed octahedral slip and cube slip in the <110> direction; that is, the first and third terms in Equation (4.14). Therefore, octahedral slip in <112> direction; that is, the second term in Equation (4.14) is negligible. Conversely, crystal creep response is solely caused by octahedral slip in the <112> direction. Thus, octahedral slip and cube slip in the <110> directions are negligible during creep.
- Octahedral slip constants are derived from tests where cube slip is not present; for example, the [100] and [110] orientations. Conversely, cube slip constants are derived from tests where octahedral slip is not present; i.e., [111] orientation.

The kinematic relationships between the applied stress tensor and local shear stresses and between local slip rates and the global strain rate tensors (see Appendix A) yield important information on how to choose appropriate test data for evaluating the material parameters. For example, the resolved shear stresses in all thirty slip systems from an applied stress of 100 MPa in [100], [110], [111], and [123] direction are shown in Table 5.3. The notation is described in Appendix A.

A high strain rate loading in the [100] direction will produce eight equally stressed octahedral a/2<110>{111} slip systems and no stress on the other a/2<110>{111} systems or the cube systems. This result indicates that eight identical slip systems contributing to the total response. Thus, according to Equation A.1 in Appendix A, the relationship between the local slip rates and the global strain rate is simply a scalar factor of 0.312. Because of this constant local/global relationship, test data in the [100] orientation are most desirable for use. By comparison, a load on a [123] oriented specimen will have shear stresses in all the octahedral and cube slip systems. These shear stresses may produce slip on more than one slip system with non-equal slip rate. Some symmetry is also exhibited for loading in the [110] and [111] directions (see Table 5.3). Thus, the tests in the [100], [110], and [111] directions are preferred for evaluating material constants because of the uniformity of stress and strain rate in the octahedral and cube systems.

Material parameter evaluation procedures (discussed next) assume a knowledge of the above. Equations for octahedral a/2<110>{111} slip systems are used as an example in the following derivation, because equations for other slip systems have similar forms. Explanations will

Table 5-3 Distribution Of Resolved Shear Stress In Each Slip System For A Loading Of 1000MPa In The [100], [110], [111], And [321] Directions.

	SPECIMEN ORIENTATION:			
SLIP NO.	[100]	[110]	[111]	[321]
1	408.25	408.25	0.00	349.93
2	0.00	-408.25	0.00	-174.96
3	408.25	0.00	0.00	174.96
4	-408.25	0.00	0.00	-116.64
5	-408.25	0.00	-272.17	-291.61
6	0.00	0.00	-272.17	-174.96
7	408.25	0.00	-272.17	0.00
8	0.00	0.00	0.00	0.00
9	408.25	0.00	-272.17	0.00
10	0.00	-408.25	-272.17	-349.93
11	-408.25	-408.25	-272.17	-466.57
12	-408.25	0.00	0.00	-116.64
13	-235.70	235.70	0.00	0.00
14	471.40	235.70	0.00	303.05
15	-235.70	-471.40	0.00	-303.05
16	-235.70	0.00	-314.27	-269.37
17	-235.70	0.00	157.13	33.67
18	471.40	0.00	157.13	235.70
19	-235.70	0.00	157.13	0.00
20	471.40	0.00	-314.27	0.00
21	-235.70	0.00	157.13	0.00
22	471.40	235.70	157.13	336.72
23	-235.70	235.70	157.13	134.69
24	-235.70	-471.40	-314.27	-471.40
25	0.00	353.55	471.40	454.57
26	0.00	353.55	0.00	151.52
27	0.00	353.55	471.40	404.06
28	0.00	353.55	0.00	202.03
29	0.00	0.00	471.40	252.54
30	0.00	0.00	0.00	-50.51

be given at appropriate locations when necessary. Also, the $\alpha\beta$ superscripts are omitted unless required for clarity.

The parameter evaluation procedure are divided into four major steps:

1) Evaluation of flow equation constants
2) Evaluation of parameters in back stress evolution equation
3) Evaluation of parameters in drag stress evolution equation
4) Evaluation of creep parameters.

This evaluation procedure is conducted squentially for the first two steps. The last two steps can be reversed. Details of each step are described next.

5.3.1 Evaluation of Flow Equation Constants

The saturated state of tensile response is defined as when the material reaches its ultimate tensile strength (UTS) or perfect plastic response during high strain rate loading. In this state, the material is fully hardened and the stress is constant (see the response of tensile loading in the [110] orientation in Figure 5-3). The inelastic strain rate is then equal to the applied strain rate (for a strain-controlled test). The back stress is also assumed to reach its maximum or saturated value. The hardening term of drag stress is assumed to be unchanged, $H_1 \approx H_{11}$, because there is only a small amount of accumulated inelastic work compared to the amount of accumulated inelastic work produced during cycling. Under such conditions, Equation (4.15) becomes

$$|\dot{\gamma}_{SAT}| = D_1 \exp[-A_1(\frac{Z_1}{|\tau_{SAT} - \Omega_{SAT}^{1}|})^{n_{11}}] \qquad (5.7)$$

where the subscript SAT indicates a saturated state. Substituting Equation (4.20) for Z_1 and rearranging Equation (5.7) gives

$$\tau_{SAT}\chi_{SAT} = H_1 + V_1\tau_{SAT^1} + V_2|\tau_{SAT^2}| + V_3\tau_{SAT^3} + \Omega_{SAT^1}\chi_{SAT} \quad (5.8)$$

where

$$\chi_{SAT} = \left[-\frac{1}{A_1}\left(\ell n\frac{|\dot{\gamma}_{SAT}|}{D_1}\right)\right]^{-\frac{1}{n_{11}}} \quad (5.9)$$

Parameter D_1 represents the limiting strain rate. This parameter is assumed to be 10^4/sec in high strain rate test conditions. This value is accepted as a constant for many materials, except under extreme loading rates or very high temperatures (Ramaswamy, 1985; Dame, 1985; Sherwood, 1987). Parameter A_1 is 0.5, which is consistent with the results of Bodner (1979). By assuming $H_1 \approx H_{11}$ and the value of n_{11}, Equation (5.8) becomes a linear equation with unknown parameters H_{11}, V_1, V_2, V_3, and Ω_{SAT^1}. At least five sets of (τ_{SAT}, $\dot{\gamma}_{SAT}$) data are required for evaluating these parameters in a linear least square optimization routine.

These tests could be tension and compression tests in the [100] orientation at two different strain rates and the same tests in the [110] orientation. Choice of [100] orientation is due to symmetry of shear stress on the octahedral slip systems described earlier in Section 4.3. Whereas, choice of [110] orientation is due to the maximum tension/compression asymmetry (refer to Figure 1.2). Note that both orientations are well away from the cube slip regime.

Choice of n_{11} is not as difficult as might be expected. This is because the calculated value for Ω_{SAT1} should be in the range zero and τ_{SAT}. Thus, the suitable range for n_{11} could be identified. Section 5.3.2, discusses how a tighter range can be determined by using anelastic recovery data from a double tensile test. The accumulated inelastic work is small for uniaxial tensile tests in comparison with the value for cyclic tests. Thus, it is reasonable to assume the hardening term H_1 in the drag stress is constant and equal to the initial value, H_{11}, in these tests.

A similar procedure was used for evaluating saturated material parameters for cube slip equations. Recall that Equation (4.26) does not contain tension/compression asymmetry terms, thus the evaluation of H_{31} and Ω_{SAT3} require less experimental data. These tests could be tension and compression tests in the [111] orientation at two different strain rates. Note that specimens loaded in the [111] orientation exhibited cube slip only.

After the above material parameters are determined, the inelastic flow equation for a/2<110> octahedral and cube slip systems are operative (e.g., Equations (4.15) and (4.24)). The next step is to evaluate the material parameters associated with back stress.

5.3.2 Evaluation of Back Stress Constants

Back stress is used to model strain hardening. Because Equation (4.15) is operative, the history of back stress during the monotonic tensile test can be determined by inverting Equation (4.15); that is:

$$\Omega_1(t) = \tau(t) - Z_1(t)/\chi(t) \qquad (5.10)$$

where:

$$\chi(t) = [- \frac{1}{A_1}(\ell n \frac{|\dot{\gamma}(t)|}{D_1})]^{-\frac{1}{n_{11}}} \qquad (5.11)$$

Because $H_1 \approx H_{11}$ and the shear stress, τ, and the local slip rate, $\dot{\gamma}$, are known at each time point during the test, the back stress, Ω_1, can be calculated throughout the test. The back stress rate history is then calculated by using a numerical differentiation routine. Because the inelastic strains and inelastic strain rates cannot be measured with confidence in the elastic loading phase, useful back stress and back stress rate calculations were used only after the yield point. Typical examples for the back stress and back stress rate histories are shown in Figures 5-10 and 5-11, respectively.

Knowing the history of Ω_1 and $\dot{\Omega}_1$ during the tensile test, the material parameters in Equation (4.19) can be evaluated. Parameters F_1 and n_{13}, associated with the inelastic back stress, should be evaluated by using Equation (4.18). Parameters G_1 and n_{12}, associated with the elastic back stress, should be evaluated by using Equation (4.17). Parameter τ_o is set to equal 1 with dimension the same as stress. Because the elastic back stress history is not reliable as explained earlier and both elastic and inelastic components are presented in Equation (5.10), the calculated back stress history is not suitable for use with either Equation (4.17) or Equation (4.18). There are several approaches to solve this problem.

The first approach is based on the assumption of a linear relationship between back stress and resolved shear stress; e.g., $n_{12}=0$.

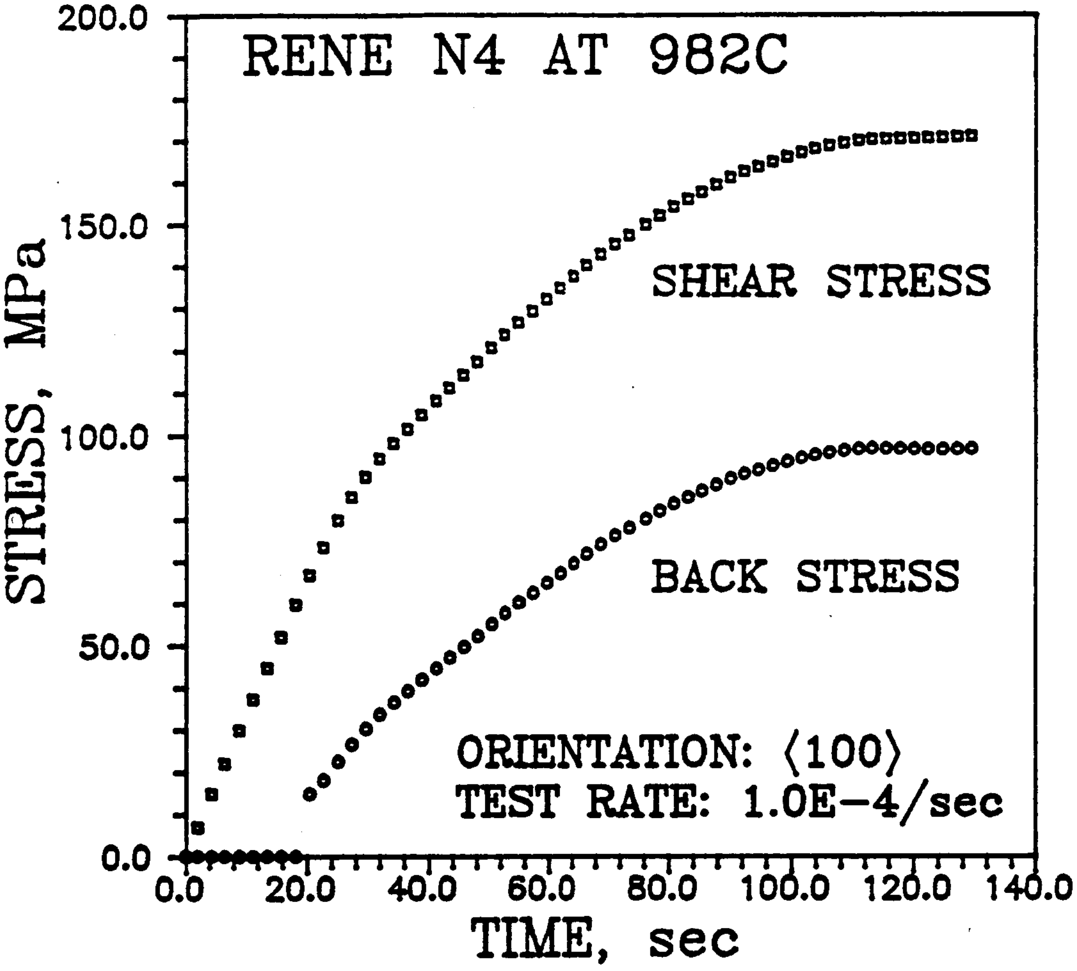

Figure 5-10 Shear Stress And Back Stress Histories For Tensile Test Of Rene N4 In The [100] Orientation At 982°C.

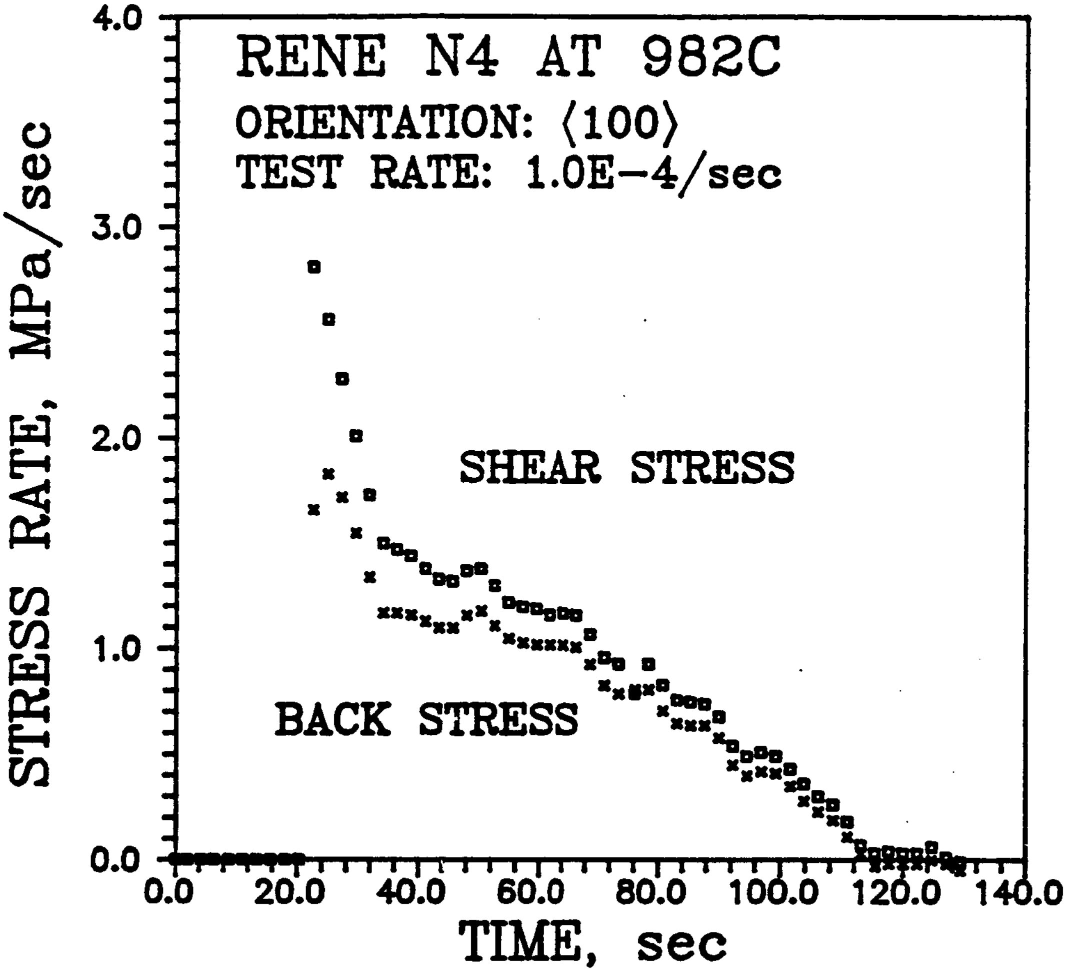

Figure 5-11 Back Stress Rate History For Tensile Test Of Rene N4 In The [100] Orientation At 982°C.

Hence, the back stress-time curve is assumed to have a similar shape to the shear stress-time curve. The elastic back stress-time curve is then simply a straight line between "yield" back stress and the origin (as shown in Figure 5-12). An estimate of G_1 could be obtained by using the value of back stress at yield divided by the value of corresponding shear stress. After G_1 is estimated, Equation (4.17) is inverted to give:

$$\dot{\Omega}^I(t) = \dot{\Omega}(t) - \dot{\Omega}^E(t) \tag{5.12}$$

The inelastic back stress rate history, $\dot{\Omega}^I(t)$, can then be used to evaluate F_1 and n_3 in Equation (4.18); that is:

$$(\dot{\Omega}_1)^I/[\ 1 - \frac{\Omega_1}{\Omega_{SAT1}}] = F_1 |\dot{\gamma}|^{n_{13}} \tag{5.13}$$

A nonlinear regression routine is used to evaluate the best set of parameters F_1 and n_3. Ramaswamy (1985) used this method on Rene 80, a polycrystalline superalloy with the same chemical composition as Rene N4, and obtained successful results. However, for the current study on Rene N4, the observed back stress was almost zero when material yielding occurred. Also, large change in the back stress occurred during the hardening of the material (as shown in region A in Figure 5-10). This result suggests that the back stress in the single crystal may have less dependence on loading in the elastic region. This finding may be caused by different microstructures in polycrystalline and monocrystalline materials. For example, the grain boundary, a major mechanism for creating back stress, is absent in single crystals.

The method described above can almost guarantee good prediction of the strain hardening characteristics in the tensile test. However, this

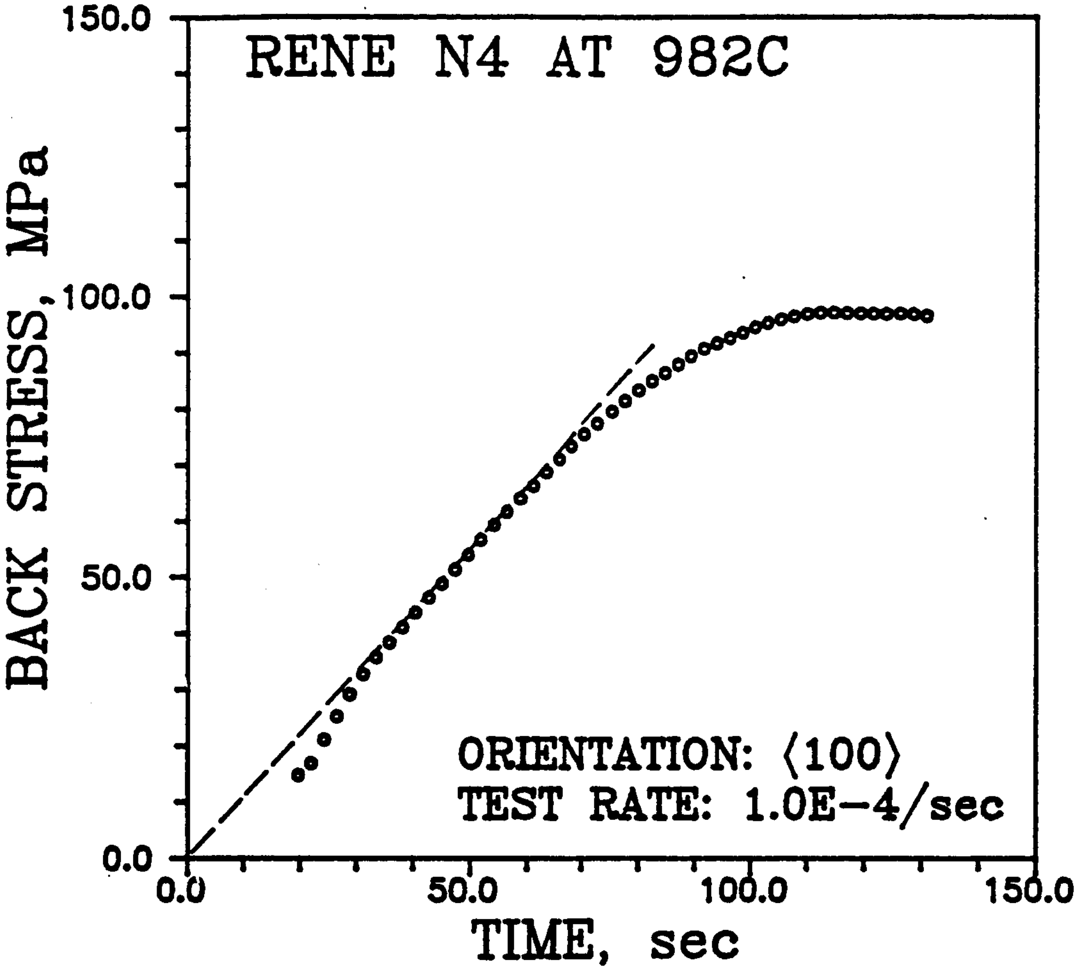

Figure 5-12 Evaluation Of G_1 Based On Linear Relationship Between Back Stress and Resolved Shear Stress.

method provides no measure of the material's anelastic effect such as the recovery during double tensile test of [100] oriented single crystal. Because the magnitude of G_1 in Equation (4.19) strongly dominates the back stress value after elastic unloading, it is assumed the effect of the elastic back stress should be evaluated using the anelastic recovery data mentioned above. In the second approach (discussed next), this material behavior has been investigated and a method has been developed to evaluate the parameters in Equation (4.19).

The second approach uses both tensile strain hardening and anelastic recovery data. During the 120-second hold period at zero stress in the double tensile test, Equation (5.10) can be used to calculate the back stress history. Because all shear stress components are zero and $H_1 \approx H_{11}$, Equation (5.10) reduces to:

$$\Omega_1(t) = - H_{11}/\chi(t) \qquad (5.14)$$

The back stress rate history can then be calculated numerically. Neither back stress nor back stress rate histories contain a contribution from the shear stress because $\tau = \dot{\tau} = 0$. Thus, Equation (4.18) and Equation (5.13) can be used for determining parameters F_1 and n_{13} through use of a nonlinear regression routine. This procedure is illustrated in Figure 5-13.

Knowing F_1 and n_{13}, Equation (4.18) can then be used in Equation (4.16) to determine the elastic back stress rate history in the tensile test; that is:

$$\dot{\Omega}^E(t) = \dot{\Omega}(t) - \dot{\Omega}^I(t) \qquad (5.15)$$

The parameters G_1 and n_{12} in Equation (4.17) are then evaluated using a nonlinear regression routine.

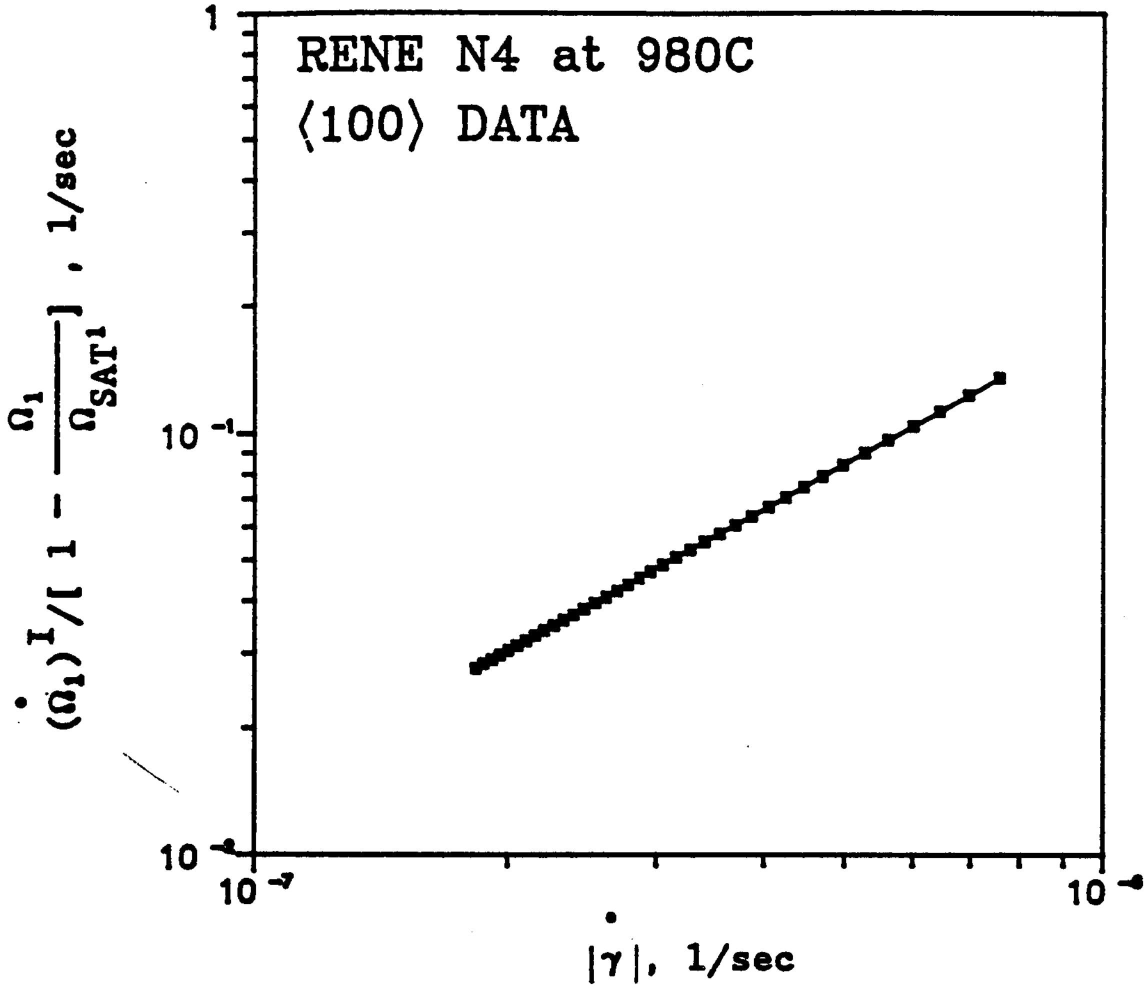

Figure 5-13 Evaluation Of F_1 And n_{12} Using Relaxation Data In Double Tensile Test Of Rene N4 At 982°C.

The second approach described above is considerably better in this study because of its consistency. However, during data analysis the parameter G_1 was found very small, and parameter n_2 was very large. This results suggested both parameters may be calculated from the noisy data and do not represent any significance. A third approach was developed to solve this problem.

In the third approach, parameters G_1 and n_{12} were set equal to zero. Under this condition, Equation (4.19) now contains only the inelastic back stress rate, thus, Equation (4.18) is fully responsible for predicting tensile strain hardening and recovery during zero-stress hold time.

Parameters F_1 and n_{13} were evaluated using both tensile hardening and anelastic recovery data. A set of optimized values were obtained through a optimization process. The necessity for this optimization is demonstrated in Figure 5-14a and 5.14b.

For example, in Figure 5-14a, a prediction of the double tensile test in the [111] orientation was made using parameters F_1 and n_{12} that were determined solely from the tensile curve. Whereas, in Figure 5-14b, same prediction was made using parameters F_1 and n_{12} that were determined solely from the recovery history. Both predictions were not satisfactory. Figure 5-14a under-predicted the strain hardening and Figure 5-14b over-predicted the same property. A optimization process was then utilized to calculate a set of F_1 and n_{12} using both tensile hardening and recovery data.

Recall that the only parameter estimated was n_{11} and all other parameters were all calculated from experimental data. Thus, in the

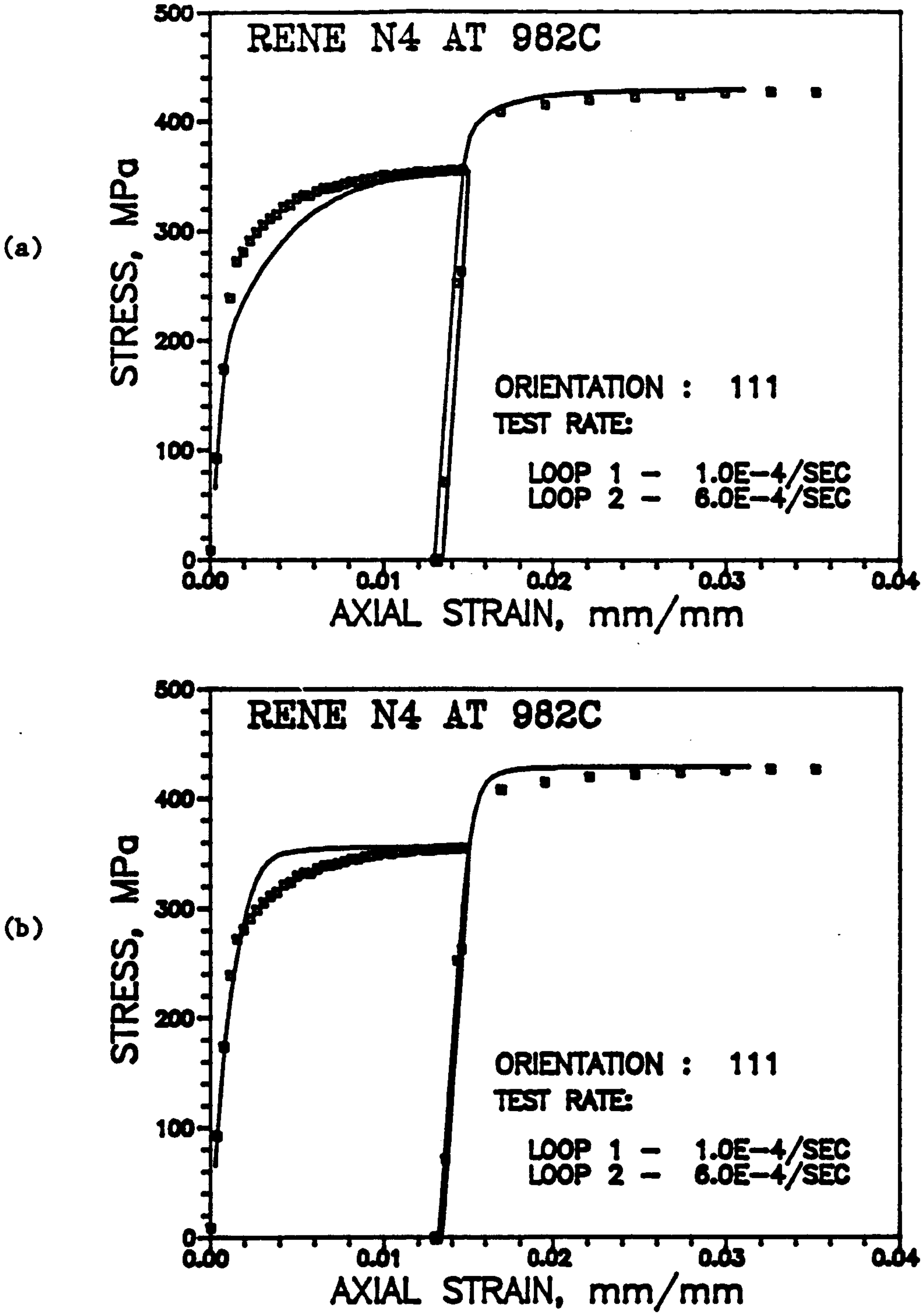

Figure 5-14 Predicted Double Tensile Test In The [111] Orientation Using F_1 and n_{1s} Values Determined From The Tensile Curve (Figure 5-14a) And From The Anelastic Recovery Data (Figure 5.14b)

optimization process, the value of n_{11} was optimized to give new values of F_1 and n_{13} until a best set was obtained. This set of optimized parameters produced a much better prediction than those un-optimized parameters. This result is later shown in Chapter VI.

In the above optimization process, the parameter n_{11} was optimized at the same time. Which is a major advantage of using this approach. Besides, because the anelastic recovery data were used in the process, the parameters F_1 and n_{13} were calibrated with a greater confidence than using the first approach.

The three methods described above should be used depending upon the data base. It is noted that double tensile test provided much more information than regular tensile tests. The anelastic material property plays important role in evaluating the back stress parameters. Thus, evolution equations that have similar form to Equation (4.18) should carefully design the experiments in order to explore the characteristics of the back stress in many aspects.

Parameter τ_o was set to equal unity for all slip systems. This term, although was not used in this research because elastic back stress term was very small, it may be used to control the orientation-dependent strain hardening rate caused by elastic back stress. For example, if τ_o is set to equal the critical resolved shear stress (τ_{CRSS}, a fuction of orientation) the strain hardening rate will vary as a function of orientation. This effect may be used to accout for different strain hardening characteristics observed in the [100] and [110] orientations (see Figure 5-1). Because of the lack of an equation to accurately describe τ_{CRSS} as a fuction of orientation, the possibility for use τ_{CRSS} as τ_o was not futher investigated.

Similar procedures was used to evaluate the parameters in the back stress evolution equation for cube slip. At this time, material parameters in the octahedral and cube slip flow equations; i.e., Equations (4.15) and (4.24), and back stress evolution equations; i.e., Equations (4.19) and (4.25) are all determined. Thus, the model can be used to calculate the responses of tensile test and the first few cycles of fatigue test.

5.3.3 Evaluation of the Drag Stress Constants

The evaluation of constants in the drag stress evolution Equations (4.22) and (4.27), for both the octahedral and cube slip systems, proceeds in a different way from the evaluation of the back stress parameters. Cyclic test data in the [100] and [111] orientations were used to determine the hardening term, H_1, in Equation (4.23) as a function of the accumulated, local inelastic work. Note that the change of H_1 within a loop should not be significant and the parameter m_1 should be obtained from the cyclic hardening during the entire cyclic test.

The history of Z_1 during a high strain rate cyclic test can be determined by rearranging Equation (5.10); that is:

$$Z_1(t) = (\tau(t) - \Omega_1(t))\chi(t) \tag{5.16}$$

Substituting Equation (4.20) for Z_1 and rearranging Equation (5.16) yields:

$$H_1(t) = [\tau(t)-\Omega_1(t)]\chi(t) - [V_1\tau_1(t)+V_2|\tau_2(t)|+V_3\tau_3(t)] \qquad (5.17)$$

where the values for all the parameters are known except for the history of back stress, $\Omega_1(t)$. Because the parameters in the back stress evolution Equation (4.19) are known and the values of $\dot{\gamma}$ at each point on the loop is also known. The back stress history can be determined by integrating Equation (4.19). For example, the back stress Ω_1 at time $t+\Delta t$ can be calculated by:

$$\Omega_1(t+\Delta t) = \Omega_1(t) + \int_t^{t+\Delta t} \dot{\Omega}_1(t)dt \quad . \qquad (5.18)$$

This calculation is performed for the first five to ten loops. The values of each pair of $(\Omega_1, H_1)_i$, at the end of each loop i, are recorded. When the changes between subsequent pairs $\Delta\Omega_1$ and ΔH_1 remain constant, the value of back stress and drag stress at the end of cycle j were extrapolated by:

$$(\Omega_1)_j = (\Omega_1)_i + \Delta\Omega_1(j-i) \qquad (5.19)$$

and

$$(H_1)_j = (H_1)_i + \Delta H_1(j-i) \qquad (5.20)$$

Calculations of back stress and drag stress histories were continued for several cycles until stable values of $\Delta\Omega_1$ and ΔH_1 were present again to allow further extrapolation. This extrapolation procedure resulted in the history of H_1 over a broad range of accumulated inelastic work. As H_1 approached steady state value, H_{12} was estimated. Knowing the values of H_{11}, H_{12} and the values of H_1 at the end of a number of cycles, the parameter m_{11} in Equation (4.23) can be determined by using a standard nonlinear regression routine. A similar procedure was adapted for cube slip.

Because fatigue data are not available for Rene N4 VF317 at 760°C, H_1 and H_3 are assumed to be constants at this temperature. This assumption is made because Rene 80 at 760°C, studied by Ramaswamy (1985), exhibited cyclicly stable responses. Also, the fatigue data of Rene N4 at 982°C exhibited no work hardening or softening. The values of H_1 and H_3 also remained constant at this temperature; i.e., $H_1 = H_{11} = H_{12}$ and $H_3 = H_{31} = H_{32}$. After this step, the constitutive model can conduct high strain rate loading simulations. The next step is to evaluate the parameter for predicting the creep response.

5.3.4 Evaluation of the Creep Constants

The creep constants are material parameters associated with the octahedral slip in the <112> direction. The procedure starts from the inelastic flow Equation (4.27). At steady state creep, Equation (4.27) reduces to the form similar to Equation (5.8) except for those tension/compression asymmetry terms and the value of H_2 remains constant; that is:

$$\tau_{SAT}\chi_{SAT} = H_{21} + \Omega_{SAT2}\chi_{SAT} \qquad (5.21)$$

However, there appears to be a major difference in interpreting Ω_{SAT2} from Ω_{SAT1} and Ω_{SAT3}. The saturated back stress in creep is a function of the resolved shear stress rather than a constant (see Section 3.4, Chapter III). Thus, Equation (5.8) is insufficient for determining material parameters. In this case, an alternative approach (described below) is used.

In evaluating creep constants, parameter H_{21} was assumed to be related to H_{11} because they both are used for characterizing the flow resistance (strain hardening) in the octahedral plane. This flow resistance is also a measure of the strain energy of the dislocations, which is proportional to the square of the magnitude of the Burger's vector. Thus, by comparing the strain energy associated with octahedral slip in the <110> direction with the strain energy associated with octahedral slip in the <112> direction, the relationship between H_{11} and H_{21} can be obtained.

In general, unit dislocation dissociates into partial dislocations from energy consideration. At high strain rate conditions, octahedral slip in <110> direction dissociated into two partial dislocations in γ' precipitate; for example:

$$a/2[\bar{1}01] \rightarrow a/6[\bar{2}11] + a/6[\bar{1}\bar{1}2] \qquad (5.22)$$

(λ_1 and λ_2 in Figure 4-3), whereas, at low strain rate, octahedral slip in <112> direction occurs by dissociation of the dislocation into two superpartial dislocations; for example:

$$a/2[112] \rightarrow a/3[112] + a/6[112] \qquad (5.23)$$

Thus, the energy from Equation (5.21) is two and half times greater than the energy from Equation (5.20). This indicates that the resistance may be two and half times or 60% smaller in creep. This estimation, of course, is not fully accurate because it only considers the strain energy of the dislocations. Other considerations may exist, for example, the APB energy and stacking fault energy. However, they are assumed to have less influence than strain energy of the dislocation.

Thus, using 60% as upper limit, H_{21} was estimated from H_{11} and was used in Equation (5.21) to evaluate the saturated back stress at various creep stress levels; that is:

$$\Omega_{SAT2} = \tau_{SAT} - H_{21}/\chi_{SAT} \qquad (5.24)$$

The saturated back stress values were adjusted by changing the value of H_{21} so that they are in the range between zero and the resolved shear stress. In the calculation of χ_{SAT}, D_2 was set to match D_1. Parameters A_2 and n_{21} were also assumed to be the same as A_1 and n_{11} for the octahedral slip in the <110> direction.

A relationship between Ω_{SAT2} and τ was further established according to Equation (4.29). The parameters C_0 and C_1 were determined by using a standard linear optimization technique. An example of this relationship is shown in Figure 5-15. Knowing these parameters, the next step is to evaluate the back stress constants in Equation (4.28).

The back stress history can be determined by using creep data in Equation (5.10). The back stress rate history was then calculated. Because $\dot{\tau} = 0$ throughout the creep test, parameters F_2 and n_{23} can be evaluated by using primary creep data in Equation (5.13). The parameters G_2 and n_{22} were evaluated by using the initial values of Ω_2 from various creep tests with the same initial loading rate, that is:

$$\Omega_2 = G_2\tau^{n_{22}+1}/(n_{22}+1) \qquad (5.25)$$

A nonlinear regression routine was then used to determine the best values for G_2 and n_{22}. This result is shown in Figure 5-16.

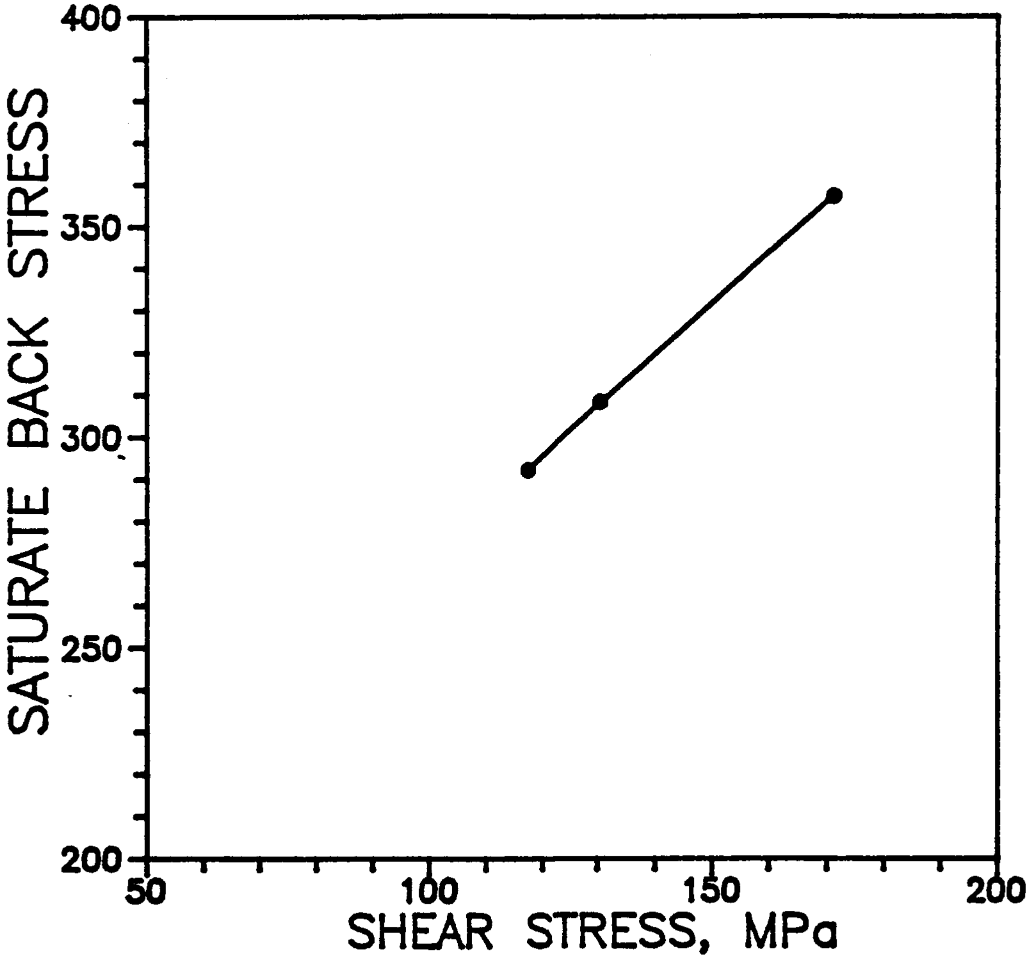

Figure 5-15 Linear Relationship Between Saturated Back Stress, Ω_{SAT}, And Resolved Shear Stress, τ, For Creep Of Rene N4 VF317 At 760°C and 756MPa, 655MPa And 620MPa.

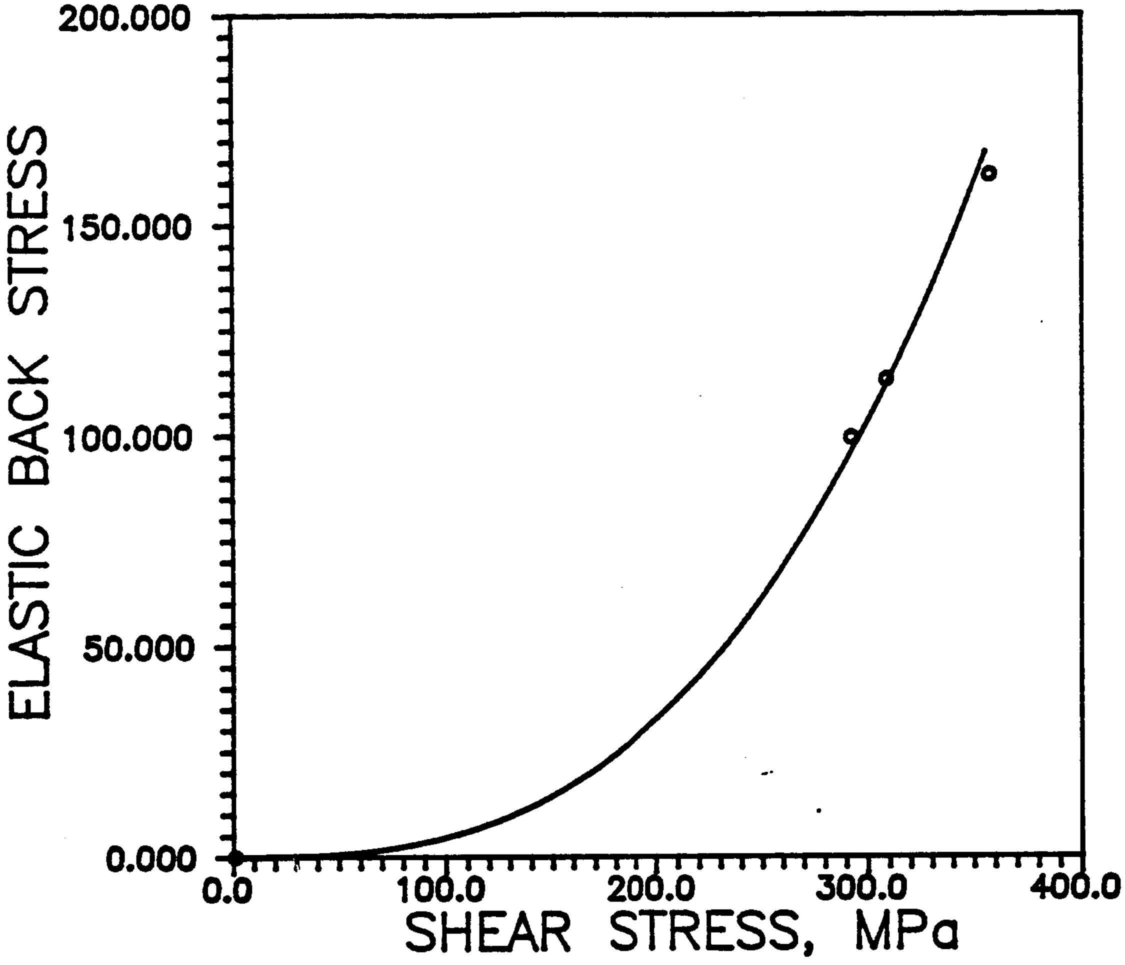

Figure 5-16 Relationship Between Elastic Back Stress, Ω_2, And Resolved Shear Stress, τ, During The Elastic Loading To Creep Stress For Rene N4 VF317 At 760°C.

5.3.5 Evaluation of the Crystal Lattice Rotation Parameters

The parameters to be determined for crystal lattice rotation are K_1 and m in Equation (4.38). In this study, hypothetical values of 10^{-4} and 2 were used for K_1 and m_{22}, respectively. The maximum angular rotation, θ_{max}, was calculated as the angle from the initial specimen orientation to the duplex boundary (see Figure 3.2) and has an upper limit of 10 degree.

Parameter K_2 in Equation (4.40) for calculating the increase of drag stress, H_2^*, due to strain hardening by crystal lattice rotation was set to equal 4000. This value was assumed because of the lack of data.

5.4 Summary of Material Parameter Evaluation

The material parameter evaluation procedure was chained in a loop, as shown in the flow chart in Figure 5-17. After each step was complete, the constitutive model could then perform correlation and predictions to validate the constants. Although flexible, this parameter evaluation procedure still requires a global optimization process. This global optimization is expected to be necessary for a limited data base. As the size of the data base increases, the current procedure should perform well.

The estimation of H_{21} is critical in evaluating other creep parameters. However, within 3 to 5 iterations, a suitable value of H_{21} can be obtained. A summary of material constants for Rene N4 VF317 at 760°C and Rene N4 at 982°C are presented in Tables 5-4 and 5-5, respectively. Model predictions and correlations are presented in the next chapter.

ORIGINAL PAGE IS
OF POOR QUALITY

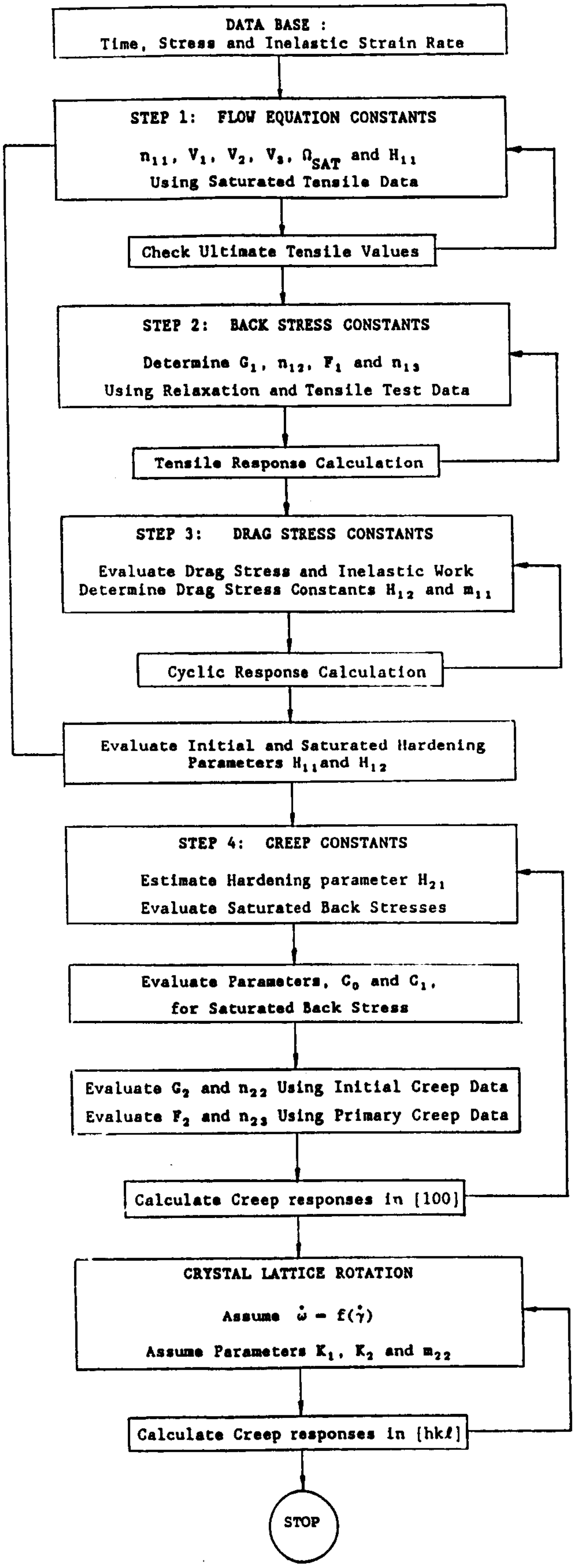
DATA BASE :
Time, Stress and Inelastic Strain Rate
STEP 1: FLOW EQUATION CONSTANTS
n_{11}, V_1, V_2, V_3, Ω_{SAT} and H_{11}
Using Saturated Tensile Data
Check Ultimate Tensile Values
STEP 2: BACK STRESS CONSTANTS
Determine G_1, n_{12}, F_1 and n_{13}
Using Relaxation and Tensile Test Data
Tensile Response Calculation
STEP 3: DRAG STRESS CONSTANTS
Evaluate Drag Stress and Inelastic Work
Determine Drag Stress Constants H_{12} and m_{11}
Cyclic Response Calculation
Evaluate Initial and Saturated Hardening
Parameters H_{11} and H_{12}
STEP 4: CREEP CONSTANTS
Estimate Hardening parameter H_{21}
Evaluate Saturated Back Stresses
Evaluate Parameters, C_0 and C_1,
for Saturated Back Stress
Evaluate G_2 and n_{22} Using Initial Creep Data
Evaluate F_2 and n_{23} Using Primary Creep Data
Calculate Creep responses in [100]
CRYSTAL LATTICE ROTATION
Assume $\dot{\omega} = f(\dot{\gamma})$
Assume Parameters K_1, K_2 and m_{22}
Calculate Creep responses in [hkℓ]
STOP

Figure 5-17 Material Parameter Evaluation Procedure.

Table 5-4 Material constants for Rene N4 VF317 at 760°C

	OCT^1 (i=1)	OCT^2 (i=2)	CUBE (i=3)
D_i	0.10000E+05	0.10000E+01	0.00000E+00
A_i	0.50000E+00	0.50000E+00	0.00000E+00
n_{i1}	0.14000E+01	0.14000E+01	0.00000E+00
H_{i1}	0.39262E+04	0.27758E+04	0.00000E+00
H_{i2}	0.00000E+00	0.00000E+00	0.00000E+00
m_{i1}	0.00000E+00	0.00000E+00	0.00000E+00
V_1	-0.27662E+01	0.00000E+00	0.00000E+00
V_2	-0.53904E+01	0.00000E+00	0.00000E+00
V_3	0.98201E+00	0.00000E+00	0.00000E+00
G_i	0.10000E+00	0.90514E-05	0.00000E+00
n_{i2}	0.00000E+00	0.19727E+01	0.00000E+00
F_i	0.40974E+05	0.35972E+06	0.00000E+00
n_{i3}	0.80567E+00	0.11166E+01	0.00000E+00
Ω_{SATi}	0.20846E+03	0.28350E+02	0.00000E+00
C_0	0.00000E+00	-0.10794E+03	0.00000E+00
C_1	0.00000E+00	0.68145E+00	0.00000E+00
K_1	0.00000E+00	0.10000E+04	0.00000E+00
m_{i2}	0.00000E+00	0.20000E+00	0.00000E+00
K_2	0.00000E+00	0.00000E+00	0.00000E+00

Table 5-5 Material constants for Rene N4 at 982°C.

	OCT^1 (i=1)	OCT^2 (i=2)	CUBE (i=3)
D_i	0.10000E+01	0.00000E+00	0.10000E+01
A_i	0.50000E+00	0.00000E+00	0.50000E+00
n_{i1}	0.53000E+00	0.00000E+00	0.70000E+00
H_{i1}	0.20510E+05	0.00000E+00	0.71841E+04
H_{i2}	0.00000E+00	0.00000E+00	0.00000E+00
m_i	0.00000E+00	0.00000E+00	0.00000E+00
V_1	-0.40415E+02	0.00000E+00	0.00000E+00
V_2	-0.28231E+02	0.00000E+00	0.00000E+00
V_3	0.17661E+02	0.00000E+00	0.00000E+00
G_i	0.00000E+00	0.00000E+00	0.00000E+00
n_{i2}	0.00000E+00	0.00000E+00	0.00000E+00
F_i	0.21619E+07	0.00000E+00	0.16000E+06
n_{i3}	0.12108E+01	0.00000E+00	0.11202E+01
Ω_{SATi}	0.95293E+02	0.00000E+00	0.61838E+02

CHAPTER VI

COMPARISON OF THE MODEL CALCULATIONS AND EXPERIMENTAL RESULTS

All the model calculations used material parameters which were determined in Chapter V (see Tables 5-4 and 5-5). Correlation between the model calculations and the experimental data that were used for evaluating material constants are presented first. Comparison between model predictions and other experimental results are then given. The constitutive model was also exercised under conditions for which no data were available.

6.1 Comparison of Experimental and Calculated Results for Rene N4 VF317 at 760°C

As listed in Table 5-4, material parameters for Rene N4 VF317 at 760°C, were evaluated only for octahedral a/2<110>{111} and a/2<112>{111} slip systems. Material parameters for the cube slip systems were not evaluated because of the lack of data, and they were set to zero. Thus, calculations were made only in the orientations which exhibited predominant octahedral slip. The features of the model that were exercised include orientation dependent stress-strain response, cyclic hardening and softening, primary and secondary creep response, and crystal lattice rotation.

6.1.1 Monotonic Tensile Calculations

Flow equation constants and back stress constants were determined from the ultimate tensile strength in the [100] and [110] orientations (see Figure 5-1). The value of saturated stress at a order higher strain rate was estimated to evaluate the strain rate sensitivity exponent, n_{11}, in the flow equation. The ratio between 0.2% yield strengths in tension and compression from PWA1480 data (see Figure 1-2, Shah and Duhl ,1984) was used to estimate the ultimate compressive strength for both orientations. The hardening parameters, F_1, G_1 and n_{13}, in the back stress evolution Equation (4.19) were calculated from the [100] response. Parameter n_{12} was set to zero. These parameters were evaluated by using the first approach described in Section 5.3.2, Chapter V because neither double tensile tests nor other relaxation tests were available. Also, note that all the tensile calculations were influenced by octahedral <112> slip systems, which are primarily used for modeling the single crystal creep response.

6.1.1.1 Orientation Dependence

Shown in Figure 6-1 are correlation between the model (dotted line) and experimental data in the [100] orientation and the comparison between model predictions (solid lines) and the experimental results in the nominal [110] and [310] orientations. The model correlates well with the data in the [100] orientation. However, significant mismatch in the elastic modulus for the predicted and experimental response in the [310] orientation was observed. This mismatch was thought to be caused by inaccurate specimen orientation that has been used in the calculation.

Recall that the observed tension/compression asymmetry for VF317 is not consistent with the experimental results for PWA 1480 (see Figure 1-2); i.e., the yield stress for the [310] specimen, about 20° from [100] in the [100]-[110] boundary, is far above the expected level. The difference in the experimental and calculated elastic modulus suggests

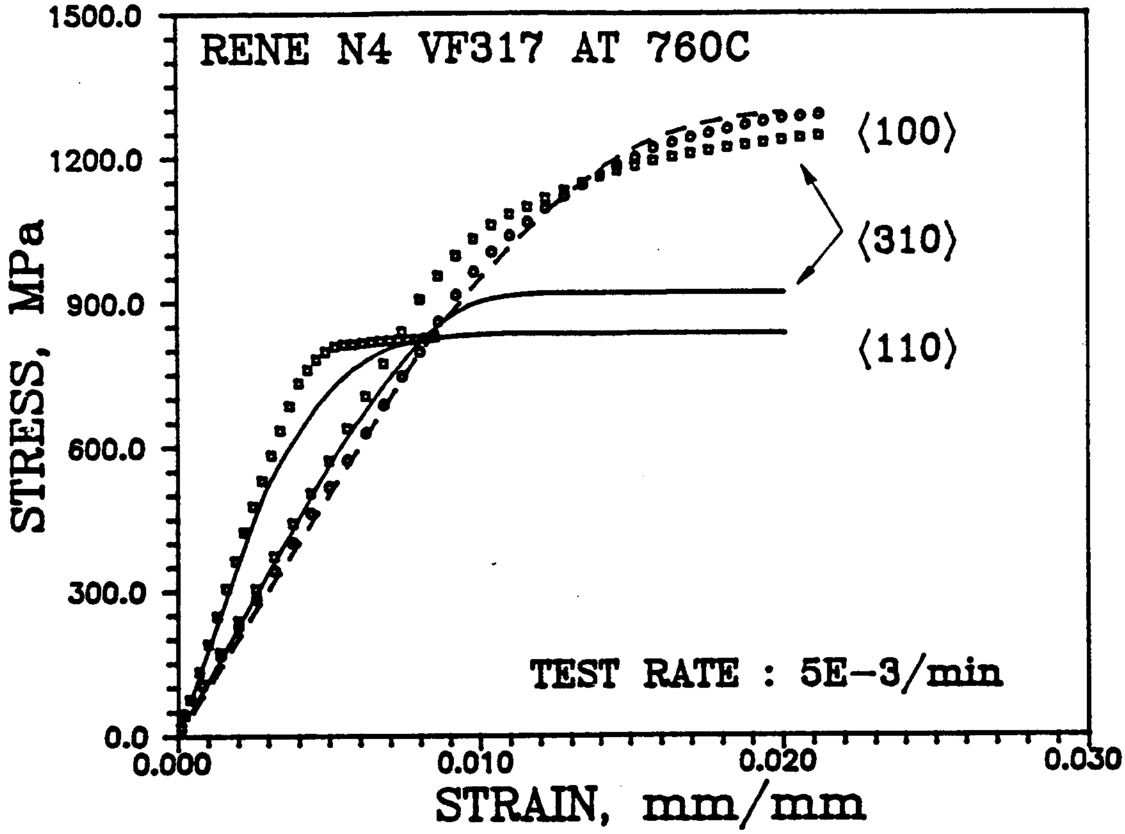

Figure 6-1 Comparison Between Model Predictions And The Experimental Results In The Nominal [100], [110] and [310] Orientations For Rene N4 VF317 At 760°C.

that the specimens in this data set designated as being in the [310] direction are probably much closer to the [100] orientation. More inconsistency was observed in creep data for samples in the [310] orientation. This will be discussed in a later section.

6.1.1.2 Strain Rate Sensitivity

Predictions of monotonic tensile response in the [100] orientation at strain rates from 10^{-7}/sec to 10^{-3}/sec are shown in Figure 6-2. The model predictions showed typical strain rate-dependent tensile response; i.e., the yield strength and the ultimate tensile strength increase as the strain rate increases. Because of the lack of data, quantitative comparison between the model and the data is not possible.

6.1.1.3 Tensile Response at Tntermediate Strain Rate

The model prediction for a tensile test at 10^{-7}/sec (shown in Figure 6-2) was used to investigate the interaction between the octahedral <110> and <112> slip systems. The response had a anomalous strain hardening portion which was caused by presence of the <112> slip systems. Shown in Figures 6-3 and 6-4 are local slip rates for octahedral <110> slip (slip 1) vs octahedral <112> slip (slip 14) as a function of time at two strain rates. Notice that the <112> slip system contribute more to the total strain at low strain rate (Figure 6-3) than at high strain rate (Figure 6-4) loading conditions. At strain rates higher than 10^{-5}/sec, the influence from the<112> slip systems are minimal. Thus, there appear to be separation between creep and plasticity at the higher strain rates.

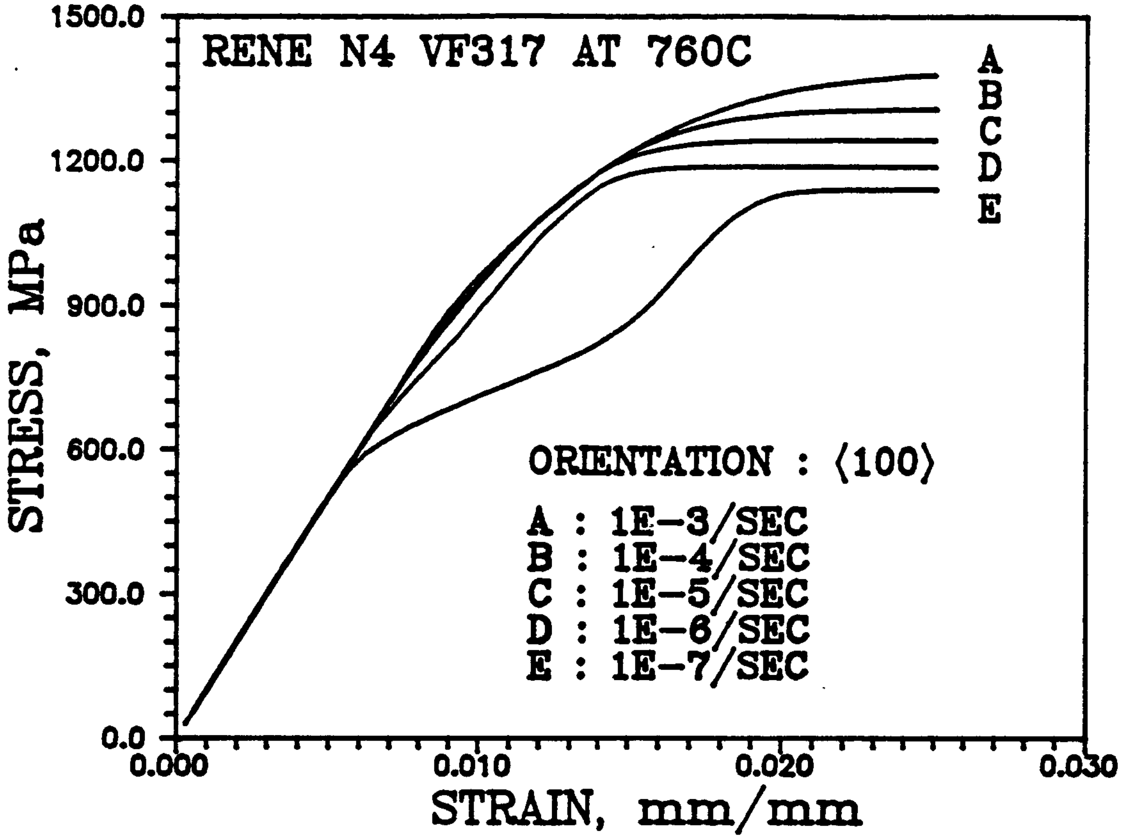

Figure 6-2 Model Predictions Of Tensile Tests Of Rene N4 VF317 In The [100] Orientation At Five Different Strain Rates at 760°C

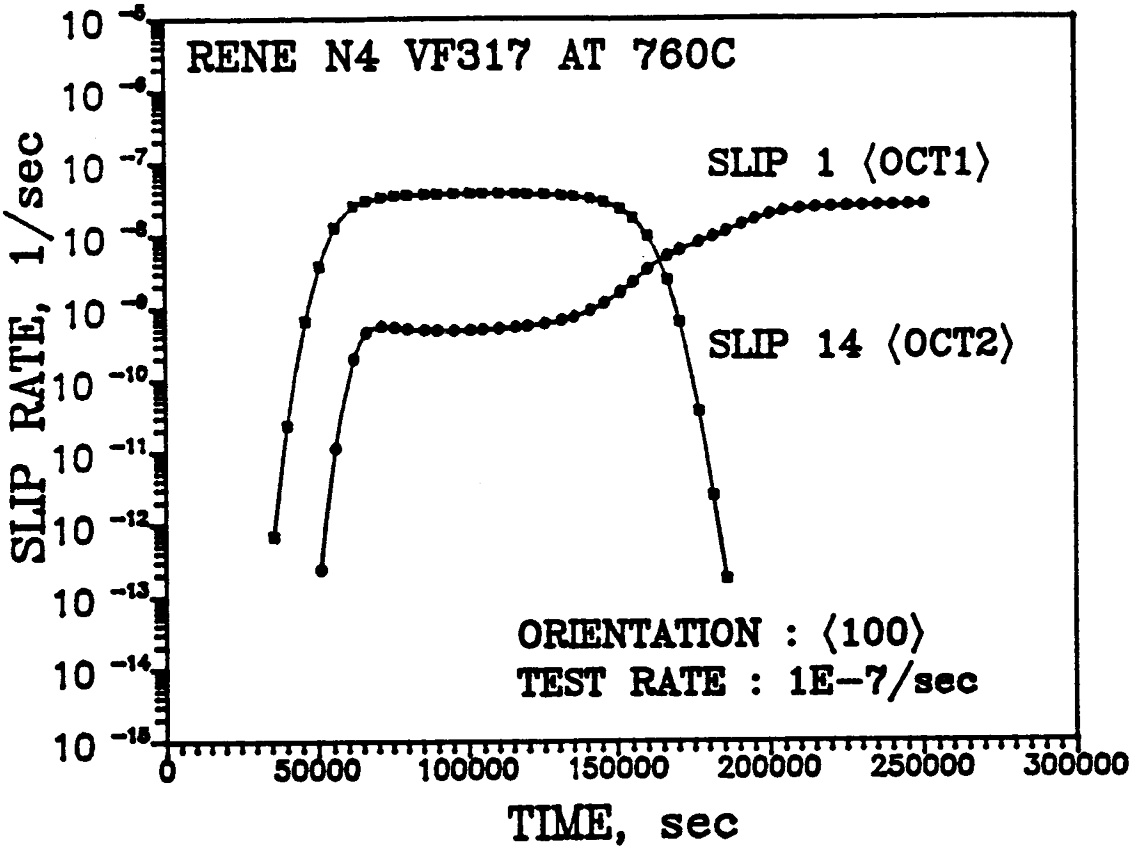

Figure 6-3 Comparison Between Calculated Local Slip Rate, $\dot{\gamma}$, Of Octahedral a/2<110> (SLIP 1) and a/2<112> (SLIP 14) Slip Systems For Tensile Response Of Rene N4 VF317 In The [100] Orientation At 760°C And Strain Rate Of 10^{-7}/min

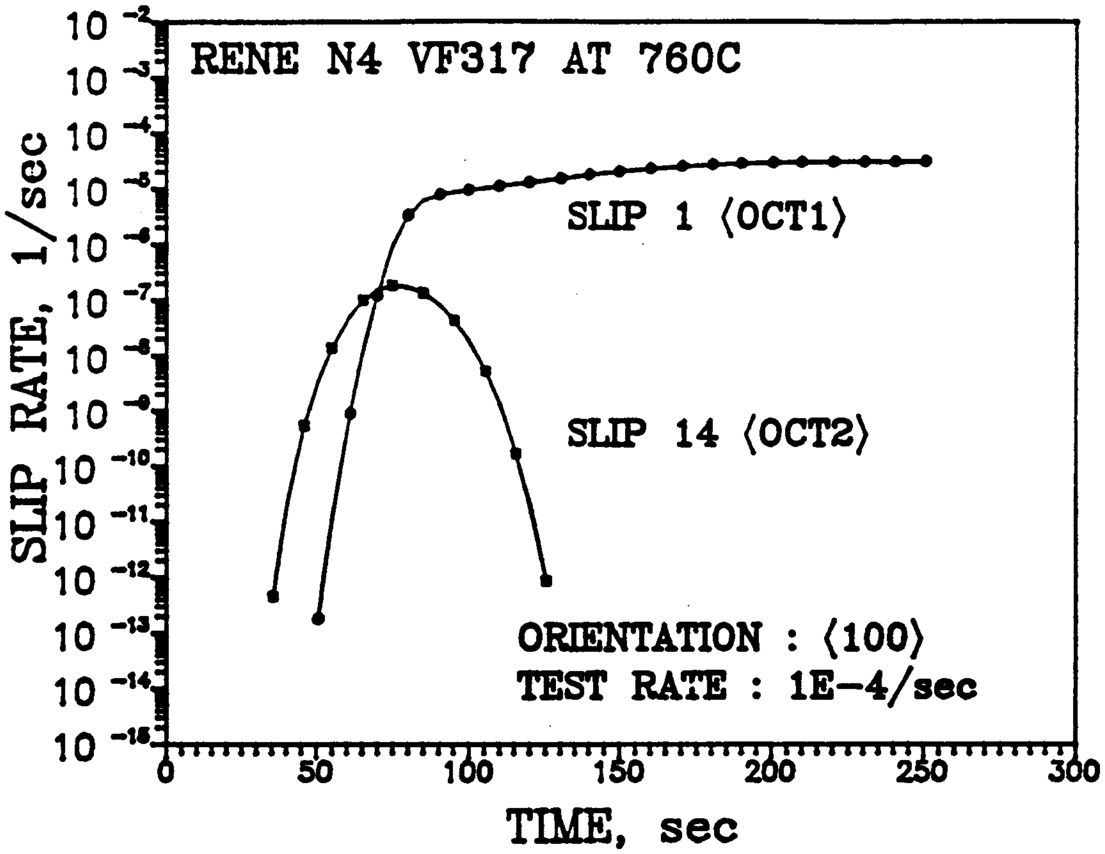

Figure 6-4 Comparison Between Calculated Local Slip Rate, $\dot{\gamma}$, Of Octahedral a/2<110> (SLIP 1) and a/2<112> (SLIP 14) Slip Systems For Tensile Response Of Rene N4 VF317 In The [100] Orientation At 760°C And Strain Rate Of 10^{-4}/min

6.1.2 Fatigue Calculations

Because no fatigue data were available for Rene N4 VF317 at 760°C, it is assumed at this temperature that the material exhibits no strain hardening or softening. This assumption is based on Ramaswamy's work on Rene 80 (1985) when he found that Rene 80 was cyclicly stable at 760°C. Thus the parameter m was set equal to zero. Calculations of cyclic responses without cyclic hardening or softening in [100] and [110] orientations are shown in Figures 6-5 and 6-6, respectively. As expected, the prediction for the [100] orientation showed larger peak stress in tension than in compression, whereas, the calculation in the [110] orientation showed an opposite pattern, e.g. larger peak stress in compression than in tension.

6.1.3 Creep Calculations

Creep response was primarily modeled by octahedral <112>{111} slip system. The flow equation constants, D_2, A_2 and n_{21} were carried over from octahedral a/2<110>{111} slip system. After the hardening constant H_{21} was estimated from H_{11}, steady state creep rates in the [100] orientation were used to determine the saturated back stress at each creep stress level. Primary creep response in the [100] orientation at 655MPa was then used to determine the back stress constants as described in Section 5.3.4, Chapter V. Hypothetical values were assigned to lattice rotation parameters to exercise the model. Because of limited data, model calculations are intended to demonstrate features of the constitutive model rather than correlation with experimental data.

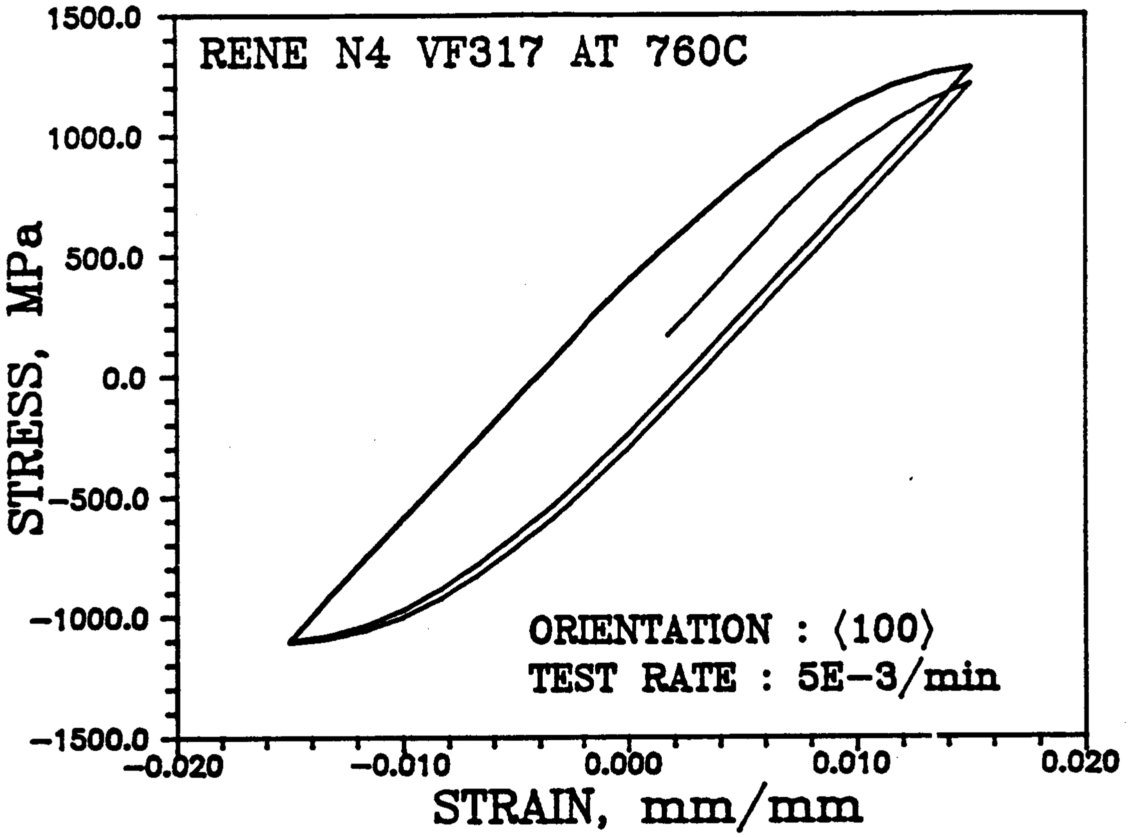

Figure 6-5 Predicted Cyclic Response Of Rene N4 VF317 In The [100] Orientation At 760°C

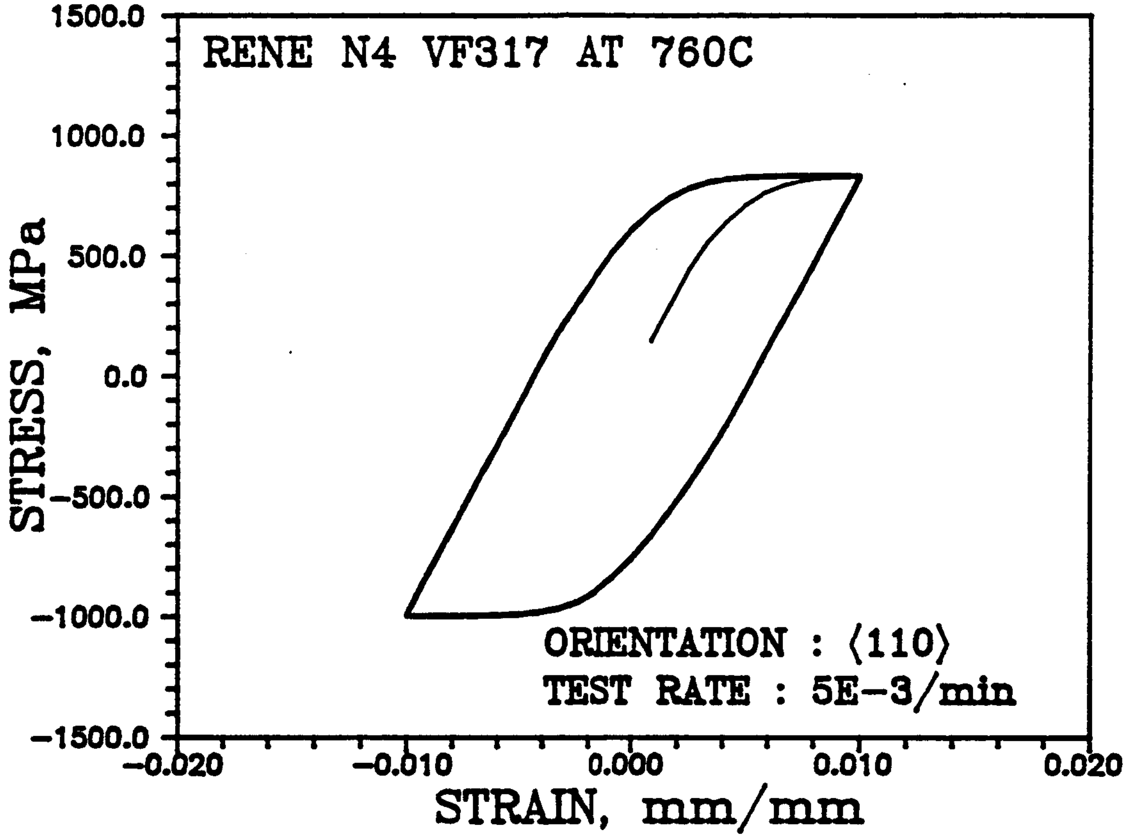

Figure 6-6 Predicted Cyclic Response Of Rene N4 VF317 In The [110] Orientation At 760°C

6.1.3.1 Creep Response along the [100]-[110] Boundary

The creep response in the [100] orientation at creep stress of 756MPa, 655MPa and 620MPa were calculated, and are compared with experimental data in Figure 6-7. The model correlates well with the experimental data at 655MPa. The calculated steady state creep rates also correlated well with the data.

The experimental data from creep rupture tests usually do not yield reliable data at the beginning of a test. For example, the initial loading rate to reach the creep stress level was not known. This information may be critical to the model because it affects the G_1 term in the back stress evolution equation. It is also believed the subsequent creep response can be affected by the initial loading rates. Significant variation in creep response for increasing stress level for IN100 at 732°C have been observed (Stouffer, 1986) and correlated with the initial loading rate. Additional difficulty because of poor alignment, strain measurement system, and inherent differences from specimen to specimen also add to the inconsistency of the data. For example, the nominal [310] oriented sample exhibited stronger creep resistance than [100] oriented sample for Rene N4 VF317 tested at 760°C and 622MPa. This is inconsistent with many published nickel-base single crystal creep data (see Figure 3-8).

Calculations for creep responses at 655MPa were also made along the [100]-[110] boundary. Each computation was made in three degree increments away from the [100] orientation (label A-F in Figure 6-8). These results are shown in Figure 6-9. Lattice rotation was assumed to be zero along the [100]-[110] duplex boundary in the current model.

The model predictions near the [100] orientation, for example, B and C, were not much different from the prediction in the [100]

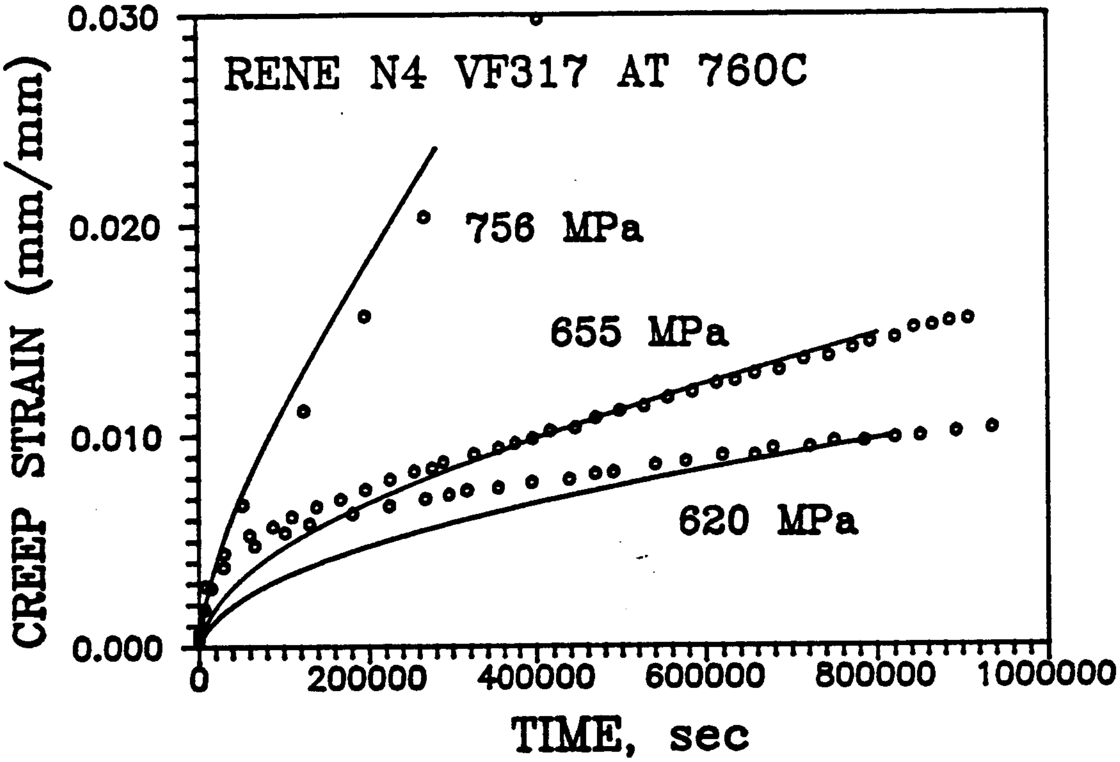

Figure 6-7 Comparison Between Experimental Data and Predicted Creep Responses Of Rene N4 VF317 At 760°C and 756MPa, 655MPa And 620MPa In The [100] Orientation.

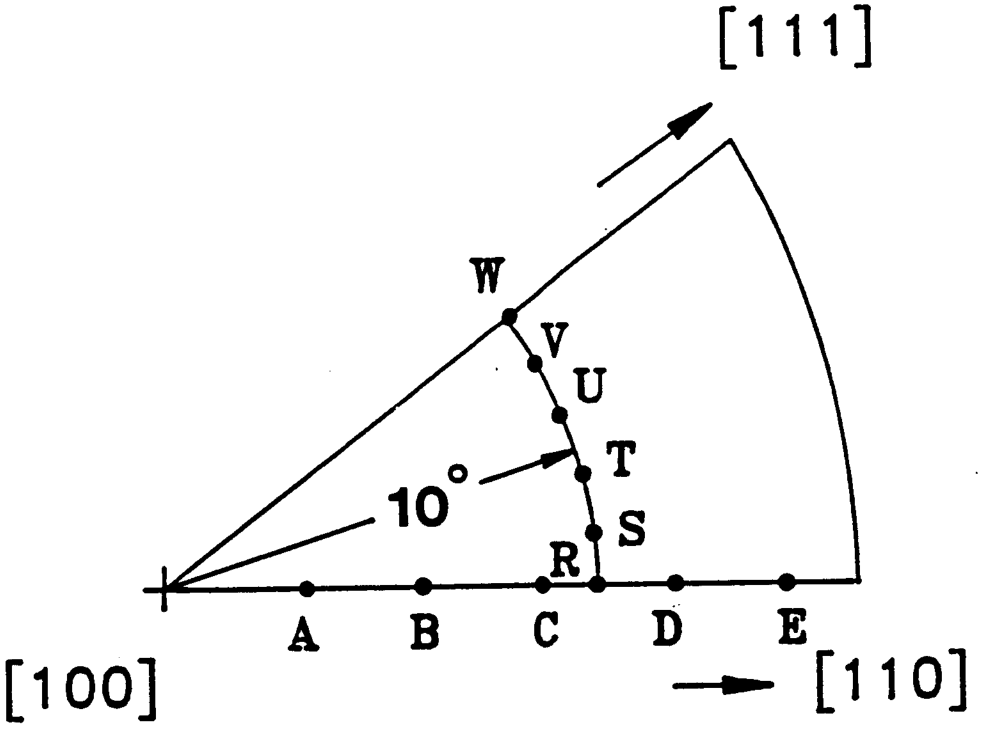
[111]
W
V
U
T
S
R
10°
A
B
C
D
E
[100]
[110]

Figure 6-8 The Orientations In Which Creep Calculations Were Made.

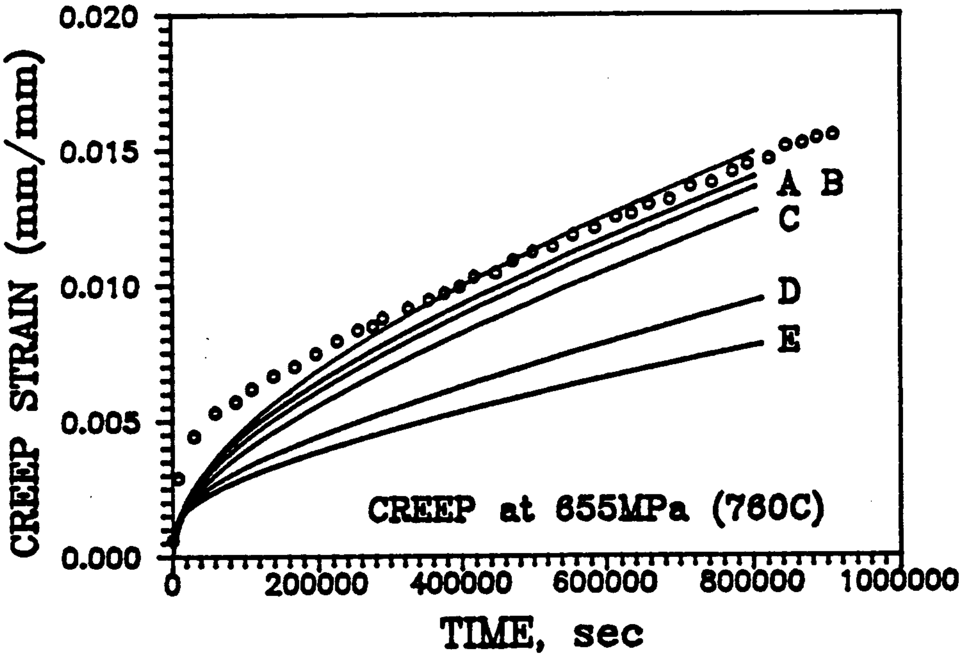

Figure 6-9 Predicted Creep Responses Of Rene N4 VF317 At 760°C And 655MPa Along The [100]-[110] Boundary.

orientation. Although there is no crystallographic symmetry for those samples (e.g., they may have different number of active slip systems) in orientations other than [100], the responses for samples near the [100] orientation should be similar. This property is predicted.

The predicted creep response along the [100]-[110] were not totally consistent with the published trends. For example, the calculated result for secondary creep rates were decreasing with increasing angle away from the [100] orientation. This mismatch was thought to caused by absence of lattice rotation for duplex slip when sample was in the [100]-[110] boundary.

6.1.3.2 Crystal Lattice Rotation

The constitutive model was exercised for computing lattice rotation. Predictions were made in orientations 10° away from the [100] orientation and 9° apart from each other (label R-W in Figure 6-8). These results are shown in Figure 6-10. The responses for sample R and W are significantly different. The model predicted larger primary creep strain, primary creep strain rate, and secondary creep rate for samples required greater lattice rotation. For example, the primary creep strain for sample W could be as high as 18%, whereas, it was not noticeable for sample R. The lattice rotation as a function of time is shown in Figure 6-11. All the rotations are completed in the primary creep stage. This results are consistent with the trends published in the literatures.

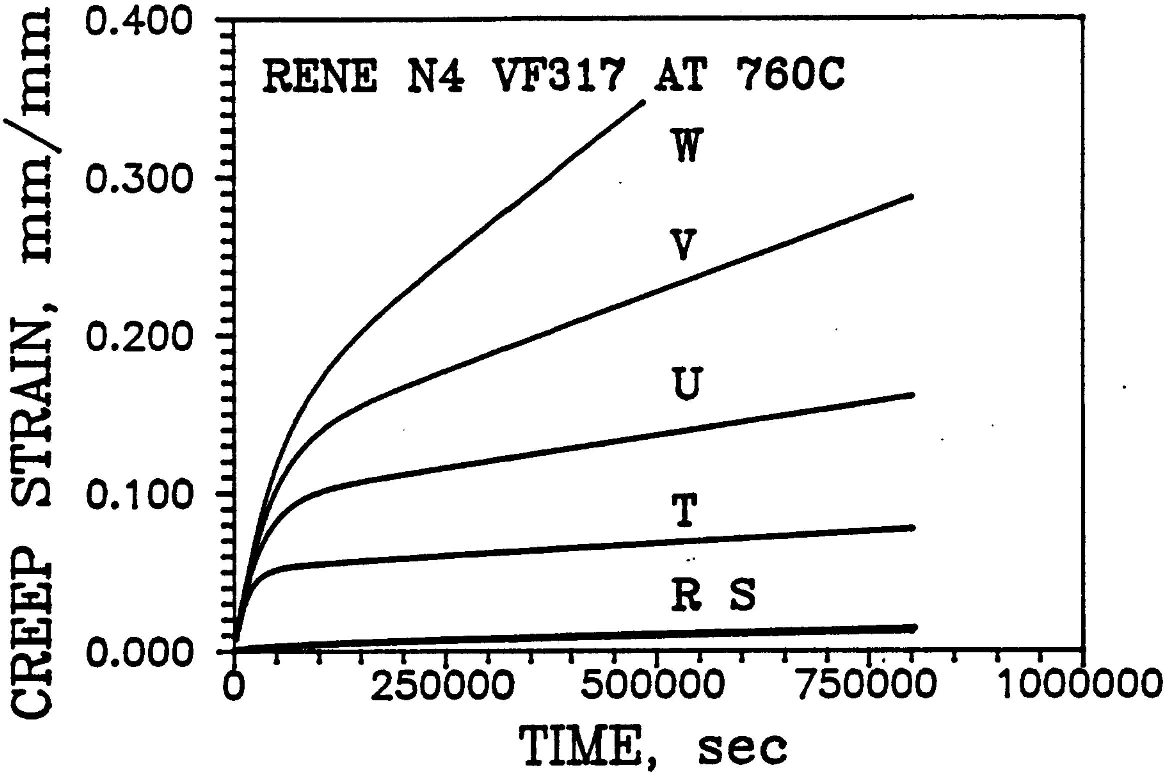

Figure 6-10 Predicted Creep Responses Of Rene N4 VF317 at 760°C And 655MPa In Orientations 10° Away From [100] And 9° Apart From Each Other (Label R-W In Figure 6-8).

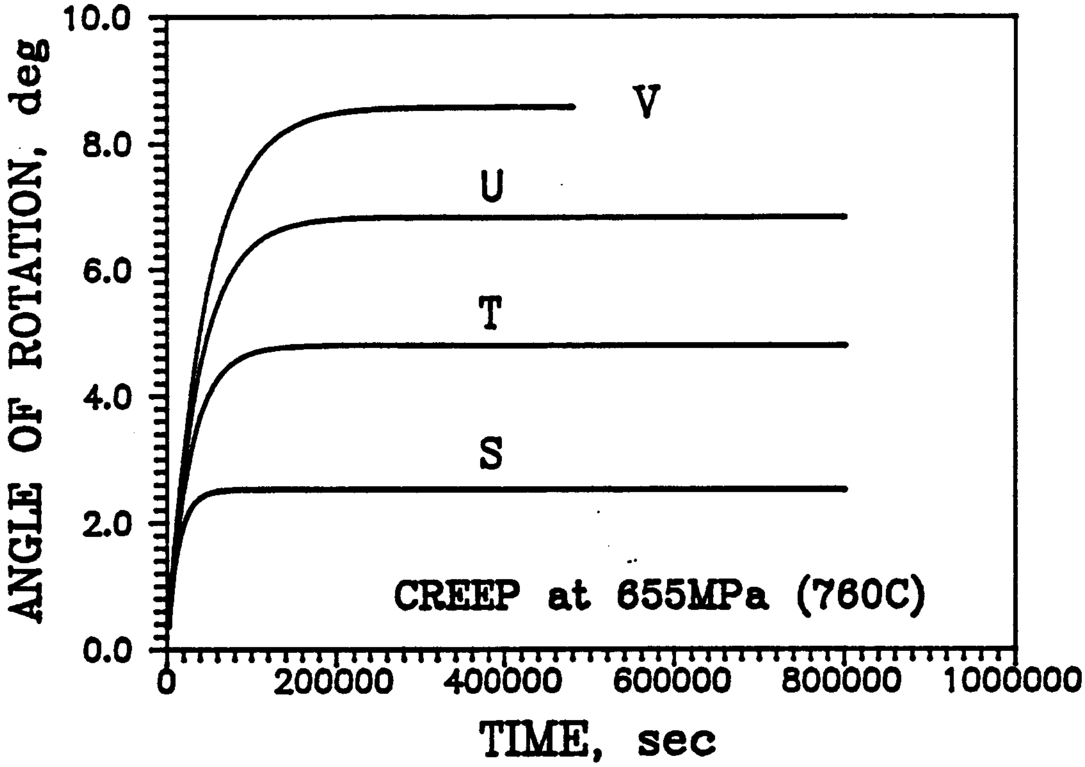

Figure 6-11 Amount Of Lattice Rotation As A Function Of Time For Creep Calculations In Figure 6-10.

6.2 Comparison of Experimental and Calculated Results for Rene N4 at 982°C

The calculations were performed using constants derived for Rene N4 at 982°C in Chapter IV (Table 5-5). Material constants for octahedral <112>{111} slip systems were not evaluated since no creep data were available, and they were set to equal zero. The features of the model that were exercised are orientation dependent stress-strain response, anelastic recovery, cyclic hardening and softening, and cyclic response with hold time.

6.2.1 Monotonic Tensile Calculations

Flow equation constants and back stress constants were determined from tensile tests in the [100] and [111] orientations (see Table 4-1) and the first quarter loop in Figures 2-3 and 2-4. The ratio between peak tensile stress and peak compressive stress in fatigue test in the [100] orientation was used for estimating the ultimate compressive strength in the [100] orientation. The ultimate tensile strength and estimated ultimate compressive strength in the [110] orientation were also used for evaluating the tension/compression asymmetry parameters. The saturated stress values in the second loop of the double tensile tests in the [100] and [111] orientations were used to establish the strain rate sensitivity. The hardening parameters, F_1 and n_{13} in Equation (3.19), were calculated from the [100] and [111] responses using the third approach described in Section 5.3.2, Chapter V.

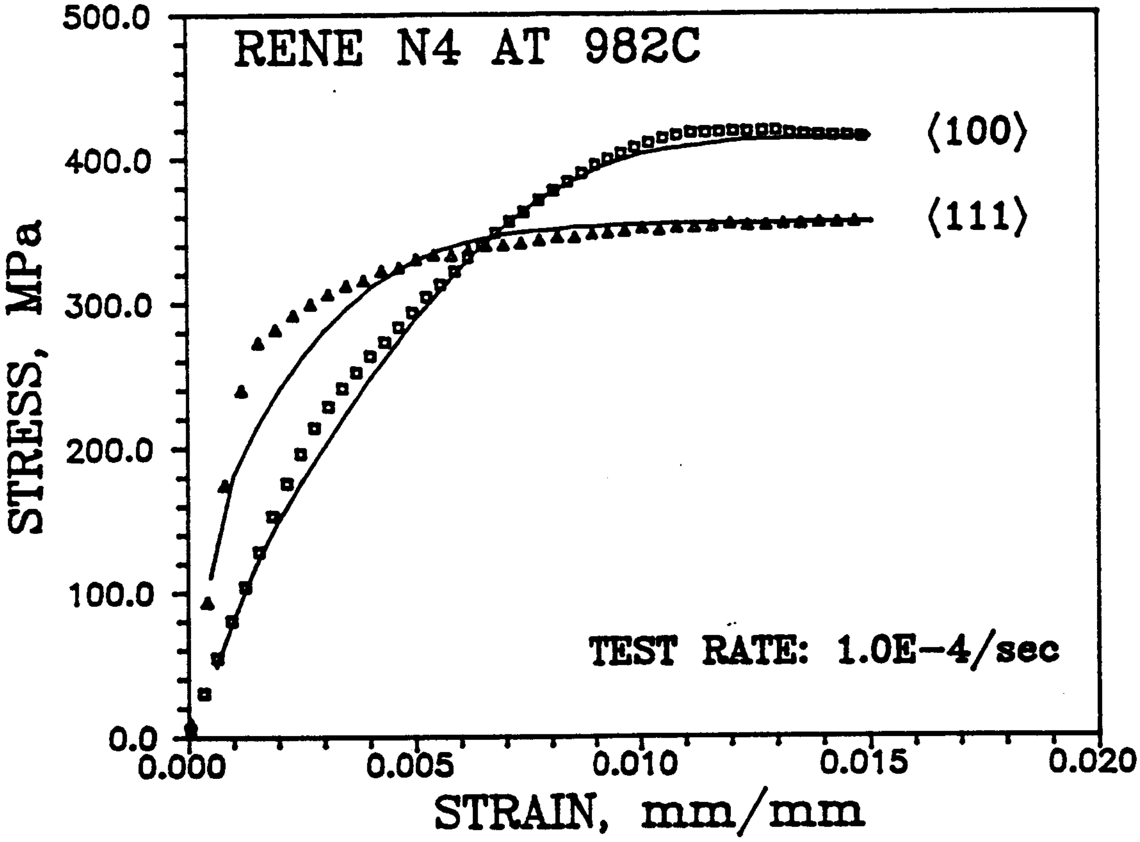

Figure 6-12 Correlation Between Model Calculations And Experimental Data For Tensile Tests Of Rene N4 In The [100] and [111] Orientations At 982°C

6.2.1.1 Orientation Dependence

Shown in Figure 6-12 are correlations between the model and experimental data in the [100] and [111] orientations. The stress-strain response was calculated for a constant strain rate of 10^{-4}/sec for both orientations. The calculated response in [100] orientation matches very well with the data. However, the calculation in [111] did not match well in the hardening portion. This mismatch is caused by initial interaction between cube and octahedral slip in the calculation. For example, the yield stress in [100] orientation is smaller than in the [111] orientation. Thus, a larger octahedral slip rate was present below the critical resolved shear stress in the [111] orientation. This is shown in Figure 6-13 where the local slip rates as a function of time are compared for a cube slip system(slip 25) and a octahedral slip system (slip 11) during tensile loading in the [111] orientation.

Comparison between model predictions and the experimental data for tensile tests in the [110] orientation loaded at 10^{-4}/sec strain rate and in [321] orientation loaded at 5.0×10^{-4}/sec strain rate are shown in Figure 6-14. The model predicted very well the elastic moduli and the strain hardening portion. The predicted ultimate tensile strength are also very close to the experimental data.

6.2.1.2 Strain Rate Sensitivity

Strain rate-dependent stress-strain response is demonstrated in Figure 6-15 for tensile loading in the [100] orientation at 10^{-4}/sec, 6×10^{-4}/sec and 10^{-3}/sec strain rates. Similar to Figure 6-2, the predicted responses at 980°C showed typical strain rate-dependent

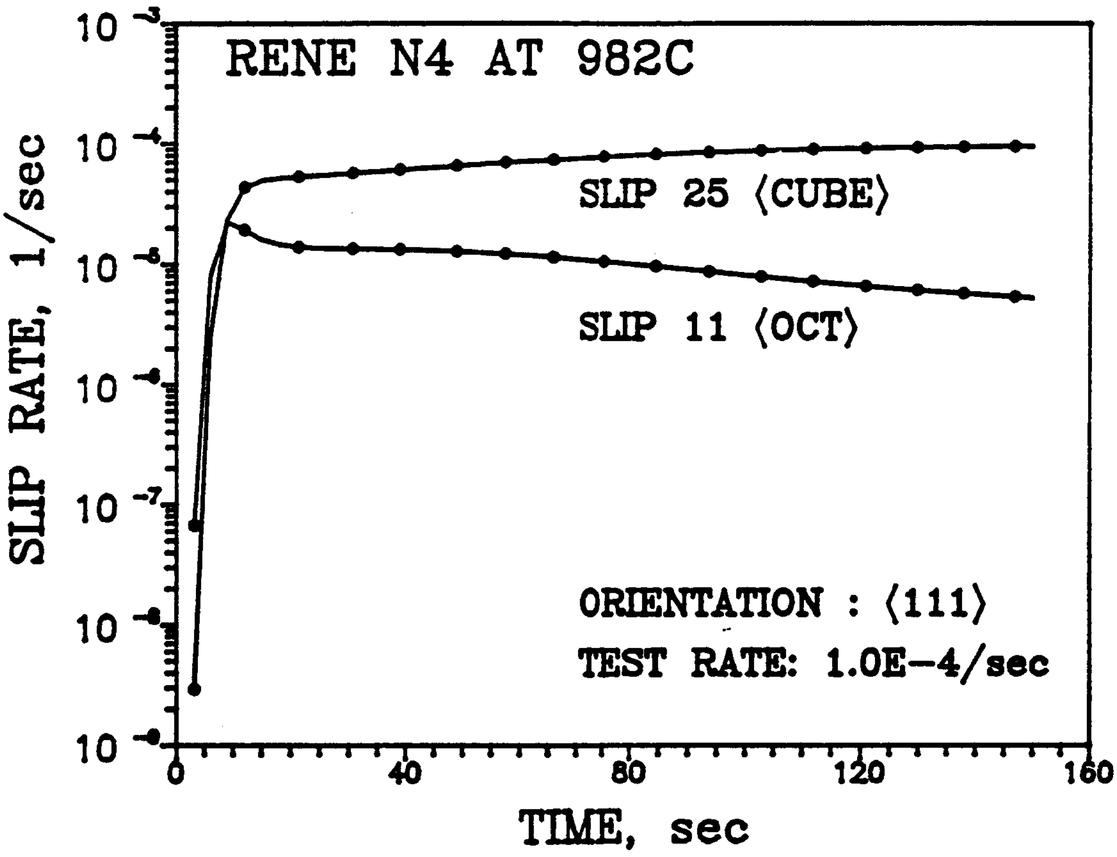

Figure 6-13 Comparison Between Calculated Local Slip Rate $\dot{\gamma}$ For A Cube Slip System (Slip 25) And A Octahedral Slip System (Slip 11) In Tensile Response Of Rene N4 In The [111] Orientation At 982°C

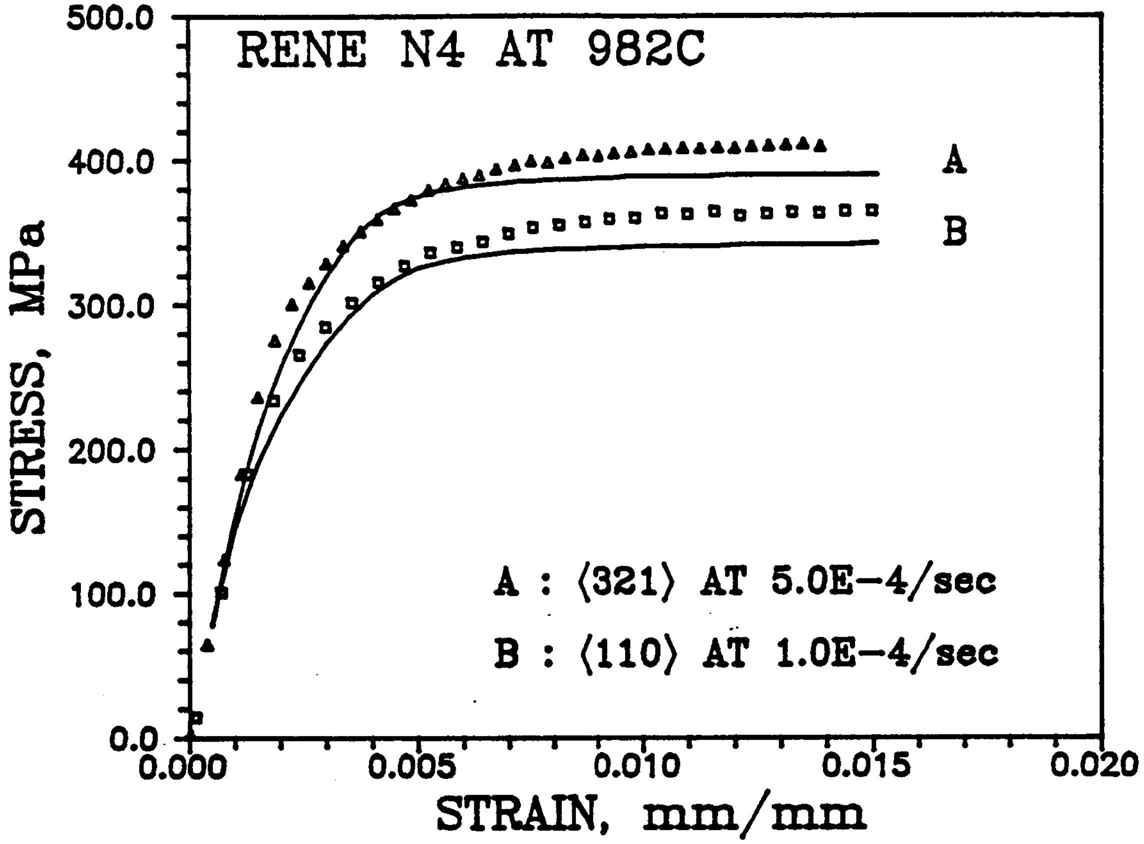

Figure 6-14 Comparison Between Experimental Data And Predicted Tensile Responses Of Rene N4 In The [110] And [321] Orientations At 980°C And Strain Rates Of 1.0×10^{-4}/sec And 5.0×10^{-4}/sec, Respectively.

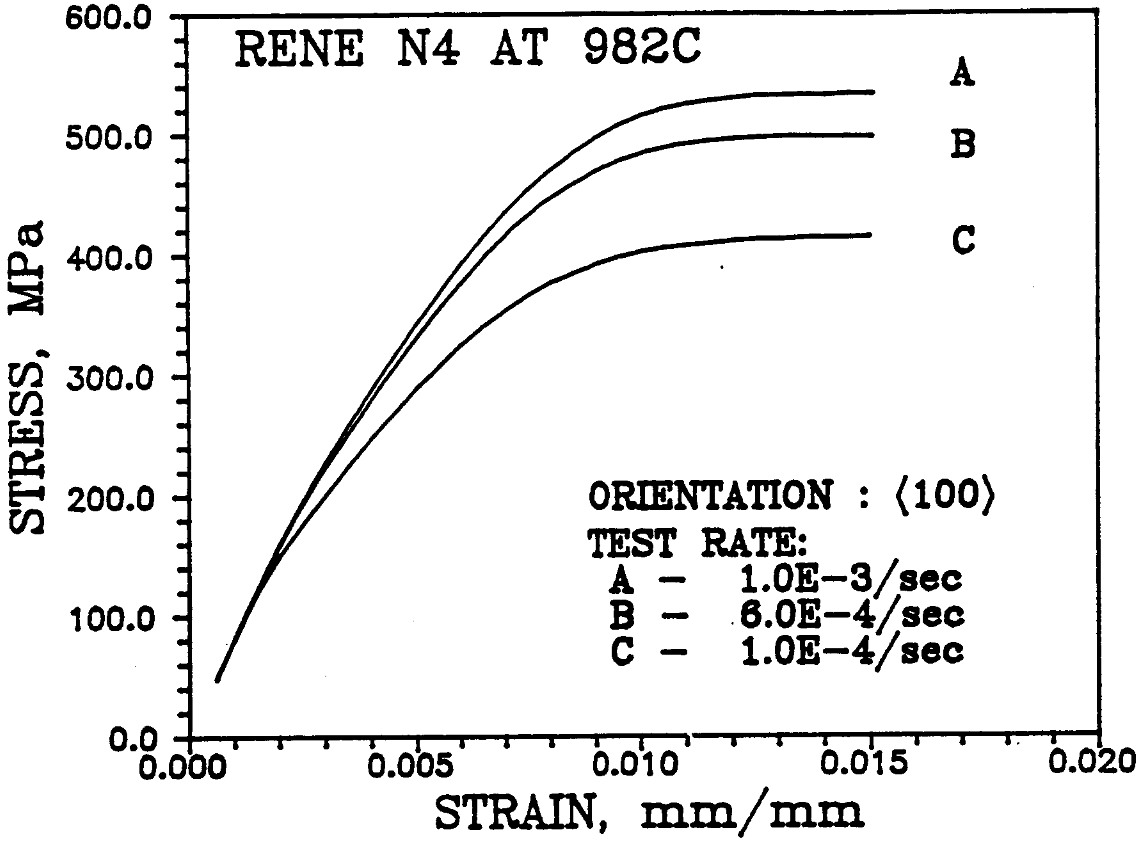

Figure 6-15 Predicted Tensile Responses of Rene N4 In The [100] Orientation At 980°C And Strain Rates Of 1×10^{-4}/sec, 6×10^{-4}/sec and 1×10^{-3}/sec

material behavior. Comparing Figures 6-2 and 6-15, the rate sensitivity is more pronounced at 982°C than at 760°C.

6.2.1.3 Anelastic Recovery

Comparison between model prediction and the experimental data for double tensile tests in the [100] and [111] orientations are shown in Figures 6-16 and 6-17, respectively. The hardening parameters were evaluated using tensile strain hardening and anelastic recovery data during the 120-second hold period in the double tensile test. The model predictions are considered successful from the following observations:

- The recovery during 120-second hold period in both orientations was correlated well (see Figure 6-18).
- The unloading portion for the [100] orientation exhibited Bauschinger effect before reaching zero stress level, which the model predicted.
- Strain hardening characteristic in the second loading loop was also satisfactorily modeled for each orientation.
- The saturated stress level in the second loading loop for each orientation was also correlated well.

A later analysis found that the recovery in the [111] orientation is primarily caused by the back stress in the octahedral slip systems rather than the back stress in the cube slip. This result is unexpected and has no experimental evidence to verify this finding.

6.2.2 Fatigue Calculations

Recall that the only information retrieved from fatigue data for determining material constants was the ratio between peak tensile stress and peak compressive stress of the fatigue test in the [100]

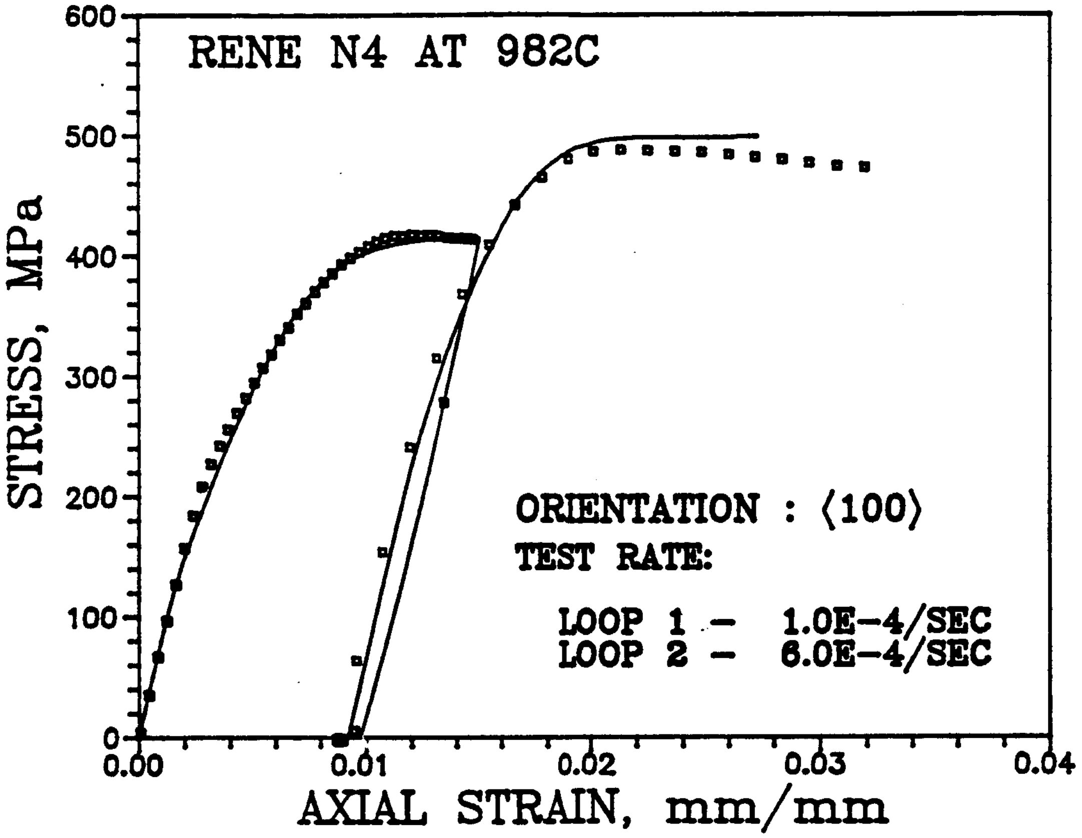

Figure 6-16 Comparison Between Experimental Data And Predicted Double Tensile Response Of Rene N4 In The [100] Orientation At 982°C

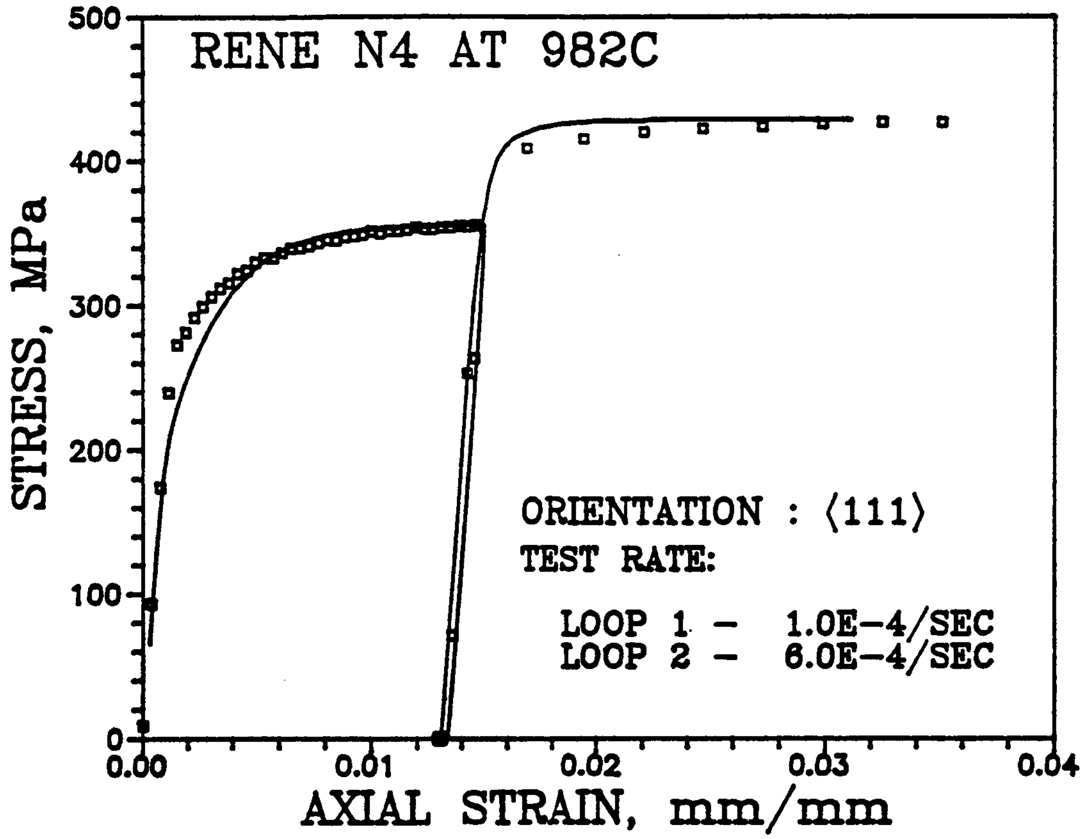

Figure 6-17 Comparison Between Experimental Data And Predicted Double Tensile Response Of Rene N4 In The [111] Orientation At 982°C

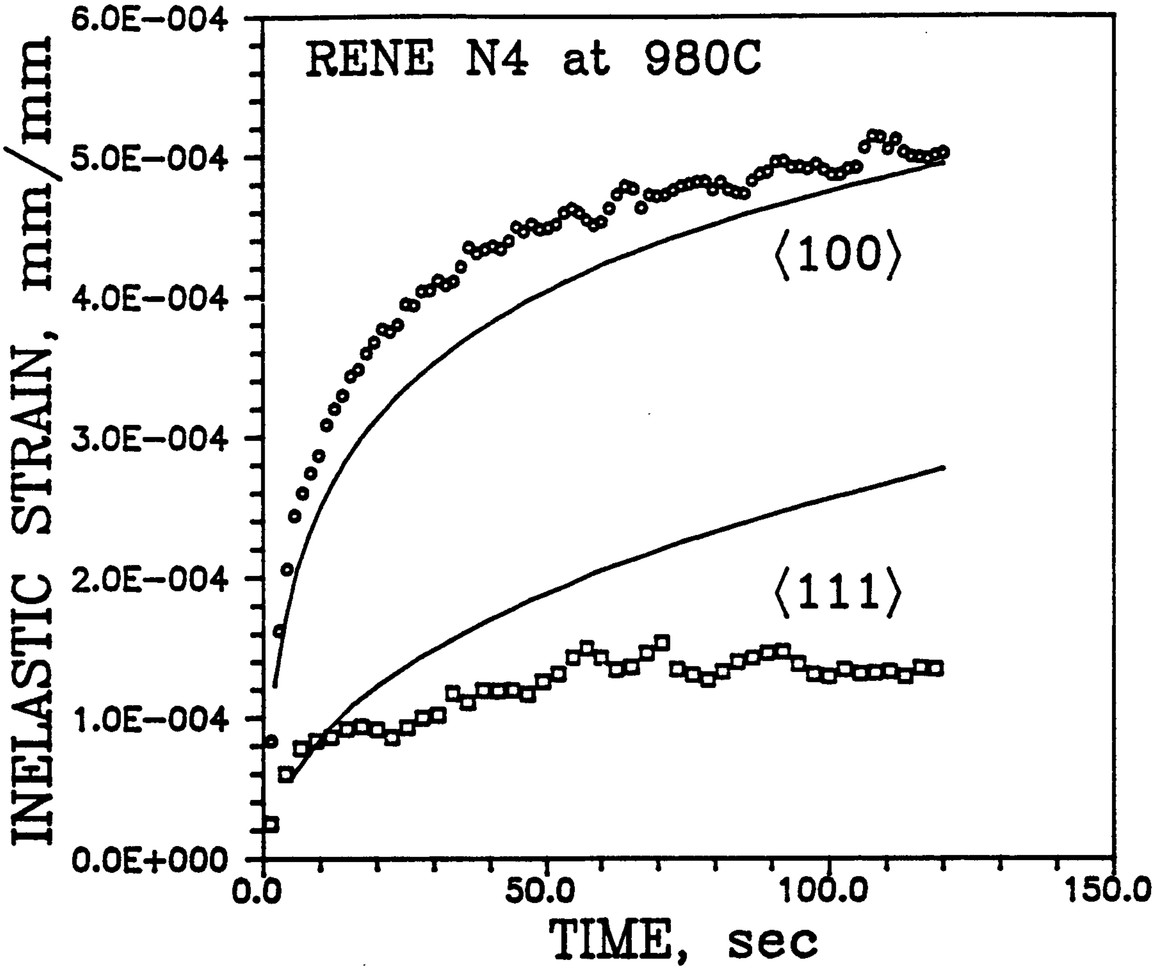

Figure 6-18 Comparison Between Predicted Anelastic Recovery And The Experimental Data In Double Tensile Test Of Rene N4 In The [100] and [111] Orientations At 982°C.

orientation. Other than this, the calculations shown in this section are model predictions by suing constants determined from the tensile tests. As explained earlier, because Rene N4 is cyclicly stable in this temperature regime, the hardening term for the drag stress are assumed unchanged.

6.2.2.1 Tension/compression Asymmetry

Comparisons between model predictions and the experimental data for cyclic tests in the [100], [111] and [123] orientations were shown in Figures 6-19, 6-20 and 6-21, respectively. These calculations were made under total strain control of ±0.3% and strain rate of 3×10^{-4}/sec for all orientations, except for the [100] orientation, which has a larger total strain range of ±0.85%. An additional fatigue calculation was made for the [110] orientation under the same control conditions. This result is shown in Figure 6-22.

The model appeared to predict these responses extremely well, for example; the shape of the stabilized loop, the hardening characteristics, and the tension/compression asymmetry in peak compressive and tensile stress. The model predicted a larger peak stress in the compressive side than in the tensile side for the [110] orientation, whereas, a reversed pattern was predicted for [100] orientation. Tension/compression asymmetry is insignificant for the [111] orientation and modest asymmetry was predicted for the [321] orientation. These calculations and experimental results were consistent with reported single crystal tension/compression asymmetry characteristics (see Figure 1-2).

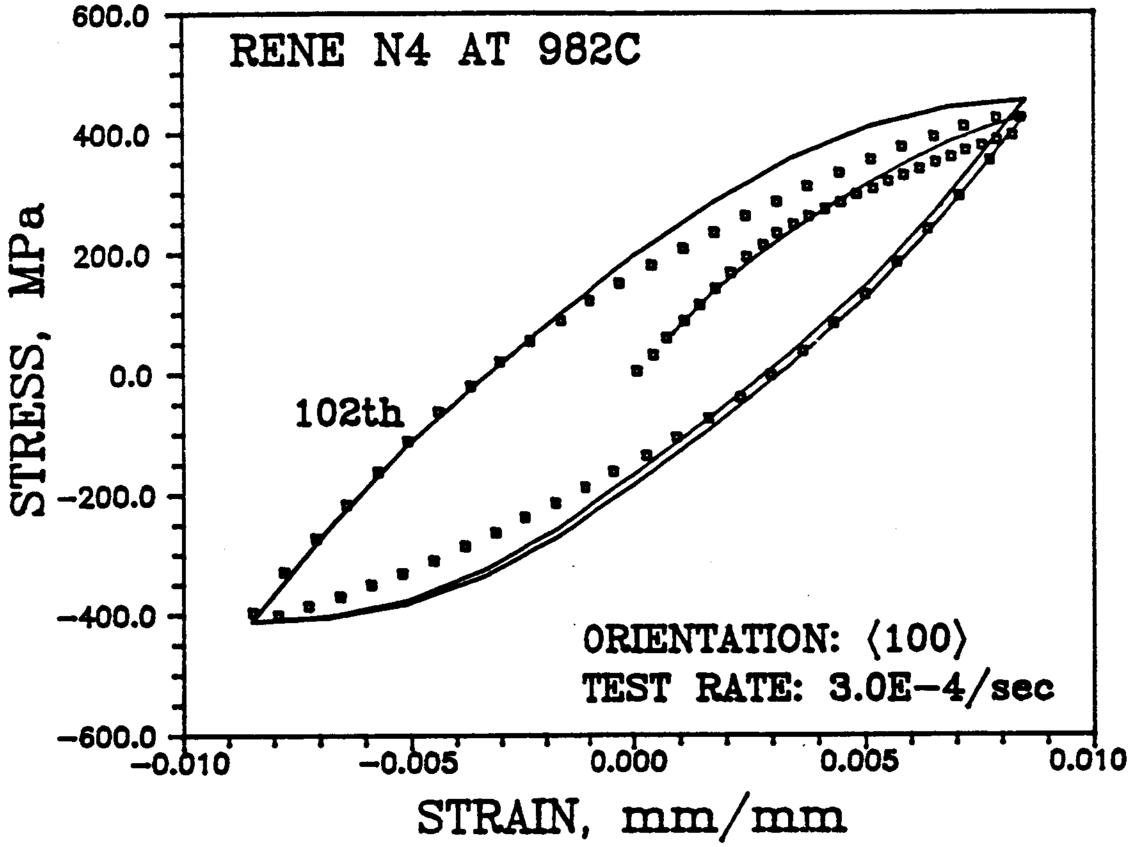

Figure 6-19 Comparison Between Experimental Data And Predicted Cyclic Response In The [100] Orientation For Rene N4 at 982°C

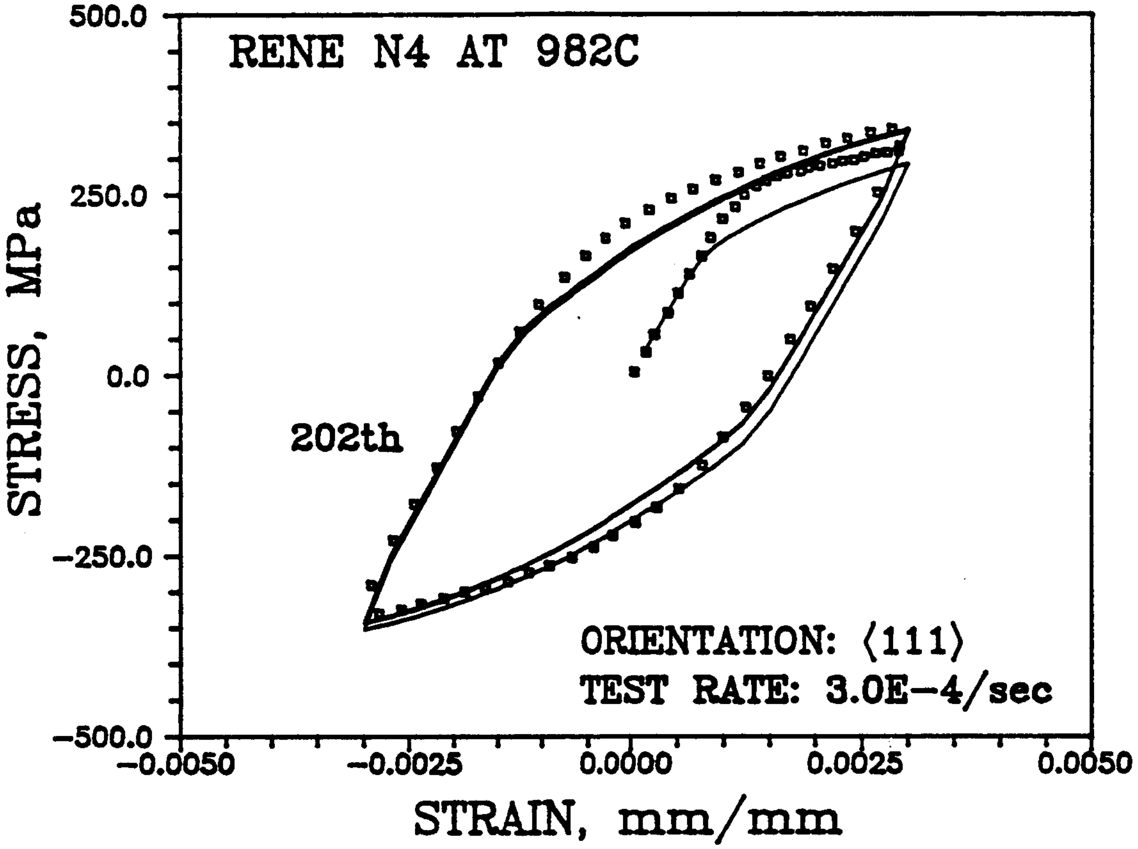

Figure 6-20 Comparison Between Experimental Data And Predicted Cyclic Response In The [111] Orientation For Rene N4 at 982°C

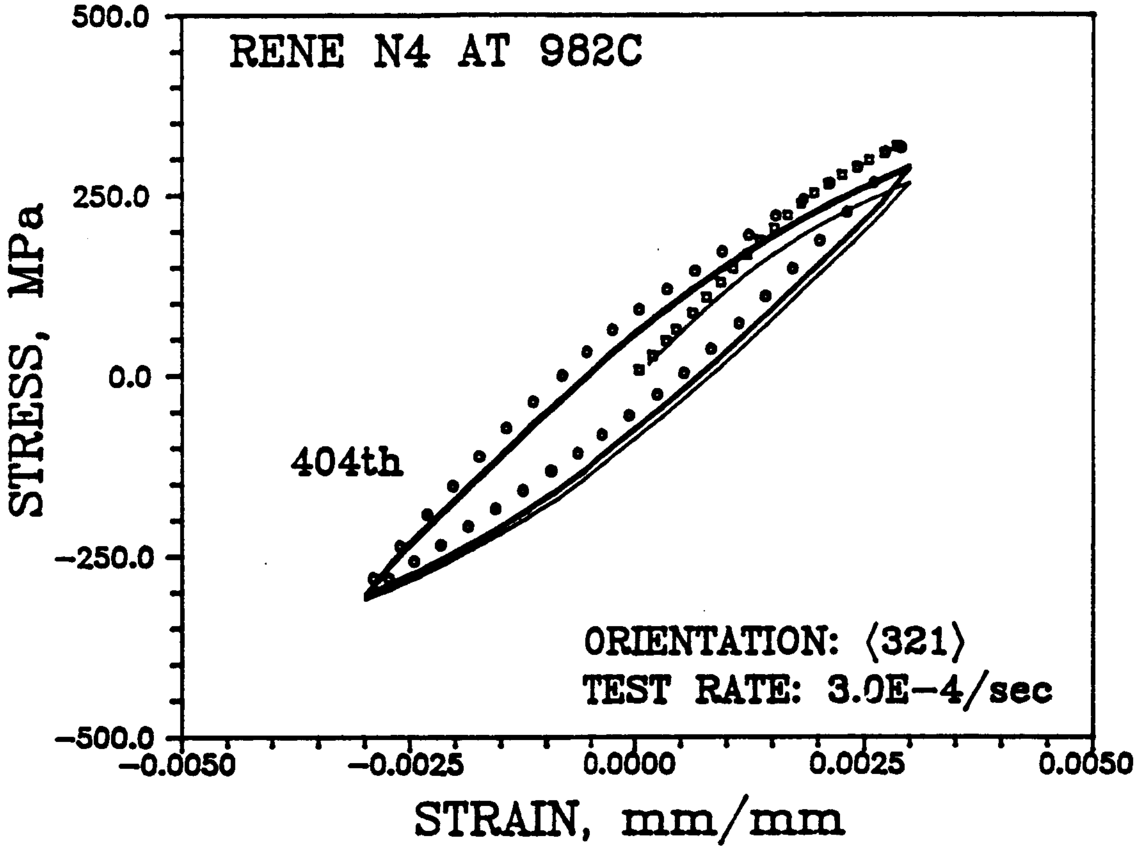

Figure 6-21 Comparison Between Experimental Data And Predicted Cyclic Response In The [321] Orientation For Rene N4 at 982°C

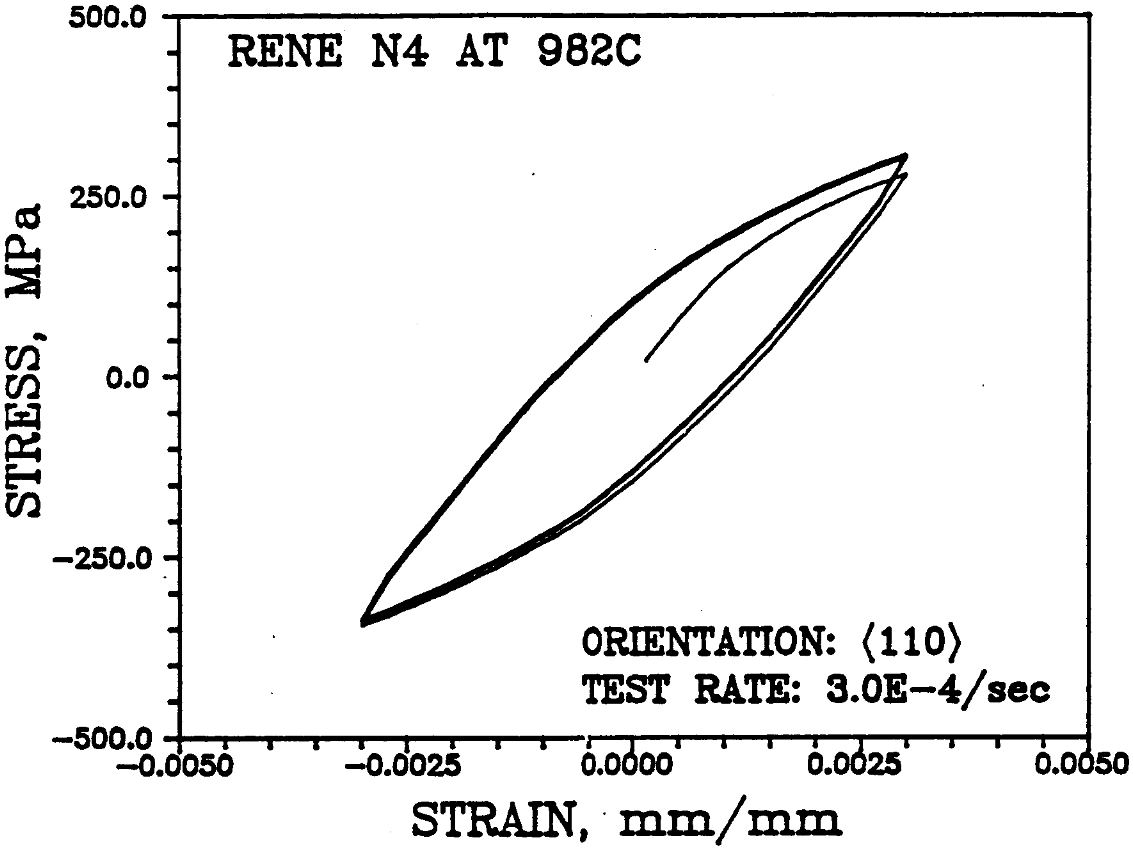

Figure 6-22 Predicted Cyclic Response In The [110] Orientation For Rene N4 At 982°C.

6.2.2.2 Stress Relaxation During Strain Hold Fatigue Test

The constitutive model was further tested using strain hold fatigue data. The test specification for strain hold fatigue tests are given in Table 5-1 (Chapter V). Comparison between model prediction and the experimental data for a compressive strain hold fatigue test in the [012] orientation is shown in Figure 6-23. The model successfully predicted the stress relaxation during the compressive strain-hold period. Also, the shape of the loop and the tension/compression asymmetry were both modeled well.

Comparison between model prediction and the experimental data for a tensile strain hold fatigue test in the [321] orientation is shown in Figure 6-24. The gradual softening of the material was not seen in all other fatigue tests. This softening behavior was suspected to be caused by increasing damage rate by tensile strain hold. The model predicted the stress relaxation in the first few loops well. However, it was impossible for the model to predict the softening behavior.

6.2.2.3 Cyclic Softening

Hypothetical values were assigned to H_{12} and m_{11} in Equation (4.23) to exercise the model for cyclic softening calculation. The result is shown in Figure 6-25 for the [100] orientation. The model prediction showed gradual cyclic softening of the material similar to the cyclic softening of Rene 80 and many other materials at elevated temperatures.

6.3 Comparison Between Dame and Stouffer's Model and the Current Model

Comparison between current model and Dame and Stouffer's model was made on qualitative basis because the two models were developed based on different physical background. For example, instead of using octahedral

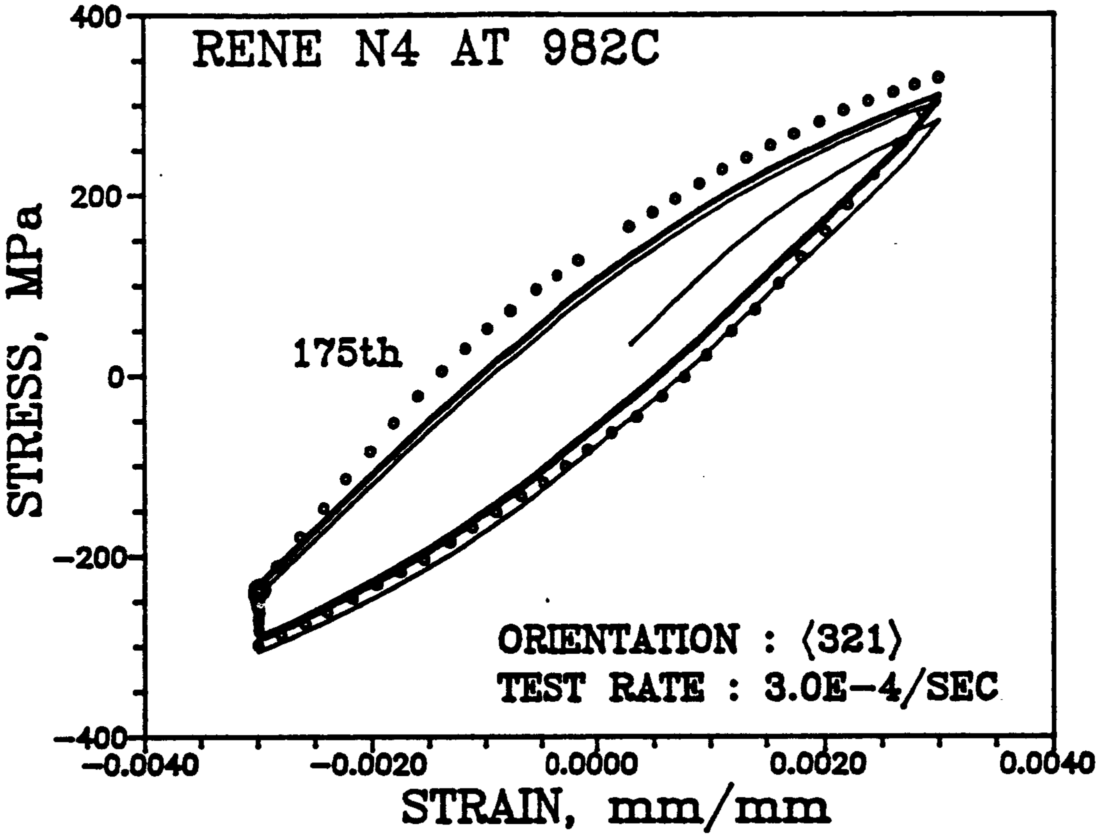

Figure 6-23 Comparison Between Experimental Data And Predicted Cyclic Response With Peak Compressive Strain Hold In The [321] Orientation For Rene N4 At 982°C.

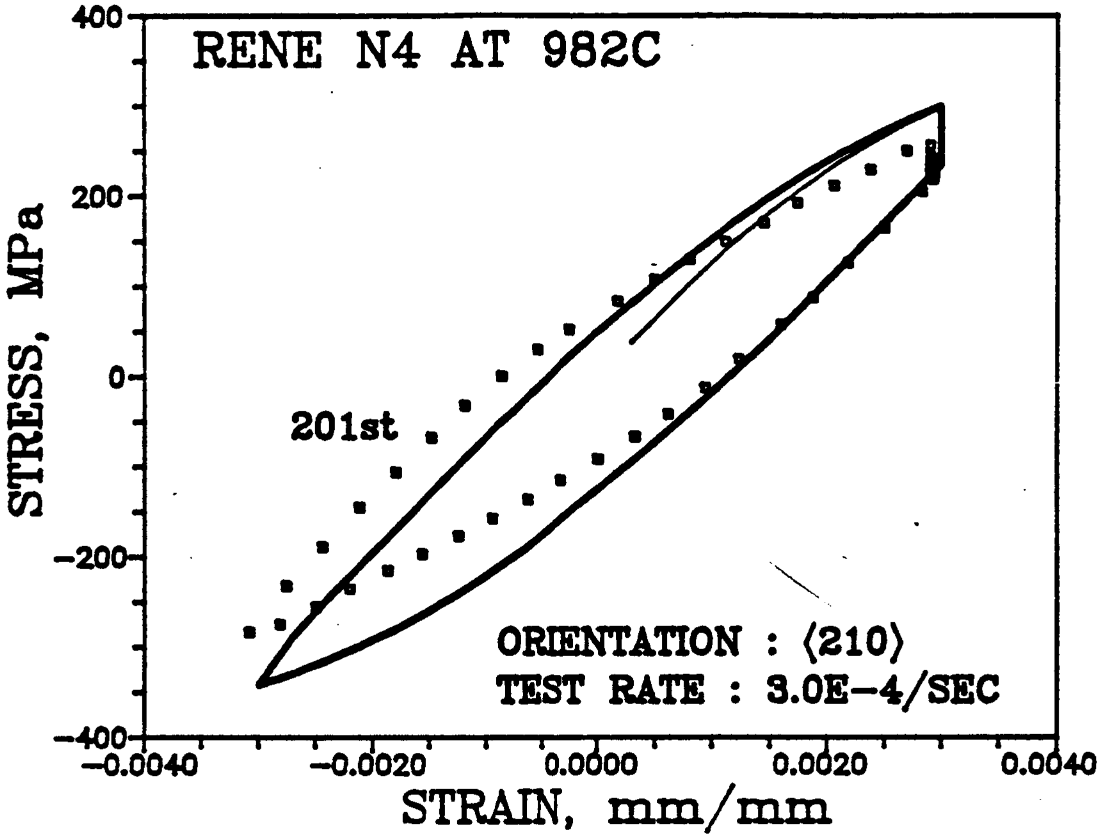

Figure 6-24 Comparison Between Experimental Data And Predicted Cyclic Response With Peak Tensile Strain Hold In The [210] Orientation For Rene N4 At 982°C.

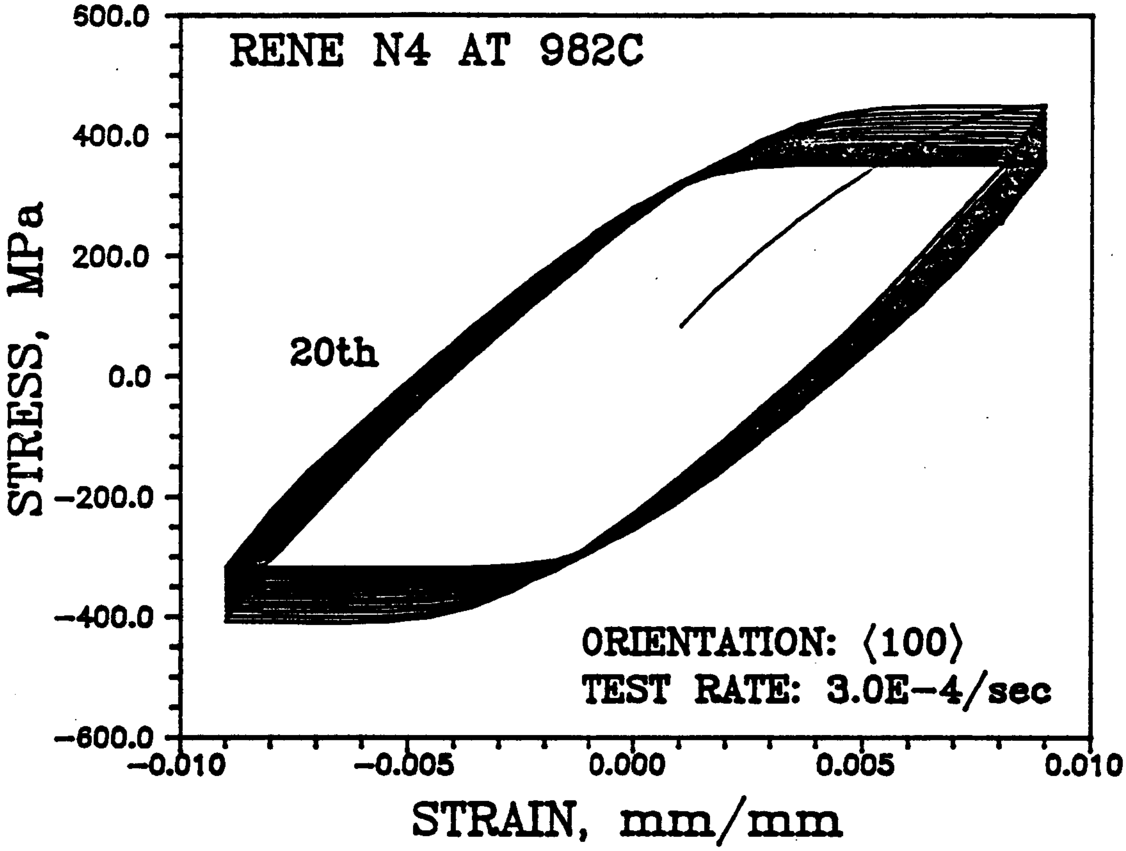

Figure 6-25 Predicted Cyclic Response In The [100] Orientation With Hypothetical Cyclic Hardening Parameters For Rene N4 At 982°C

<110> slip as in Dame and Stouffer's model, current model used octahedral <112> slip systems to calculate creep response.

The comparison between the two model are made from two aspect. That is the predictive capability and accuracy. These are discussed below for tensile, fatigue and creep calculations.

6.3.1 Tensile Calculation

Because of limited tensile data available, Dame and Stouffer's model was only exercised for tensile calculations in the [100], [110] and [310] orientations. The calculated responses in the [100] and [110] are comparable for both model. Similar mismatch of the [310] response also occurred in both model.

Dame and Stouffer's model satisfactorily predicted yield stresses in several orientations for Rene N4 using Minor et al's data (1986b). However, the ability to predict ultimate tensile strength (or saturated tensile stress) were not shown because of the lack of data. This ability is demonstrated by the current model for Rene N4 at 980°C (refer to Figure 6-15).

An important improvement made in this model is the ability to model the anelastic material behavior (Figures 6-16 through 6-18) which Dame and Stouffer's model was unable to predict. Other predictive capability, such as rate sensitivity and tensile-creep interaction, are expected to be similar for both models, although they were not demonstrated in Dame and Stouffer;s model

6.3.2 Fatigue Calculation

Because of fuzzy fatigue data were used by Dame and Stouffer's model, fatigue calculations did not match the experimental data well.

Thus, the accuracy of the fatigue calculation is not clear. The fatigue predictive capability of the current model is fully demonstrated for various sample orientations and loading conditions. The current model predicted these conditions very well.

6.3.3 Creep Calculation

Because both models used different active slip systems, the predictive capability and accuracy can not be compared directly. Dame and Stouffer's model used data from seven creep tests, and the predictions were very well. Current model was exercised by using data from three tests in the [100] orientation. Current model also utilized a set of kinematic rule to calculate the crystal lattice rotation.

It is still not clear whether all the single crystal alloys exhibit crystal lattice rotation during creep. Thus, studies on the creep deformation mechanism and the macroscopic mechanical response are needed.

CHAPTER VII

DISCUSSION AND SUMMARY OF THE CURRENT MODEL

The results presented in Chapter V show substantial improvements on the predictive capability of the current model over previous model (Dame and Stouffer, 1985). In particular, the predicted single crystal cyclic response, anelastic recovery, and the cyclic response with hold time were all greatly improved. The model also demonstrated the capability for calculating creep response associated with crystal lattice rotation. The success of the model can be attributed to two major reasons: first is the use of accurate deformation mechanisms and second the successful incorporation of the back stress state variables into the model. Early in this research, a significant effort was devoted to understanding the deformation mechanisms for the various loading conditions of single crystals and their relationship with the observed macroscopic material response. This work laid a strong physical basis for the model. Evaluation of the material parameters played the heavist role in this research. It involves formulation and modification of the equations, formulation of the test matrix and the design of special tests, generation of computational schemes for evaluating experimental data and determining material parameters, and the validation of these parameters. In this chapter, key elements in the development of the model are briefly reviewed. Limitation of the model and recommendation for future development are then discussed.

7.1 Constitutive Model Development

Development of the anisotropic constitutive model in this research can roughly be divided into two steps. In the first step, experiments were conducted to generate a data base for Rene N4 at 982°C. In addition to regular tensile tests, a double tensile test was designed to evaluate the existence of back stress. As described in Section 2.5, Chapter II, anelastic material response similar to back stress relaxation was observed for loading in the [100] orientation. This result motivated the incorporation of the back stress state variable into the model. Evolution equations were formulated (Chapter III) based on Ramaswamy's model for Rene 80. Because local slip is unidirectional, the back stress in the current model has a scalar form rather than tensorial form.

Macroscopic material properties and the corresponding deformation mechanisms for various single crystal alloys under high and low strain rates were thoroughly studied. This review established the physical basis for the model. The result indicated the high strain rate single crystal response was primarily due to octahedral a/2<110>{111} slip and cube a/2<110>{100} slip systems. The active slip system depends on temperature, strain rate and the loading direction relative to the material principal axes. Low strain rate single crystal deformation is primarily resulted from slip in the directions similar to <112> on the octahedral planes. Thus, three separate flow equations, one for each slip system, was required to model the inelastic flow in each slip system. The corresponding kinematic equations for each slip system were then developed.

In the second step, evolution equations for the state variables were formulated. A significant amount of work was then focused on establishing a procedure for evaluating material parameters. At the same time, refinements of the evolution equations were also made based on the experimental data and literature review. Parameter evaluation procedure was developed and could be divided into four parts: e.g., i) evaluation of flow equation constants; ii) evaluation of back stress parameters; iii) evaluation of drag stress parameters; and iv) evaluation of creep parameters. As described in Chapter V, this evaluation procedure is conducted sequentially for the first two steps. The order for the last two steps can be reversed. Several key elements in this procedure are summarized below.

- This evaluation procedure requires an initial estimate of the rate sensitivity exponent, n_{11}, in the inelastic flow equation. Other material constants are then evaluated. Parameter n_{11} could be optimized if experimental data similar to the double tensile test are available. This has been discussed in Chapter V.
- Depending upon the available data, three approaches could be used for evaluating the back stress parameters. It has been demonstrated in Chapter V that double tensile test provides more information about the material properties including the strain hardening characteristics, anelastic recovery behavior, strain rate sensitivity, and possibly the static thermal recovery. This information could play a dominant role in determining the material constants and the model predictive capability. The current model took advantage of the double-tensile test data and have made successful predictions on complex material responses such as cyclic test with hold time (see Figures 6.18, 6.21, 6.23, and 6.24).
- Drag stress in the current model incorporated the resolved shear stress on a secondary slip plane to better characterize the tension/compression asymmetry behavior. The predicted results

were in better agreement with the experimental data (see Figures 6.5, 6.6, 6.14, 6.19-6.24) than the previous model.

- An optimization process is available for back stress parameters using double tensile test data. This method also helps to obtained a better estimate of the strain rate sensitivity exponent n_{11} as described in Section 5.2.3, Chapter V.
- The Crystal lattice rotation kinematics was also established in this research. A Preliminary investigation on the rotation and primary creep strain was made for tensile loading. Because of lattice rotation, the primary creep strain could be as high as 10-15%. This calculation was made based on the assumptions that lattice rotation occur only for orientations that exhibit single glide and the rate of rotation is a function of local inelastic work rate (Equation 4.39). To date, no experimental data is available to evaluate the relationship between rate of lattice rotation and the inelastic strain rate.
- Crystal lattice rotation was evaluated only for tensile creep conditions. How the crystal lattice rotates under multiaxial loading conditions is not clear.

7.2 Data Base Requirements

For the single crystal constitutive model to be used in a nonlinear finite element code, it is necessary to develop the data base for evaluating the material parameters. In addition, it is necessary to evaluate the model at other temperatures. Inelastic behavior for turbine blades and vanes during operation mostly occurs at temperatures between 600°C to about 1000°C. The test data for the inelastic response of the material should therefore be acquired in this temperature range.

Considering the variation in response with temperature, it is desirable to obtain data at about 100°C intervals. A test matrix at a single temperature is presented in Table 7.1 The test matrix is based on the ideal tests required to determine the material parameters as discussed in Chapter V. The data base must be chosen to activate the octahedral and cube slip systems separately. Thus, most tests should be conducted in the [100] and [111] orientations. Tests in the [110] direction are also necessary, because the tension/compression asymmetry is significant. Tests should also be conducted in other orientations to verify the model. It is not expected that the full test matrix should be run at all temperatures; however, the full matrix should be run at least one temperature above and below the critical temperature, about 800°C, since the deformation mechanisms appear to be different.

7.3 Limitation and Recommendation

Because the material parameters for the current model were evaluated using data from the same temperature, the variation of material parameters with temperature was is known. The model has only been used for isothermal calculations. However, a method for non-isothermal prediction has been suggested by Bodner (1979) for isotropic material and has been successfully used by Ramaswamy (1985) on Rene 80. This method may be successful for Rene N4 because Rene 80 and Rene N4 are almost identical in composition.

Cyclic hardening and softening for Rene N4 was not evaluated for various total strain range. In the current research, both 760°C and 982°C data exhibited cyclicly stable material response. Although the model has demonstrated the capability for modeling cyclic softening or hardening, the actual material responses under different loading

Table 7-1 Data Base Requirement for Determining Material Constants In The Current Model.

TEST TYPE	ORIENTATION	TEST*	STRAIN RATE	STRESS LEVEL
CONST. STRAIN RATE	[100]	DT	2	-
CONST. STRAIN RATE	[100]	C	1	-
CONST. STRAIN RATE	[110]	T	1	-
CONST. STRAIN RATE	[110]	C	1	-
CONST. STRAIN RATE	[111]	DT	2	-
CONST. STRAIN RATE	[100]	F	1	-
CONST. STRAIN RATE	[111]	F	1	-
CONST. LOAD	[100]	T	-	2
CONST. LOAD	[100]	C	-	2
CONST. LOAD	[111]	T	-	1
CONST. LOAD	[111]	C	-	1
	VERIFICATION TESTS			

* T : Tensile test
C : Compressive test
DT : Double tensile test
F : Fatigue test

conditions; for example, a greater total strain range, may not be cyclic stable. Further refinement on the drag stress evolution equation may be required.

Crystal lattice rotation predictions were based on hypothetical material parameters. Thus, they may not be appropriate for actual material response. Further, tertiary creep can not be predicted by the current model. A approach similar to isotropic material could be used to model tertiary creep for single crystal alloys by incorporating a damage state variable and evolution equation. This may be necessary for the model to predict the gradual softening observed for the tensile strain hold fatigue test.

Future work should be aimed to better understand the relationship between crystal lattice rotation and inelastic slip rate for monotonic creep condition and other low strain rate loading conditions. Multiaxial data base is also required to establish for further investigation of the mechanical properties of the single crystal and the verification of the constitutive model.

Static thermal recovery was not considered in this model. However, it was suspected to be present; for example, during the zero stress hold period in the double tensile test. Nearly all of the recently developed unified constitutive models include a hardening term and a recovery term in the work hardening state variable evolution equations. This form has been successful in modeling the inelastic response of many isotropic metals. In this research, an adequate data base for evaluating a recovery term was not available and the term was not included. Future investigation in this aspect is important to formulate a better state variable evolution equation.

In this research, a material parameter evaluation procedure was developed. Optimization of the parameters was performed in each step of the procedure. However, there is a need for a global optimization scheme for practical application of the model. Particularly, if the model is to be implemented into nonlinear finite element code for structural analysis.

Finally, latent hardening, e.g., the hardening of inactive slip system due to intersection with active slip system, was not considered in the current model. However, latent hardening is generally considered to be an important part of the theoretical basis for hardening in single crystal plasticity (Asaro, 1983; Havner and co-worker, 1977 and 1983; Weng, 1979). For small strains and proportional loading, latent hardening will have little or no effect on the materials response or the predictive capability of the constitutive model. For nonproportional loading or large strains the effect of latent hardening for Rene N4 is probably important but cannot be investigated with the current data base. Extension of the present theory to large strains and/or nonproportional loading may require consideration of latent hardening effects.

APPENDIX A

DEVELOPMENT OF THE KINEMATIC EQUATIONS

This appendix contains explicit representations for the local and global stress and inelastic strain rate components.

A.1 Octahedral a/2<110>{111} Slip Systems

The sign convention for positive slip directions on the {111} octahedral planes are shown in Figure A-1. The positive unit normals to the four octahedral planes are given by:

$$\bar{n}^1 = 1/\sqrt{3}\ (\bar{i} + \bar{j} + \bar{k}) \qquad \bar{n}^2 = 1/\sqrt{3}\ (-\bar{i} + \bar{j} - \bar{k})$$

$$\bar{n}^3 = 1/\sqrt{3}\ (\bar{i} - \bar{j} - \bar{k}) \qquad \bar{n}^4 = 1/\sqrt{3}\ (-\bar{i} - \bar{j} + \bar{k}) \tag{A.1}$$

where $\bar{i}$, $\bar{j}$, and $\bar{k}$ are the unit vectors in the principal material directions. The positive sign convention for the <110> directions on the octahedral planes are:

$$\bar{\ell}^{11} = 1/\sqrt{2}\ (\bar{i} - \bar{k}) \qquad \bar{\ell}^{12} = 1/\sqrt{2}\ (-\bar{j} + \bar{k})$$

$$\bar{\ell}^{13} = 1/\sqrt{2}\ (\bar{i} - \bar{j}) \qquad \bar{\ell}^{21} = 1/\sqrt{2}\ (\bar{i} - \bar{k})$$

$$\bar{\ell}^{22} = 1/\sqrt{2}\ (\bar{i} + \bar{j}) \qquad \bar{\ell}^{23} = 1/\sqrt{2}\ (\bar{j} + \bar{k})$$

$$\bar{\ell}^{31} = 1/\sqrt{2}\ (\bar{i} + \bar{j}) \qquad \bar{\ell}^{32} = 1/\sqrt{2}\ (-\bar{j} + \bar{k})$$

$$\bar{\ell}^{33} = 1/\sqrt{2}\ (\bar{i} + \bar{k}) \qquad \bar{\ell}^{41} = 1/\sqrt{2}\ (\bar{j} + \bar{k})$$

$$\bar{\ell}^{42} = 1/\sqrt{2}\ (\bar{i} + \bar{k}) \qquad \bar{\ell}^{43} = 1/\sqrt{2}\ (\bar{i} - \bar{j}) \tag{A.2}$$

Substituting Equations (A.1) and (A.2) into Equation (4.3), e.g.,

$$\tau^{\alpha\beta} = \sum_{ij} \sigma_{ij}\, n_i^{\alpha}\, \ell_j^{\alpha\beta} \tag{4.3}$$

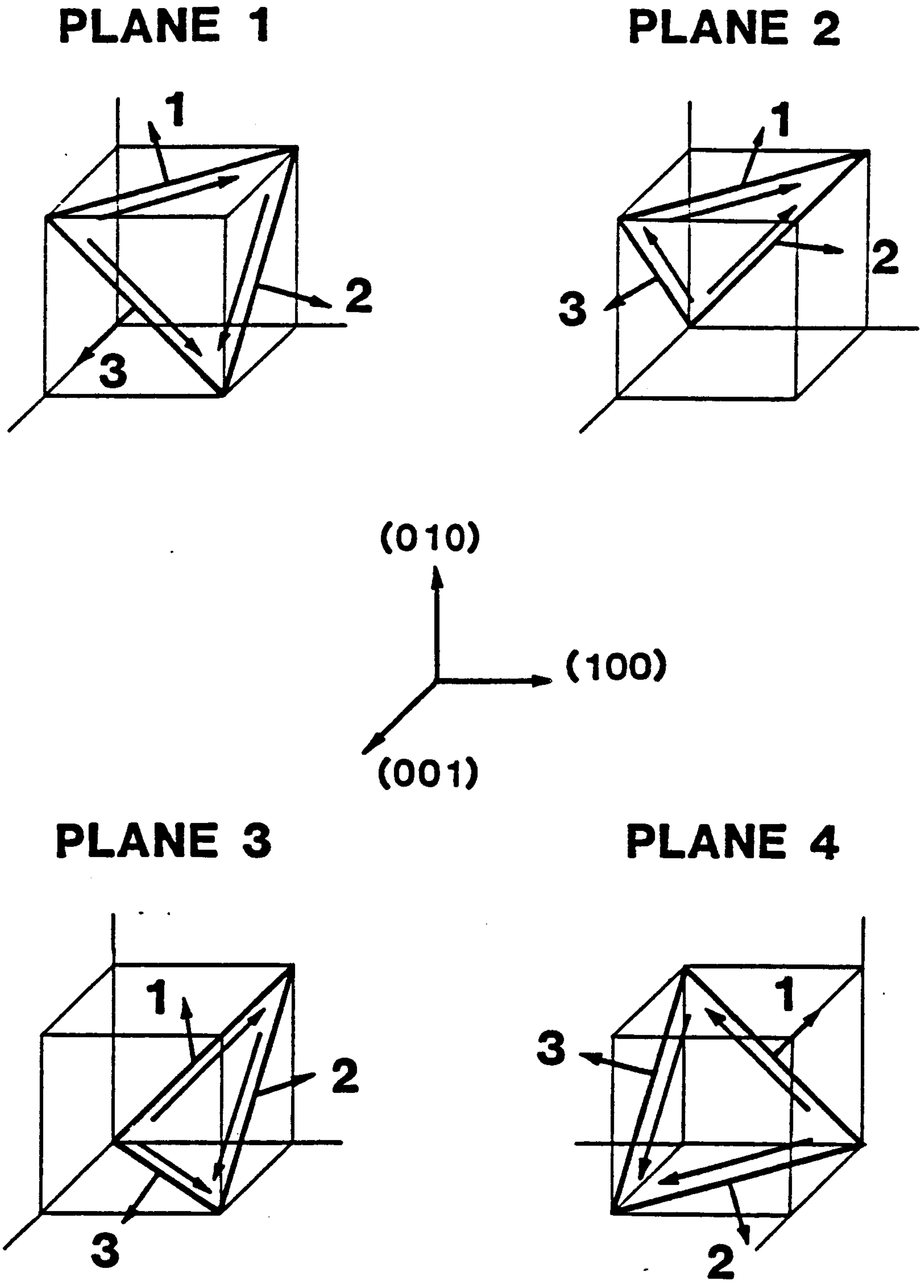
PLANE 1
1
2
3
PLANE 2
1
2
3
(010)
(100)
(001)
PLANE 3
1
2
3
PLANE 4
1
3
2

Figure A-1 Octahedral a/2<110> and a/2(112> slip systems.

gives the shear stress in each of the <110> directions on the octahedral planes as:

$$\begin{bmatrix} \tau^{11} \\ \tau^{12} \\ \tau^{13} \\ \tau^{23} \\ \tau^{22} \\ \tau^{23} \\ \tau^{31} \\ \tau^{32} \\ \tau^{33} \\ \tau^{41} \\ \tau^{42} \\ \tau^{43} \end{bmatrix} = \frac{1}{\sqrt{6}} \begin{bmatrix} 1 & 0 & -1 & 1 & 0 & -1 \\ 0 & -1 & 1 & -1 & 1 & 0 \\ 1 & -1 & 0 & 0 & 1 & -1 \\ -1 & 0 & 1 & 1 & 0 & -1 \\ -1 & 1 & 0 & 0 & -1 & -1 \\ 0 & 1 & -1 & -1 & -1 & 0 \\ 1 & -1 & 0 & 0 & -1 & -1 \\ 0 & 1 & -1 & -1 & 1 & 0 \\ 1 & 0 & -1 & -1 & 0 & -1 \\ 0 & -1 & 1 & -1 & -1 & 0 \\ -1 & 0 & 1 & -1 & 0 & -1 \\ -1 & 1 & 0 & 0 & 1 & -1 \end{bmatrix} \begin{bmatrix} \sigma_{11} \\ \sigma_{22} \\ \sigma_{33} \\ \sigma_{12} \\ \sigma_{13} \\ \sigma_{23} \end{bmatrix} \qquad \text{(A.3)}$$

The stresses σ_{ij} are relative to the material principal axes.

Substituting Equations (A.1) and (A.2) into Equation (4.6), e.g.,

$$\dot{\epsilon}_{ij} = \sum_{\alpha\beta} \frac{1}{2} \dot{\gamma}^{\alpha\beta} (\ell_i^{\alpha\beta} n_j^{\alpha} + \ell_j^{\alpha\beta} n_i^{\alpha}) \quad . \qquad \text{(4.6)}$$

gives the inelastic strain rate tensor, relative to the material principal axes, resulted from shearing in the <110> directions on the octahedral planes. That is:

$$
\begin{aligned}
&\begin{bmatrix} \dot{\epsilon}^{I}_{11} & \dot{\epsilon}^{I}_{12} & \dot{\epsilon}^{I}_{13} \\ \dot{\epsilon}^{I}_{21} & \dot{\epsilon}^{I}_{22} & \dot{\epsilon}^{I}_{23} \\ \dot{\epsilon}^{I}_{31} & \dot{\epsilon}^{I}_{32} & \dot{\epsilon}^{I}_{33} \end{bmatrix}_{\mathrm{OCT}_1} = \sqrt{6}/12 \times \Bigg\{ \\
&\dot{\gamma}^{11}_{\mathrm{OCT}^1} \begin{bmatrix} 2 & 1 & 0 \\ 1 & 0 & -1 \\ 0 & -1 & -2 \end{bmatrix} + \dot{\gamma}^{12}_{\mathrm{OCT}^1} \begin{bmatrix} 0 & -1 & 1 \\ -1 & -2 & 0 \\ 1 & 0 & 2 \end{bmatrix} + \dot{\gamma}^{13}_{\mathrm{OCT}^1} \begin{bmatrix} 2 & 0 & 1 \\ 0 & -2 & -1 \\ 1 & -1 & 0 \end{bmatrix} + \\
&\dot{\gamma}^{21}_{\mathrm{OCT}^1} \begin{bmatrix} -2 & 1 & 0 \\ 1 & 0 & -1 \\ 0 & -1 & 2 \end{bmatrix} + \dot{\gamma}^{22}_{\mathrm{OCT}^1} \begin{bmatrix} -2 & 0 & -1 \\ 0 & -2 & -1 \\ -1 & -1 & 0 \end{bmatrix} + \dot{\gamma}^{23}_{\mathrm{OCT}^1} \begin{bmatrix} 0 & -1 & -1 \\ -1 & 2 & 0 \\ -1 & 0 & -2 \end{bmatrix} + \\
&\dot{\gamma}^{31}_{\mathrm{OCT}^1} \begin{bmatrix} 2 & 0 & -1 \\ 0 & -2 & -1 \\ -1 & -1 & 0 \end{bmatrix} + \dot{\gamma}^{32}_{\mathrm{OCT}^1} \begin{bmatrix} 0 & -1 & 1 \\ -1 & 2 & 0 \\ 1 & 0 & -2 \end{bmatrix} + \dot{\gamma}^{33}_{\mathrm{OCT}^1} \begin{bmatrix} 2 & -1 & 0 \\ -1 & 0 & -1 \\ 0 & -1 & -2 \end{bmatrix} + \\
&\dot{\gamma}^{41}_{\mathrm{OCT}^1} \begin{bmatrix} 0 & -1 & -1 \\ -1 & -2 & 0 \\ -1 & 0 & 2 \end{bmatrix} + \dot{\gamma}^{42}_{\mathrm{OCT}^1} \begin{bmatrix} -2 & -1 & 0 \\ -1 & 0 & -1 \\ 0 & -1 & 2 \end{bmatrix} + \dot{\gamma}^{43}_{\mathrm{OCT}^1} \begin{bmatrix} -2 & 0 & 1 \\ 0 & 2 & -1 \\ 1 & -1 & 0 \end{bmatrix} \Bigg\}
\end{aligned}
\tag{A.4}
$$

A.2 Octahedral a/2<112>{111} Slip Systems

The sign convention and the plane normals for positive slip directions on the {111} octahedral planes are shown in Figure A-1 and Equation (A.1), respectively. The positive sign convention for the <112> directions on the octahedral planes are:

$$\bar{\ell}^{11} = 1/\sqrt{6}\,(-\bar{i} + 2\bar{j} - \bar{k})$$

$$\bar{\ell}^{12} = 1/\sqrt{6}\,(2\bar{i} - \bar{j} - \bar{k})$$

$$\bar{\ell}^{13} = 1/\sqrt{6}\,(-\bar{i} - \bar{j} + 2\bar{k})$$

$$\bar{\ell}^{21} = 1/\sqrt{6}\,(\bar{i} + 2\bar{j} + \bar{k})$$

$$\bar{\ell}^{22} = 1/\sqrt{6}\,(\bar{i} - \bar{j} - 2\bar{k})$$

$$\bar{\ell}^{23} = 1/\sqrt{6}\,(-2\bar{i} - \bar{j} + \bar{k})$$

$$\bar{\ell}^{31} = 1/\sqrt{6}\,(-\bar{i} + \bar{j} - 2\bar{k})$$

$$\bar{\ell}^{32} = 1/\sqrt{6}\,(2\bar{i} + \bar{j} + \bar{k})$$

$$\bar{\ell}^{33} = 1/\sqrt{6}\,(-\bar{i} - 2\bar{j} + \bar{k})$$

$$\bar{\ell}^{41} = 1/\sqrt{6}\,(-2\bar{i} + \bar{j} - \bar{k})$$

$$\bar{\ell}^{42} = 1/\sqrt{6}\,(\bar{i} - 2\bar{j} - \bar{k})$$

$$\bar{\ell}^{43} = 1/\sqrt{6}\,(\bar{i} + \bar{j} + 2\bar{k}) \tag{A.5}$$

Substituting Equations (A.1) and (A.5) into Equation (4.3) in Chapter IV gives the shear stress in each of the <112> directions on the octahedral planes as:

$$\begin{bmatrix} \tau^{11} \\ \tau^{12} \\ \tau^{13} \\ \tau^{21} \\ \tau^{22} \\ \tau^{23} \\ \tau^{31} \\ \tau^{32} \\ \tau^{33} \\ \tau^{41} \\ \tau^{42} \\ \tau^{43} \end{bmatrix} = \begin{bmatrix} -1 & 2 & -1 & 1 & -2 & 1 \\ 2 & -1 & -1 & 1 & 1 & -2 \\ -1 & -1 & 2 & -2 & 1 & 1 \\ -1 & 2 & -1 & -1 & -2 & -1 \\ -1 & -1 & 2 & 2 & 1 & -1 \\ 2 & -1 & -1 & -1 & 1 & 2 \\ -1 & -1 & 2 & 2 & -1 & 1 \\ 2 & -1 & -1 & -1 & -1 & -2 \\ -1 & 2 & -1 & -1 & 2 & 1 \\ 2 & -1 & -1 & 1 & -1 & 2 \\ -1 & 2 & -1 & 1 & 2 & -1 \\ -1 & -1 & 2 & -2 & -1 & -1 \end{bmatrix} \begin{bmatrix} \sigma_{11} \\ \sigma_{22} \\ \sigma_{33} \\ \sigma_{12} \\ \sigma_{13} \\ \sigma_{23} \end{bmatrix} . \qquad (A.6)$$

These components influence the orientation dependent yield and tension/compression asymmetry for octahedral slip through the core width effect.

Substituting Equations (A.1) and (A.5) into Equation (4.6) gives the inelastic strain rate tensor, relative to the material principal axes, caused by shearing in the <112> directions on the octahedral planes. That is:

$$
\begin{aligned}
\begin{bmatrix} \dot{\epsilon}^{I}_{11} & \dot{\epsilon}^{I}_{12} & \dot{\epsilon}^{I}_{13} \\ \dot{\epsilon}^{I}_{21} & \dot{\epsilon}^{I}_{22} & \dot{\epsilon}^{I}_{23} \\ \dot{\epsilon}^{I}_{31} & \dot{\epsilon}^{I}_{32} & \dot{\epsilon}^{I}_{33} \end{bmatrix}_{\text{OCT}_2} = \sqrt{6}/12 \times \Bigg\{ \\
\dot{\gamma}^{11}_{\text{OCT}^2} \begin{bmatrix} -2 & 1 & -2 \\ 1 & 4 & 1 \\ -2 & 1 & -2 \end{bmatrix} + \dot{\gamma}^{12}_{\text{OCT}^2} \begin{bmatrix} 4 & 1 & 1 \\ 1 & -2 & -2 \\ 1 & -2 & -2 \end{bmatrix} + \dot{\gamma}^{13}_{\text{OCT}^2} \begin{bmatrix} -2 & -2 & 1 \\ -2 & -2 & 1 \\ 1 & 1 & 4 \end{bmatrix} + \\
\dot{\gamma}^{21}_{\text{OCT}^2} \begin{bmatrix} -2 & -1 & -2 \\ -1 & 4 & -1 \\ -2 & -1 & -2 \end{bmatrix} + \dot{\gamma}^{22}_{\text{OCT}^2} \begin{bmatrix} -2 & 2 & 1 \\ 2 & -2 & -1 \\ 1 & -1 & 4 \end{bmatrix} + \dot{\gamma}^{23}_{\text{OCT}^2} \begin{bmatrix} 4 & -1 & 1 \\ -1 & -2 & 2 \\ 1 & 2 & -2 \end{bmatrix} + \\
\dot{\gamma}^{31}_{\text{OCT}^2} \begin{bmatrix} -2 & 2 & -1 \\ 2 & -2 & 1 \\ -1 & 1 & 4 \end{bmatrix} + \dot{\gamma}^{32}_{\text{OCT}^2} \begin{bmatrix} 4 & -1 & -1 \\ -1 & -2 & -2 \\ -1 & -2 & -2 \end{bmatrix} + \dot{\gamma}^{33}_{\text{OCT}^2} \begin{bmatrix} -2 & -1 & 2 \\ -1 & 4 & 1 \\ 2 & 1 & -2 \end{bmatrix} + \\
\dot{\gamma}^{41}_{\text{OCT}^2} \begin{bmatrix} 4 & 1 & -1 \\ 1 & -2 & 2 \\ -1 & 2 & -2 \end{bmatrix} + \dot{\gamma}^{42}_{\text{OCT}^2} \begin{bmatrix} -2 & 1 & 2 \\ 1 & 4 & -1 \\ 2 & -1 & -2 \end{bmatrix} + \dot{\gamma}^{43}_{\text{OCT}^2} \begin{bmatrix} -2 & -2 & -1 \\ -2 & -2 & -1 \\ -1 & -1 & 4 \end{bmatrix} \Bigg\} \quad \text{(A.7)}
\end{aligned}
$$

A.3 Cube a/2<110>{100} Slip Systems

The sign convention for positive slip directions on the {100} cube planes are shown in Figure A-2. The positive unit normals are given by:

$$\bar{n}^1 = \bar{i}$$

$$\bar{n}^2 = \bar{j}$$

$$\bar{n}^3 = \bar{k} \tag{A.9}$$

The sign convention for positive slip directions on the cube planes are:

$$\ell^{11} = 1/\sqrt{2}\ (\bar{j} + \bar{k}) \qquad \ell^{12} = 1/\sqrt{2}\ (\ \bar{j} - \bar{k})$$

$$\ell^{21} = 1/\sqrt{2}\ (\bar{i} + \bar{k}) \qquad \ell^{22} = 1/\sqrt{2}\ (\ \bar{i} - \bar{k})$$

$$\ell^{31} = 1/\sqrt{2}\ (\bar{i} + \bar{j}) \qquad \ell^{32} = 1/\sqrt{2}\ (-\ \bar{i} + \bar{j}) \tag{A.10}$$

Substituting Equations (A.9) and (A.10) into Equation (3.3) gives the shear stress in each of the directions on the cube planes as:

$$\begin{bmatrix} \tau^{11} \\ \tau^{12} \\ \tau^{21} \\ \tau^{22} \\ \tau^{31} \\ \tau^{32} \end{bmatrix} = 1/\sqrt{2} \begin{bmatrix} 0 & 0 & 0 & 1 & 1 & 0 \\ 0 & 0 & 0 & 1 & -1 & 0 \\ 0 & 0 & 0 & 1 & 0 & 1 \\ 0 & 0 & 0 & 1 & 0 & -1 \\ 0 & 0 & 0 & 0 & 1 & 1 \\ 0 & 0 & 0 & 0 & -1 & 1 \end{bmatrix} \begin{bmatrix} \sigma_{11} \\ \sigma_{22} \\ \sigma_{33} \\ \sigma_{12} \\ \sigma_{13} \\ \sigma_{23} \end{bmatrix} \tag{A.11}$$

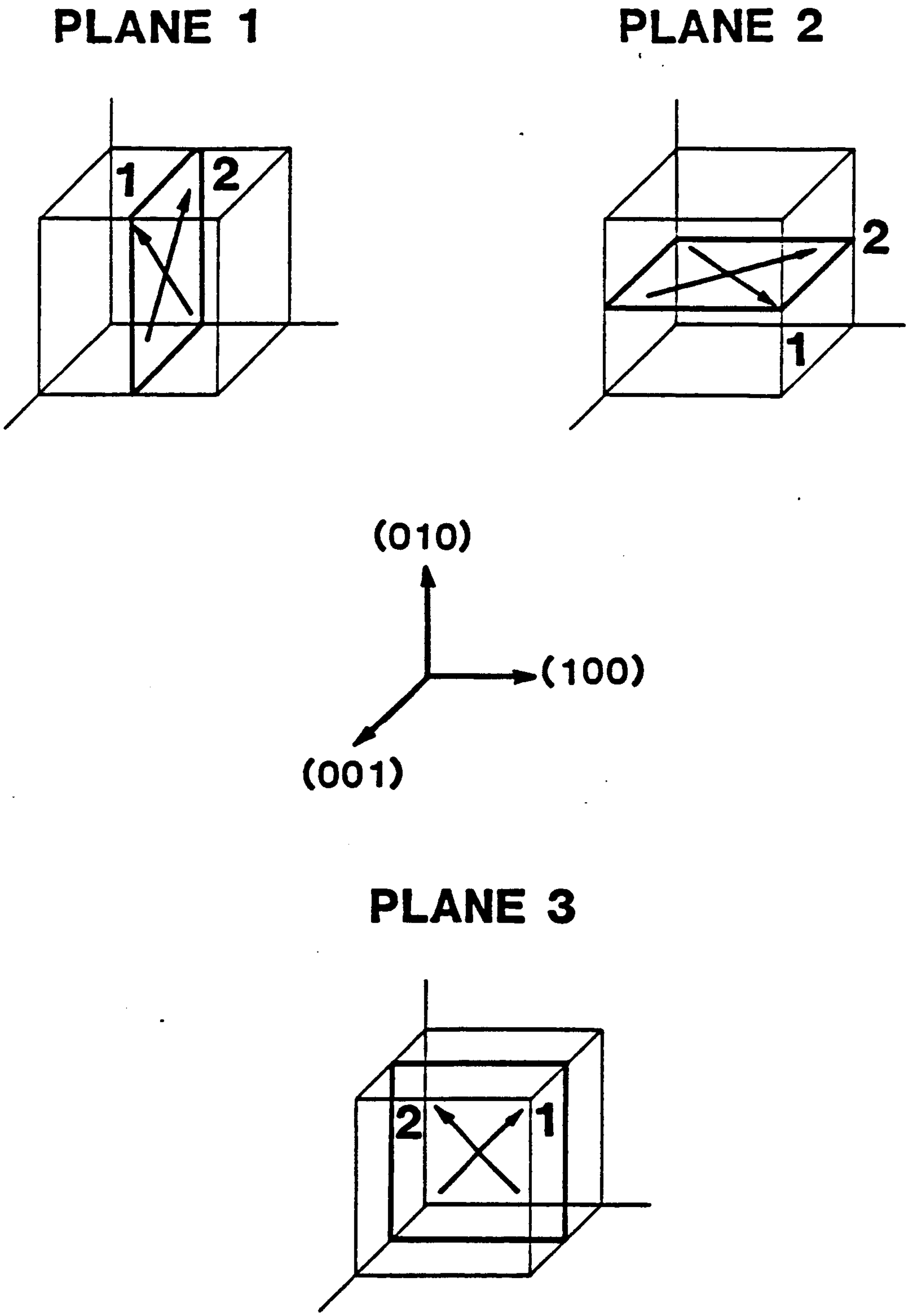
PLANE 1
1
2
PLANE 2
2
1
(010)
(100)
(001)
PLANE 3
2
1

Figure A-2 Cube a/2<110> slip systems

Substituting Equations (A.9) and (A.10) into Equation (3.6) gives the inelastic strain rate tensor, relative to the material principal axes, caused by shearing on the cube planes. That is:

$$
\begin{bmatrix} \dot{\epsilon}^{I}_{11} & \dot{\epsilon}^{I}_{12} & \dot{\epsilon}^{I}_{13} \\ \dot{\epsilon}^{I}_{21} & \dot{\epsilon}^{I}_{22} & \dot{\epsilon}^{I}_{23} \\ \dot{\epsilon}^{I}_{31} & \dot{\epsilon}^{I}_{32} & \dot{\epsilon}^{I}_{33} \end{bmatrix}_{\mathrm{CUBE}} = \sqrt{2}/4 \left\{ \begin{array}{l}
\dot{\gamma}^{11}_{\mathrm{CUBE}} \begin{bmatrix} 0 & 1 & 1 \\ 1 & 0 & 0 \\ 1 & 0 & 0 \end{bmatrix} + \dot{\gamma}^{12}_{\mathrm{CUBE}} \begin{bmatrix} 0 & 1 & -1 \\ 1 & 0 & 0 \\ -1 & 0 & 0 \end{bmatrix} + \\[2ex]
\dot{\gamma}^{21}_{\mathrm{CUBE}} \begin{bmatrix} 0 & 1 & 0 \\ 1 & 0 & 1 \\ 0 & 1 & 0 \end{bmatrix} + \dot{\gamma}^{22}_{\mathrm{CUBE}} \begin{bmatrix} 0 & 1 & 0 \\ 1 & 0 & -1 \\ 0 & -1 & 0 \end{bmatrix} + \\[2ex]
\dot{\gamma}^{31}_{\mathrm{CUBE}} \begin{bmatrix} 0 & 0 & 1 \\ 0 & 0 & 1 \\ 1 & 1 & 0 \end{bmatrix} + \dot{\gamma}^{32}_{\mathrm{CUBE}} \begin{bmatrix} 0 & 0 & -1 \\ 0 & 0 & 1 \\ -1 & 1 & 0 \end{bmatrix}
\end{array} \right\} \qquad \text{(A.12)}
$$

REFERENCES

Alden, T.H. (1973), "The Mechanisms of 'Metarecovery' and its Role in Temperature Dependence Plastic Flow," Metall. Trans., 4-1047.

Alexopoulous, P. Keusseyan, R.L., Wire, G.L. and Che-Yu Li (1982), "Experimental Investigation of Nonelastic Deformation Emphasizing Transient Phenomena By Using a State Variable Approach," Mechanical Testing for Deformation Model Developmen, ASTM STP 765, R.W. Rhode and J.C. Swearengen (eds) p. 148.

Asaro, R.J. (1983) "Crystal Plasticity," J. App. Mech. 50:921-934

Asaro, R.J. (1985) "Material Modelling and Failure Modes in Metal Plasticity," Mechanics of Materials, 4:343-373

Asaro, R.J. and Rice, J.R.(1977) "Strain Localization in Ductile Single Crystals," J. Mech. Phys. Solids, 25-309.

Asaro, R.J. and Needleman, A. (1984) "Flow Localization in Strain Hardening Crystalline Solids," Scripta Metall., 18:429

Asaro, R.J. and Needleman, A. (1985) "Texture Development and Strain Hardening in Rate Dependent Polycrystals," Acta Metall., 33:923

Bacroix, B., Jonas, J.J., Montheillet, F. and Skalli, A. (1986), "Grain Reorientation During The Plastic Deformation of F.C.C. Metals", Acta Metall., 34:937-950.

Bishop, J., and Hill, R. (1951a), "A Theory of the Plastic Distortion of a Polycrystalline Aggregate Under Combined Stresses", Phil. Mag., p. 41.

Bishop, J., and Hill, R. (1951b), "A Theoretical Derivation of the Plastic Properties of a Polycrystalline Face-Centered Metal", Phil. Mag., Vol. 42, p. 1298.

Bishop, J. (1952), "A. Theoretical Examination of the Plastic Deformation of Crystals by Glide", Phil. Mag., p. 51.

Blum, W. and Finkel, A. (1982), " New Technique for Evaluation of Long Range Internal Back Stress," Acta Metall., 30:1705.

Bodner, S., and Partom, Y. (1975), "Constitutive Equations for Elastic-Viscoplastic Strain-Hardening Materials", ASME, Journal of Applied Mechanics, Vol. 42, p. 385.

Cadek, J. (1987), " The Back Stress Concept in Power Law Creep of Metals: A review," Mat. Sci. Eng., 94:79-92.

Cuddy, L.J. (1970), "Internal Stress and Structures Developed During Creep," Metall. Trans., 1:395-401.

Dalal, R. P., Thomas, C. R. and Dardi, L. E. (1984), "The Effect of Crystallographic Orientation on the Physical and mechanical Properties of Investment Cast Single Crystal Nickel-Base Superalloy," Superalloy 1984, 5th Int. Symp. on Superalloys, ASM., Metals Park, Ohio, p. 185.

Dame, L.T. (1985), "Anisotropic Constitutive Model for Nickel Base Single Crystal Alloys: Development and Finite Element Implementation. Ph.D. Dissertation, University of Cincinnati.

Dame, L.T. and Stouffer, D.C. (1986), "Anisotropic Constitutive Model for Nickel Base Single Crystal Alloys: Development and Finite Element Implementation. NASA CR-175015, Lewis Research Center.

Eisenberg, M., and Yen, C.(1981), "A Theory of Multiaxial Anisotropic Viscoplasticity", Journal of Applied Mechanics, ASME, Vol. 48, p. 276.

Ezz, S., Pope, D., and Paidar, V. (1982), "The Tension/Compression Flow Stress Asymmetry in Ni_3 (Al,Nb) Single Crystals", Acta Metallurgica, Vol. 30, p. 921.

Fredholm A and Strudel J.L. (1984), "On The Creep Resistance of Some Nickel Base Single Crystals," Superalloy 1984, 5th Int. Symp. on Superalloys, ASM., Metals Park, Ohio, p. 211.

Flinn, P.A. (1960), Trans. TMS-AIME, 218:145-54.

Gell, M., Duhl, D.N. and Giamei, A.F.(1980), "The Development of Single Crystal Superalloy Turbine Blades," Superalloys 1980, Proceedings of Fourth Int. Sym. on Superalloys, ASM Internation, Metals Park, OH, pp.205-214.

Gell, M., and Leverant, G. (1968), "The Fatigue of a Nickel-Base Superalloy, Mar-M200, In Single-Crystal and Columnar-Grained Forms at Room Temperature", Trans AIME, Vol. 242, p. 1869.

Gabb, T., Gayda, J., and Miner, R. (1986), "Orientation and Temperature Dependence of Some Mechanical Properties of the Single-Crystal Nickel-Base Superalloy Reñe N4: Part II. Low Cycle Fatigue Behavior," Metall. Trans., Vol. 17A, P. 497.

Gilat, A. (1985), "A Viscoplastic Theory with Anisotropic Hardening and Its Application to Pressure-Shear Plate Impact Experiments," ASME paper 85-APM-37.

Han, Y. and Chaturvedi, M.C. (1987), "A Study of Back Stress During Creep Deformation of a Superalloy Inconel 718," Mat. Sci. Eng., 85:59-65.

Han, Y. and Chaturvedi, M.C. (1987), "Steady State Creep Deformation of Superalloy Inconel 718," Mat. Sci. Eng., 89:25-33.

Heredia, F. , and Pope, D.(1986), "The Tension/Compression Flow Asymmetry in a High γ' Volume Fraction Nickel Base Alloy," *Acta Metall.*, Vol. 34, No. 2, pp. 279-285.

Hill, R.(1965), "Continuum Micro-mechanics of Elastoplastic Polycrystals," *J. Mech. Phys. Solids*, 13:89.

Hill, R.(1966), "Generalized Constitutive Relations for Incremental Deformation od Metal Crystals by Multislip," *J. Mech. Phys. Solids*, 14:95.

Hill, R. and Havner, K.S.(1982), "Perspectives in the Mechanics of Elastoplastic Crystals", *J. Mech. Phys. Solids*, 30:5.

Holbrook, J.H., Rhode, R.W. and Swearengen, J.C. (1981), "The Continuity of Plastic Strain Rate," *Acta Metall.*, 29:1099.

Hopgood, A.A. and Martin, J.W. (1986), "The Creep Behavior od a Nickel-Based Single Crystal Superalloy", *Mat. Sci. Eng.*, 82:27-36

Hutchinson, J.W.(1970), "Elastic-Plastic Behavior of Polycrystalline Metals and Composites", *Proc. Roy. Soc. Lond.*, A319:247.

Jackson, P.J. (1986), "The Mechanisms of Plastic Relaxation in Single-crystal Deformation," *Mat. Sci. Engr.*, 81:169-174.

Jackson, P.J. (1985), "Dislocation Modeling of Shear In f.c.c. Crystals," Progress in Materials Science, 29:139-175.

James, G. H., Imbrie, P. K., Hill P. S., Allen, D. H. ans Haisler, W. E. (1987), "An Experimental Comparison of Several Current Viscoplastic Constitutive Models at Elevated Temperature," *J. Eng. Mat. and Tech.*, Vol. 109, p. 130.

Jones, R. (1975), *Mechanics of Composite Materials*, McGraw Hill, New York.

Jones, W,B. and Rhode, R.W. and Hicks, D.L. (1983), "Measuring Back Stress in commercial Alloys at Elevated Temperatures," *Trans 7th SMIRT Conf.*, Vol. L, P. 395.

Jones, W,B., Rhode, R.W., and Swearengen, J.C. (1982), "Deformation Modeling and the Strain Transient Dip Test," *Mechanical Testing for Deformation Model Development*, ASTM STP 765, R.W. Rhode and J.C. Swearengen (eds) p. 301.

Kassner, M.J., Miller, A.J. and Sherby, O.D. (1982), "The Separate Roles of Forest Dislocations and Subgrains in the Isotropic Hardening of Type 304 Stainless Steel," *Metall. Trans.*, 13A:1977.

Kear, B., and Piearcey, B. (1967), "Tensile and Creep Properties of Single Crystals of the Nickel-Base Superalloy Mar-M200", *Trans. AIME*, Vol. 239, p. 1209.

Krempl, E., McMahon, J.J., and Yao, D. (1986), "Viscoplasticity Based on Overstress with a Differential Growth Law for the Equilibrium Stress," *Mechanics of Materials*, Vol. 5, p. 35.

Lai, W.M, Rubin, D. and Krempl, E., "*Introduction to Continuum Mechanics*," Pergamon Press Inc., 1978.

Lall, C., Chin, S., and Pope, D. (1979), "The Orientation and Temperature Dependence of the Yield Stress of Ni_3 (Al, Nb) Single Crystals", *Metall. Trans.*, Vol. 10A, p. 1323.

Leverant, G., and Gell, M. (1969), "The Elevated Temperature Fatigue of a Nickel-Base Superalloy, MAR-M200, in Conventionally Cost and Directionally Solidified Forms", *Trans. AIME*, Vol. 245, p. 1167.

Leverant, G., and Kear, A.H. (1970), "The Mechanism of Creep in Gamma Prime Precipitation-Hardened Nickel-Base Alloys at Intermediate Temperatures", *Metall. Trans.*, Vol. 1, p. 491-498.

Lee, D., and Zaverl, F. (1978), "A Generalized Strain Rate Dependent Constitutive Equation for Anisotropic Metals", *Acta Metallurgica*, Vol. 26, p. 1771.

LeMay, I., "*Principles of Mechanical Metallurgy*," Elservier Science Pub. Co., Inc., New YorK, New York 10017, 1981.

Lowe, T.C. and Miller, A.K. (1983), "The Nature of Directional Strain Hardening," *Scripta Met.*, 17:1177-82.

MacKay, R. A. and Ebert, L. J. (1984) "Factors which Influence Directional Coarsening of γ' During Creep in Nickel Base Superalloy Single Crystals," *Superalloy 1984*, 5th Int. Symp. on Superalloys, ASM., Metals Park, Ohio, p. 135

MacKay, R. A. and Maier, R. D. (1982), "The Influence on the Stress Rupture Properties of Nickel-Base Single Crystals," *Metall. Trans.*, Vol. 13A, p. 1747.

Miller, A.K. and Ziaai-Moayyed, A.A. (1981), "Some Critical Experimental Tests of the MATMOD Constitutive Equations with respect to Directional Hardening and Cyclic Deformation," *Mechanical Testing for Deformation Model Developmen*, ASTM STP 765, R.W. Rhode and J.C. Swearengen (eds) p. 202.

Milligan W.W. and Antolovich, S.D. (1987), "Yielding and Deformation Behavior of the Single Crystal Superalloy PWA 1480," *Metall. Trans.*, Vol. 18A, p. 85.

Miner, R., Voigt, R., Gayda, J., and Gabb, T. (1986a), "Orientation and Temperature Dependence of Some Mechanical Properties of the Single-Crystal Nickel-Base Superalloy Rene N4: Part I. Tensile Behavior", *Metall. Trans.*, Vol. 17A, P. 491.

Miner, R., Gabb, T., Gayda, J., and Hemker, K. J. (1986b), "Orientation and Temperature Dependence of Some Mechanical Properties of the Single-Crystal Nickel-Base Superalloy Rene N4: Part III. Tensile-Compression Anisotropy," *Metall. Trans.*, Vol. 17A, P. 507.

Molinari, A., Canova, G.R. and Ahzi, S. (1987), "A Self Consistent Approach of the Large Deformation Polycrystal Viscoplasticity", Acta Metall., 35:2983-2994.

Nathal, M.V. and Ebert, L.J.(1985), "Elevated Temperature Creep-Rupture Behavior of the Single Crystal Nickel-base Superalloy NASAIR 100", Metal. Trans., 16A:427-439.

Oikawa, H. and Langdon, T.G. (1985), in Creep Behavior of Crystalline Solids, R.W. Evans (eds.), Pineridge, Swansea, P. 33.

Paslay, P., Wells, C., and Leverant, G. (1970), "An Analysis of Primary Creep of Nickel-Base Superalloy Single Crystals", Journal of Applied Mechanics, ASME, p. 759.

Paslay, P., Wells, C., Leverant, G., and Burck, L. (1971), "Creep of Single Crystal Nickel-Base Superalloy Tubes Under Biaxial Tension", Journal of Applied Mechanics, ASME, Vol. 38, p. 623.

Peirce, D., Asaro, R.J. and Needleman, A. (1982), "An Analysis on nonuniform and Localized Deformation in Ductile Single Crystals", Acta Metall., 30:1087.

Peirce, D., Asaro, R.J. and Needleman, A. (1983), "Material Rate Dependence and Localized Deformation in Crystalline Solids", Acta Metall., 31:1951.

Pope, D., and Heredia, F. (1984), "The Tension/Compression Asymmetry in High γ' Volume Fraction Nickel Base Alloy Single Crystals", Superalloy 1984 Fifth International Symposium on Superalloys, ASM, Metals Park.

Pope, D., and Ezz, S. (1984), "Mechanical Properties of Ni_3Al and Nickel-Base Alloys with High Volume Fraction of γ'", Int. Metals Reviews, Vol. 29, No. 3, p. 136.

Ramaswamy, V.G. (1986), "A Constitutive Model for the Inelastic Multiaxial Cyclic Response of a Nickel Base Superalloy Rene'80," NASA CR-3998.

Rhode, R.W., Jones, W,B. and Swearengen, J.C. (1981), "Deformation Modeling of Aluminium: Stress, Relaxation, Transient Behavior, and Search for Microstructural Correlations," Acta Metall., 29:41.

Shah, D. (1983), "Orientation Dependence of Creep Behavior of Single Crystal γ' (Ni_3Al)", Scripta Metallurgica, Vol. 17, p. 997.

Shah, D., and Duhl, D. (1984), "The Effect of Orientation, Temperature and Gamma Prime Size on the Yield Strength of a Single Crystal Nickel Base Superalloy", Proceedings of the Fifth International Symposium on Superalloys, ASM, Metals Park, Ohio.

Shih, C., and Lee, D. (1978), "Further Developments in Anisotropic Plasticity", Journal of Engineering Materials and Technology, ASME, Vol. 100, p. 294.

Steen, M., Provost, W. and Dhooge, A. (1985), "The Relationship between Microstructure and Internal Stress in a γ'-strengthened Superalloy," Mat. Sci. Eng., 76:139-146.

Stouffer, D.C., Jayaraman, N., Sheh, Y.C., and Alden, D. (1987), "Anisotropic Constitutive Modeling for Single Crystal Superalloy Rene N4 at 982°C", 6th NASA Turbine Engine Hot Section Technology Conference, Cleveland, Ohio, NASA CP-2493, pp289-298.

Swanson, G. (1984a), Life Prediction and Constitutive Models for Engine Hot Section Anisotropic Materials Program, Contract NAS3-23939, Monthly Report PWA-5968-8, August 1984.

Swanson, G. (1984b), Life Prediction and Constitutive Models for Engine Hot Section Anisotropic Materials Program, Contract NAS3-23939, Monthly Report PWA-5968-9, September 1984.

Swearengen, J.C., and Holbrook, J.H. (1985), "Internal Variable Models for Rate-dependent Plasticity: Anslysis of Theory and Experiment," Res Mechanica, 13:93-128.

Swearengen, J.C., Rhode, R.W., and Hicks, D.L. (1976), "Mechanical State Relastions for Inelastic Deformation of Iron: The Choice of Variables," Acta Metall., 24:969.

Taylor, G. (1938), "Plastic Strains in Metals", J. Inst. Metals, Vol. 62, p.307.

Turner, A.P.L. (1979), " Cyclic Deformation Behavior of Type 304 Stainless Steel at Elevated Temperature," Metall. Trans., 10A:225.

Turner, A.P.L., and Hasegawa T. (1982), "Deformation Microstructures and Mechanical Equations of State," Mechanical Testing for Deformation Model Developmen, ASTM STP 765, R.W. Rhode and J.C. Swearengen (eds) pp. 322-41.

Umakoshi, Y., Pope, D., and Vitek, V. (1984), "The Asymmetry of The Flow Stress In $Ni_3(Al,Ta)$ Single Crystals", Acta Metallurgica, Vol. 32, No. 3, p. 449.

VerSnyder, F. and Piearcey, B.(1966), "Single Crystal Alloy Extends Turbine Blade Service Life Four Times", SAE Journal, Vol. 74, p. 36.

Walker, K.P. (1981), "Research and Development Program for Nonlinear Structural Modeling and Advanced Time-Temperature Dependent Constitutive Relationships," NASA CR165533.

Weertman, J., (1975) in Rate Processes in Plastic Deformation of Materials, Proc. J. E. Dorn Symp., J.C.M. Li, and A.K. Mukherjee (eds.), ASM, Metals Park, Ohio, P. 315.

Yang, S. (1984), "Elastic Constants of a Monocrystalline Nickel-Base Superalloy", Metall. Trans., Vol. 16A-No. 4, p. 661.